JUPITER'S MOON EUROPA: NEW INSIGHTS FROM PHYSICAL EXPERIMENTS WITH IMPLICATIONS FOR GLOBAL RESURFACING PROCESSES AND PLANETARY ICE TECTONICS

By

MICHAEL WILLIAM KLASER

A thesis submitted to the

Graduate School-New Brunswick

Rutgers, The State University of New Jersey

In partial fulfillment of the requirements

For the degree of

Masters of Science

Graduate Program in Geological Sciences

Written under the direction of

Dr. Juliane Gross

And approved by

_____

_____

_____

_____

New Brunswick, New Jersey

October, 2017

ABSTRACT OF THE THESIS

Jupiter's Moon Europa: New insights from physical experiments with implications for global resurfacing processes and planetary ice tectonics

By MICHAEL WILLIAM KLASER

Thesis Director: Dr. Juliane Gross

Jupiter's moon Europa is a differentiated planetary body comprised of a metallic core, a silicate mantle, and an outer layer of H_2O. This shell can be further subdivided into an icy surface shell and a liquid subsurface ocean; details about the physical properties and structural parameters, such as the thickness, of the surface ice shell are poorly understood. Further, Europa has one of the youngest geologic surfaces in our solar system with an age of 40 - 90 Ma, implying an intense history of resurfacing. Although this young surface exhibits many extensional features such as dilational bands at which new surface material is created, evidence of corresponding contractional features is sparse. Recently, however, evidence for subduction on Europa has been observed. In this model, brittle, denser, conductive surface ice is thrust and subducted into a warmer, less dense and convecting subsurface ice. This process could be responsible for recycling aging terranes on a large scale. However, the basic physical parameters needed to initiate subduction on Europa, such as thickness of the brittle conductive layer, deformation rates, and orientation of pre-existing zones of weaknesses, are not well understood.

In this study, we used a set of physical analogue paraffin wax experiments to examine the conditions that could lead to the initiation of subduction on Europa, such as

the conductive layer thickness, deformation rate, and orientation of the pre-existing zone of weakness. The wax is heated from below and cooled with N_2 from above so that a solid conductive lid forms above a molten convecting wax layer, similar to proposed ice models of Europa. Our results indicate that subduction could be initiated over a broad range of surface thicknesses and deformation rates above a minimum conductive layer thickness. In general, thicker conductive layers and faster deformation rates more readily initiate subduction. However, subduction in our experiments is strongly dependent on the orientation of the pre-existing zones of weakness; inclined pre-existing zones of weakness allow subduction over a wider range of thicknesses and deformation rates compared to vertical ones. Below a minimum critical conductive layer thickness, the conductive layer behaves ductilely during shortening, resulting in a previously undescribed process called ductile roll back, in which surface material is pushed, rolled, and eventually subducted into the subsurface at a pre-existing zone of weakness. Both ductile roll back and subduction in the experiments can accommodate a significant fraction of boundary displacement and, thus, could play a critical role in resurfacing Europa throughout its geologic history. These results establish a conceptual framework for the recognition and study of contractional surface features on Europa, which in turn have significant implications for Europa's thermal history and evolution, habitability, and future space-craft missions.

ACKNOWLEDGMENTS

My sincerest gratitude to my advisor, Dr. Juliane Gross for taking a risk on a project she had no background in, with a student who had no experience, on a planetary surface neither knew much about. What separates good leadership from great leadership is a deep sense of personal responsibility for the professional development of their followers, and a willingness to make sacrifices to ensure their success. Dr. Gross possesses these traits in spades. It has been a privilege to work on this project with her, and I have grown immensely as a scientist with her guidance.

Secondly, this project would not have been possible without Dr. Sarah Tindall. She generously allowed me to invade her lab at Kutztown University and turn it into a giant wax mess for the better part of a year. Her positive attitude and encouragement helped me stick at it, especially when the commutes were starting to wear on me.

Also, a big thanks to Dr. Roy Schlische and Dr. Chris Potter for being on my committee, and for the years of mentorship.

I would also like to thank my wife, Dr. Diana Klaser Cheng. She's been a loving and supportive partner, and she's also a scientist whom I look up to. She has been my informal therapist during graduate school, a thankless task for which I will now thank her. Thanks wife. You're the best.

I'd like to thank all my fellow geology graduate students, past and present. You guys are all awesome, let's grab some beers sometime soon. Max Needle, thanks for making me read that nonsense paper about ice subduction on Europa.

Hey Mom and Dad: look at me, I'm a scientist! Love you both!

And to all my SSBN-734G Peeps: Report to Dink Study you NUBs!!!

TABLE OF CONTENTS

LIST OF TABLES

LIST OF FIGURES

ADDITIONAL FIGURES OF ALL EXPERIMENTS IN APPENDIX A

1. Introduction

Europa is one of the four Galilean moons that orbit Jupiter in prograde, near-circular, and roughly co-planar orbits (Canup and Ward, 2008). Europa is the second closest moon to Jupiter and the smallest of the four Galilean moons with a radius of 1562 km, a mean density of 3.01 g/cm^3, and a surface gravity of 1.314 m/s^2 (Park, 2015). Based on gravity data, Europa is believed to be fully differentiated, composed of a metallic core, a silicate mantle, and an outer H_2O package (Schubert et al., 2009). The outer H_2O package can be further divided into a liquid water ocean with an overlying crust of ice (e.g., Pappalardo et al., 1998, 1999; Kivelson et al., 2000; Billings and Kattenhorn, 2005). The total thickness of the entire H_2O package (liquid water ocean and icy surface shell) is not well constrained and estimates are currently limited to and by surface observations and gravity data (Anderson et al., 1998). These methods have poor resolution in terms of the structure and physical properties of the crust and ocean. Therefore, it is unclear what phases are present and whether the liquid water ocean is overlain by a brittle surface shell or if this icy surface shell can be further subdivided into a ductile, warm, less dense convecting ice layer underneath a denser, brittle, conductive surface ice layer. Current thickness estimates of the total H_2O package (liquid ocean and ice) range from 80 to 170 km (Anderson et al., 1998; Billings and Kattenhorn, 2005). This range largely depends on whether some or most of the silicate minerals in Europa's mantle are hydrated, which would result in a lower density of that silicate layer and, thus, an increase in the total thickness of the overlying H_2O package (Schubert et al., 2009).

The thickness of the solid icy shell and its physical properties have been inferred based on surface morphology and topography, including impact craters (e.g., Carr et al.,

1998; Pappalardo et al., 1998; Hoppa et al., 1999b; Prockter et al., 2000; Turtle and Pierazzo, 2001; Schenk, 2002; Nimmo et al., 2003; Nimmo et al., 2007; Schenk and Turtle, 2009; Bray et al., 2014), induced magnetic field (Zimmer et al., 2000), tidal dissipation (Hussmann et al., 2002; Tobie et al., 2003; Wahr et al., 2006), and orbital evolution and thermal models (e.g., Ojakangas and Stevenson, 1989; Hussman et al., 2002; Spohn and Schubert, 2003; Sotin and Tobie, 2004). The results of these studies vary widely and can be roughly classified into two models (Fig. 1):

(1) A thin-shell model with thickness estimates ranging from 0.1 - 8 km. These estimates are mostly inferred from mechanical methods (e.g. flexture estimates, bouancy estimates, impact crater morphology, etc: see Billings and Katterhorn, 2005) and only estimate the thickness of a brittle surface ice layer , whether or not it is underlain by a lower layer of ductile warmer ice (e.g., Schenk and McKinnon, 1989; Carr et al., 1998; Williams and Greeley, 1998; Hoppa et al., 1999a; Greenberg et al., 2000; Kadel et al., 2000; Billings and Kattenhorn, 2002, 2003, 2005 and references therein; Nimmo et al., 2003; Hufford et al., 2004; Hand and Chyba, 2007).

(2) A thick-shell model with total thickness estimates ranging from 6 km up to 40 km. These estimates are mostly inferred from thermal analyses, thermal equilibrium, temperature gradient calculations, and current models of surface features (e.g. Pappalardo et al., 1998; Hussmann et al., 2002; Nimmo et al., 2003; Billing and Kattenhorn, 2005 and references therein; Schubert et al., 2009; Nimmo and Manga, 2009; Kattenhorn and Prockter, 2014). These models consider the entire ice-shell thickness and include (and imply) the existence of a ductile, convecting, warm

lower layer below the conductive (brittle) surface layer (see Billing and Kattenhorn, 2005 and references therein for a more detailed description). Thickness estimates for the conductive surface ice layer range from 0.1 km to 6 km (Billing and Kattenhorn, 2005) and can be further sub-divided (Fig. 2) (Nimmo and Manga, 2009). Thickness estimates for the underlying ductile, warm, convecting ice layer range from 2 km up to 40 km (Pappalardo et al., 1999 and references therein; Billing and Kattenhorn, 2005 and references therein; Schubert et al. 2009; Nimmo and Manga, 2009).

Europa experiences several sources of stress acting at different time scales that modify its icy surface and contribute to the formation of observed tectonic features. On a shorter time scale (days), Europa experiences significant diurnal tidal forces due to its orbital eccentricity, resonance with Io and Ganymede, and a potentially decoupled ice shell (e.g., Greenberg et al., 1998; Greenberg et al., 2003; Harada and Kurite 2006; Wahr et al., 2009; Kattenhorn and Hurford 2009; Rhoden et al., 2010) (Fig. 3). On a longer time scale, Europa experiences non-synchronous rotation of the decoupled icy shell, which could result in large stress build-ups in the shell (e.g., Greenberg et al., 1998; Kattenhorn 2002; Hurford et al., 2007; Sotin et al., 2009; Wahr et al., 2009). The observed tectonic features include ridges, bands, troughs, and cycloids (Kattenhorn and Hurford, 2009), as well as sparse folding (Prockter and Pappalardo, 2000), and strike-slip faults (Kattenhorn, 2004).

Crater counting age dates indicate that the Europan surface is young, placing it between 40-90 Ma (Bierhaus et al., 2009), which implies an active history of past and potential presently ongoing resurfacing processes. A wide variety of resurfacing

processes have been proposed for Europa, including several types of cryo-volcanism (Fagents, 2003) and impact processes (Scheck and Turtle, 2009). However, these processes alone do not appear to be widespread enough to resurface Europa to the extent required for a young surface age of 40-90 Ma (Fagents, 2003; Schenk and Turtle, 2009).

Work by Prockter et al. (2002) established that new surface ice material is created at dilational bands, analogous to terrestrial mid-ocean ridges. Since no data suggest the outer ice shell of Europa is growing, some process or combination of processes must recycle aging terranes back into the subsurface. Kattenhorn and Prockter (2014) tectonically reconstructed a small portion of Europa's trailing northern hemisphere (imaged by Galileo) and showed evidence that almost 100 km of surface material was missing without any observable change in topography. This missing material coincided with previously described contractional bands. Kattenhorn and Prockter (2014) proposed that these contractional bands were in fact subduction zones, where colder, brittle, and denser conductive ice subducts into warmer, less dense and convecting subsurface ice (Fig. 4). While the subduction process is analogous to terrestrial subduction, there is one major distinction: on Europa, the subducted slab is re-integrated into the convecting, ductile subsurface ice (Fig. 4). This part of the process is called subsumption to distinguish it from subducted slab processes on Earth (Kattenhorn and Prockter, 2014). If subduction and subsumption occur on Europa, the work of Kattenhorn and Prockter (2014) would establish the first example of full plate tectonics on another planetary body, with new crustal material being created at dilational bands, old terranes being recycled at subduction zones, and a complex array of microplates. However, this

subduction/subsumption process is not well understood and Europan subduction initiation conditions are unknown.

In this study, we aim to understand the basic physical parameters that may allow subduction to take place using a series of two-layered paraffin wax experiments composed of a solid, conductive surface layer and an underlying viscous, convecting wax layer as analogue to the brittle, conductive surface ice layer and the underlying ductile, convecting, warmer ice layer on Europa. We investigate three parameters and their constraints on subduction initiation: **1) the role of solid (brittle) layer thickness on the ability of that layer to undergo subduction, 2) the role of deformation rate in the initiation process of subduction, and 3) the role of pre-existing zone of weakness orientation on subduction initiation**.

By varying the thickness of the brittle layer, the deformation rate, and the orientation of a pre-existing zone of weakness (vertical vs. 45° inclined) in the experiments, we can study the influence these parameters have on subduction initiation. Aside from providing insight into subduction as a process, helping to constrain the brittle layer thickness on Europa will additionally provide important insight into the total brittle + ductile ice shell thickness. This is vital to our understanding of Europa's geologic history and processes (Billings and Kattenhorn, 2005) and has important implications for habitability (Chyba and Phillips, 2001; Figueredo et al., 2003). In addition, this work may provide important inputs for the design and planning of future space missions (Nimmo et al., 2003) such as the Europa Clipper lander mission, including the identification of potential subduction markers and future survey locations.

2. Methods

2-1 Equipment and Materials

2-1-1 Equipment

In this study, paraffin wax is used as an analogue material to the proposed brittle, conducting icy surface layer and the underlying ductile, convecting ice subsurface layer on Europa. To protect existing equipment from wax contamination, a self-contained experimental apparatus was constructed that can fit inside of the existing equipment. Figure 4 shows a schematic sketch of the experimental box apparatus. This apparatus consists of a plexiglass box with four fixed side walls, one internal moving wall, and a base (Fig. 5). All walls are made from 1/2" (1.3 cm) thick plexiglass. The internal dimensions (length x width x height) of the box are 24" x 23" x 12" (61 cm x 58.4 cm x 30.5 cm). The long sides of the box are made from clear plexiglass to allow cross-section viewing (Fig. 6b), while the rest of the box is made from white opaque plexiglass. The internal moving wall (Fig. 6a, c) is notched at the bottom to allow it to pass over the heat mat (Fig. 6a) and to allow molten wax to flow from one side of the moving wall to the other. With this design, consistent total wax depth can be maintained on either side of the moving wall.

To move the internal wall, it is coupled to a stainless steel external moving wall through the rear fixed wall of the experiment box with four stainless steel rods and secured by washers and nuts (Fig. 6c). Four rubber grommets attached to the rear fixed

wall, through which the rods pass, prevent molten wax leakage (Fig. 6c). The external moving wall is attached to a threaded rod. An AC motor, coupled to a transmission, moves this threaded rod and thus, the external and internal moving walls. The AC motor is controlled by a custom computer program called "Motor Control" created in National Instruments™ LabVIEW 8.0, running on a standalone computer. This program allows the user to drive the moving wall forward or backward at any rate between 0.1 - 35 cm/hr (±0.1 cm/hr).

To heat the wax from the bottom of the experiment, three resistance heat mats with the dimensions of 24" x 12" (61 cm x 30.5 cm, one mat) and 12" x 12" (30.5 cm x 30.5 cm, two mats) lie flat directly atop the base of the box (Fig. 6a). These heat mats are controlled by a STC-1000 digital temperature controller with thermocouple monitoring. The digital temperature controller has a measuring range of -50 °C to +99 °C, with a resolution of 0.1 °C and an error of ±1 °C, and provides 110V, 60hz AC power to the heat mats. The heat mats have a power density of 2.5w/in^2 (0.004watts/mm^2) for a total power capacity of 576 watts between the three mats. The heat mats have an operating temperature range from -51°C to +232 °C. In addition to controlling the heat mat temperatures, the STC-1000 digital temperature controller also monitors and records the liquid wax temperature, while the solid wax surface and box air temperatures are monitored and recorded using thermocouples connected to a Fluke 52-2 digital thermometer.

To cool the surface solid wax layer of the experiment, a U-shaped 1/2" (1.3 cm) outer diameter flexible copper manifold runs along the eastern and western sides of the box horizontally, directly above the side walls (Figs. 6c, 7a, c). The copper manifold is

coupled with a stainless steel braided cable to a 22-psi liquid nitrogen cryo-tank. Each side of the manifold contains 3 - 4 narrow horizontal slits approximately 1” in length that allow cold N_2 gas to flow out onto the model surface (Fig. 7b). For the N_2 gas to encompass and thus cool the entire surface evenly, as opposed to hit and only cool the areas directly underneath the slits, the slits are directed slightly upward and outward toward the top of the apparatus, thus allowing the cold gas to spread evenly over the entire box dimensions before it reaches the surface. Each side of the copper manifold sits inside a cardboard tube, with larger holes corresponding to each copper slit (Fig. 7b). This set-up allows liquid N_2 drops from the copper manifold slits to be contained within the cardboard tube and evaporate instead of reaching the surface, which would result in localized cooling, and thus thickening of areas directly beneath the copper manifold slits. To contain the N_2 gas within the box and insulate the box from the surrounding warmer air during cooling, a cardboard lid roughly seals the entire experiment apparatus box during the experimental runs (Fig. 7c). This ensures homogenous cooling of the entire wax surface.

During experimental runs, photos are systematically taken (see Appendix A for experiment picture schedules) with a Canon Rebel T5 digital camera mounted on a tripod suspending it directly above the box (Fig. 7a). When pictures are taken, the wax surface is lit from the moving wall with two LED light strips to ensure optimal lighting conditions. In addition, temperatures at the heat mat array (T_{mat}), solid wax surface at a depth of ~2mm ($T_{brittle}$), and box air (T_{air}), are recorded every minute throughout the entire experimental run to ensure constant thickness of the solid, brittle layer during the run. A series of trial and error experiments (not described here) established the duration of initial

cooling, and the range of experiment run temperatures required to maintain consistent solid layer thickness (See Table 1).

2-1-2 Materials

The paraffin wax is "General Purpose Candle Making Wax", brand Country Lane™, with a melting point of ~53° C, purchased in 10 lb slabs from Hobby Lobby®. Copper manifold and associated hardware purchased from Home Depot®, as were the required electrical wiring components. Plexiglass walls, stainless steel rods, heat mats, and associated hardware purchased from Grainger®. Digital temperature controller purchased from Amazon®.

In our 2-layered wax experiments, the solid surface wax layer is analogous to the brittle, conductive surface ice layer on Europa, while the molten wax layer is analogous to the convecting subsurface ice layer on Europa. Our solid surface layer can be further subdivided into an upper brittle layer and a lower plastic layer (Fig. 2c). This is similar to the subdivision of the conductive surface ice on Europa (Fig. 2b) (Manga and Sinton, 2004; Nimmo and Manga, 2009). For a more detailed discussion of paraffin wax as an analogue material, see section 4-5.

2-2 Procedure

The paraffin wax is pre-heated in a 9-gallon aluminum kettle with separate electric heat mats before each experiment. The molten wax is then added to the box and cooling with N_2 gas begins immediately. During cooling, the heat controller is set to 55°C to minimize heat input and allow the solid surface wax layer to grow. Cooling periods range from 30 minutes for the 1 cm solid layer experiment, up to 2.5 hours for the

4 cm solid layer experiment. After initial cooling, a 5 cm grid is marked on the solid wax surface, which serves as a deformation tracking system. Additionally, the camera is calibrated, the displacement rate is set, and thicknesses samples (approximately 1cm^2) are carefully cut out of the surface with a heated knife. After these tasks are performed, cooling is resumed for an additional 10 minutes to counteract any weakening of the brittle surface layer during those preparations. Afterwards, cooling is paused and a pre-existing zone of weakness (PZW) is created by cutting the entire depth of the solid wax layer from west to east near the center of the experiment with the heated knife. The PZW in the experiments represents any one of the ubiquitous fractures observed on Europa's surface (e.g. Kattenhorn and Hurford 2008) where subduction might initiate, including ridges, bands, cycloids, etc. For inclined PZWs, the cut angle always dips south approximately 45°, unless otherwise noted. Immediately after the cut, boundary displacement begins by setting the moving wall in motion. Boundary displacement is due north in all experiments. To maintain a consistent solid layer thickness during the experiment, cooling is resumed throughout the experimental run with a closed cardboard lid and the set temperature for the heat controller is raised to 61°C. To take pictures of the surface during an experiment, the N_2 flow is turned off immediately prior to taking the pictures and the lid is removed to allow the N_2 gas to clear out and expose the surface. After the picture is taken, the lid is reinstalled and cooling is resumed. This process takes approximately 20-25 seconds (for picture schedules, see Appendix A). Experiments last between 26 to 36 minutes depending on brittle layer thickness and deformation rate. Experiments are restricted to this range because controlling conductive layer thickness beyond ~40 minutes is challenging. Upon completion of the experiment, the moving wall

is stopped, cooling is stopped, and thickness samples are taken again from areas adjacent to the pre-run sample locations to verify consistent solid layer thickness throughout the run. Multiple post-run pictures are taken with a variety of lighting directions and camera orientations. All photos are processed in Adobe Lightroom 6 and in addition to individual pictures, time lapse movies are created for each experiment.

3. Results

3-1 Definitions

In the experiments, ***subduction*** is defined as a process in which one plate is thrust atop another, and the underlying plate is then subducted with increasing boundary displacement (Fig. 8). Initiation of subduction is marked by the development of a thrust fault, either by inclined PZWs, natural thrust fault development in vertical PZWs, or by the overturning of blocks with increasing boundary displacement that eventually results in a thrust fault geometry. If subduction occurs over ≥75% of the length of the PZW, the experimental run is defined as ***full subduction.*** If subduction occurs only on a portion of the PZW, <75% and >10%, the run is defined as ***partial subduction***. If subduction occurs on ≤10% and does not propagate, especially if it begins at an edge, or does not occur at all, then the experiment is defined as <u>not</u> resulting in subduction.

In the experiments, ***ductile roll back*** is defined as the pushing of surface material into the subsurface by two fold limbs at the PZW (Fig. 9). Ductile roll back initiates at the PZW when the southern limb of an anticline north of the PZW and the northern limb of an anticline south of the PZW push the PZW into the subsurface and progressively roll

additional surface material into the subsurface with increasing boundary displacement. Figure 10 compares the model surface topography created by subduction and ductile roll back.

Surface distance measurements, given in Appendix A, have a maximum error of ± 1.5 cm, which is the result of a trigonometric calculation of the maximum distortion of horizontal distance based on the most extreme dip angle in the experiments (45°) on which subduction accommodation is measured:

$$\mathrm{X} - (\mathrm{X}COS\angle) = Error \qquad \text{Eq. 1}$$

where X is the horizontal distance measured on the surface in centimeters, and ∠ is the angle of dip of that surface in degrees. Most experiments exhibit dips far less extreme and thus, most surface measurement errors are less than ± 1 cm. Table 2 summarizes the error values for the observed dip angles in the experiments.

3-2 Results Summary

The maximum boundary displacement for fixed-duration experiments is dependent on the displacement rate and thus, each experiment results in a different total (maximum) displacement (Fig. 11). For 10 cm/hr maximum boundary displacement is 5.5 - 9.5 cm, for 20 cm/hr it is 10 - 13 cm, and for 30 cm/hr it is 13 - 14 cm (Table 3, 4). Therefore, to compare experimental results to each other, all experiments were examined for subduction initiation by 5.5 cm of boundary displacement (Fig. 12). See Appendix for a detailed description of each experiment.

3-2-1 Vertical PZWs

In our vertical PZW experiments, the solid conductive layer thickness as well as the boundary displacement rate plays a significant role in the ability to subduct surface material. In general, the slower the deformation rate and the thinner the solid surface material, the less likely subduction will initiate (Fig. 12).

In the thinnest, 1 cm, solid layer experiments subduction never occurred regardless of the boundary displacement rate (Figs. 12, Table 3). Instead, boundary displacement results in buckle folding only (Appendix. A. Figs. A, B, C). Here, the PZW serves as a buttress between the folds on either side. At the onset of boundary displacement in these experiments, the southern limb of the northern fold and the northern limb of the southern fold, respectively, push the PZW into the subsurface. With increasing boundary displacement, additional surface material is pushed into the subsurface at the PZW via ductile roll back. This process accommodates a significant portion of boundary displacement in the 1 cm experiments at all examined deformation rates. For example, in the 1 cm at 10 cm/hr experiment (Appendix Fig. A), 7.3 cm of surface material is pushed into the subsurface via ductile roll back, which represents 77% of the boundary displacement imposed. Surface topography is generally minimized during ductile roll back (Appendix Figs. A, C) and usually results in two parallel ridges with the PZW in the center (e.g., Appendix Figs. A; see also section 4:4-2, Fig. 20).

Only solid layers thicker than 1.5 cm with a deformation rate faster than 10 cm/hr result in partial or full subduction (Fig. 12). In general, the thicker the solid layer, the less ductilely it behaves. In experiments with solid conductive layers thicker than 1 cm large wavelength buckle folds form with high surface topography, instead of ductile roll back

(Appendix Figs. E, F, G, H, J, K, L; also see 4:4-1, Fig. 18). These folds can accommodate a significant fraction of boundary displacement in the experiments. For slower boundary displacement rates (20cm/hr) the solid surface must be thicker than 2.5 cm for partial subduction to occur (Fig. 12). In fast boundary displacement rate experiments (30 cm/hr), however, partial subduction can occur if the thickness is greater than 1.5 cm. Full subduction occurs at solid-layer thicknesses greater than 2 cm (Fig. 12). In many experiments subduction is either preceded by, or accompanied by, large wavelength (> 15 cm) buckle folding (e.g. Appendix Figs F, G, K, L, M). However, for the fastest deformation rate experiments (30cm/hr) at 2.5 cm solid surface thickness and at 4 cm solid surface thickness subduction does not result in significant surface topography. For those specific experiments subduction is accompanied by block overturning and upwelling of subsurface wax that flows from the subduction zone onto the subducting plate and overriding plate, resulting in hummocky textures/subduction bands on the subducting plate (Appendix Figs. I, M). Upwelled surface wax on the overriding plate remains un-deformed with increasing boundary displacement, resulting in smooth texture.

3-2-2 Inclined PZWs

In the inclined PZW experiments, solid conductive layer thickness plays a central role with no subduction initiation for any of the 1 cm solid conductive layer thickness experiments (Fig. 13) regardless of boundary displacement rate. In general, however, solid layers more readily subduct in the inclined PZW experiments.

Like the vertical PZW experiments, 1 cm thick solid conductive layer experiments with inclined PZWs do not result in subduction and instead cause ductile roll back at the

PZW (Appendix Figs. N, O, P). The PZW serves as a buttress between the folds on either side. At the onset of boundary displacement in these experiments the southern limb of the northern fold and the northern limb of the southern fold push the PZW into the subsurface. With increasing boundary displacement, additional surface material is pushed into the subsurface at the PZW. Like the vertical PZW experiments, ductile roll back can accommodate significant proportions of boundary displacement, with up to 80% of imposed convergence being driven into the subsurface (e.g., 1 cm at 30 cm/hr; App. A Fig. P).

The deformation rate plays a much less significant role in the ability of the solid layer to be subducted in the inclined PZW experiments (Fig. 13), and the range of deformation rates that result in subduction is much broader in these experiments compared to the vertical PZW experiments (Fig. 13; App. A Fig. Y). In the inclined PZW experiments subduction occurs over the entire range of experimental boundary displacement rates for the 3 cm solid layers, and partial to full subduction occurs over the entire range of the 2 cm solid layer experiments (Fig. 13, Table 3). Additionally, the surface relief that results from boundary displacement is generally much less pronounced in the inclined PZW experiments compared to the vertical PZW experiments, independent of the solid conductive thickness (e.g. compare the shadows cast in Appendix Figs. L and W, and see Section 4-4-1, Fig. 18). Subduction in the inclined experiments is not preceded by, nor accompanied by, any significant topographic relief across the subduction zone (Appendix Figs. R, S, T, U, V, W), with one exception (Appendix Fig. Q).

4. Discussion

The thickness of the ice shell on Europa is important to our understanding of Europan geologic evolution and processes including the development of chaos features; impact crater morphologies (and thus surface age calculations); the formation of ridges, bands, and faults which represent structural lineaments in the ice shell; and the formation of pits, spots, and domes. The thickness of the ice shell also has crucial implications for habitability and exobiological studies (Chyba and Phillips, 2001), as nutrient transport and sustainability are limited by the ice shell thickness (Gaidos et al. 1999; Chyba et al., 2000; Chyba and Phillips, 2001; Figueredo et al., 2003). Direct and indirect (through radar) access to the ocean during future exploration, such as by the proposed NASA Europa Clipper Mission, will also be affected by ice shell thickness (Billings and Kattenhorn, 2005).

The current models of observed features on the Europan surface imply the presence of a ductile, convecting subsurface ice layer beneath a brittle, conductive surface ice layer (Fig. 1b) whose thickness estimates are variable (e.g., Billings and Kattenhorn, 2005; Kattenhorn and Prockter, 2014). Previous two-layered analogue models, investigating the role of the ductile/convecting lower ice layer on the brittle/conducting surface ice layer deformation, used two different materials such as therapeutic putty underneath fine-grained sand to represent the ductile lower layer overlain by a brittle surface layer (Leonard et al., 2016). In this study however, we aim to understand basic physical parameters that may allow subduction as a resurfacing process to take place on Europa, regardless of the thickness of the convecting lower ice layer. Specifically, we are investigating the effects of thickness of the conductive outer ice

layer, deformation rate, and orientation of a preexisting zone of weakness on the initiation of subduction. In contrast to Leonard et al. (2016), we are using a single medium for our two-layered model that undergoes phase transitions, similar to H_2O, so that temperature alone is the major controlling factor for its mechanical behavior.

The results of our experiments indicate that a very thin conductive surface layer, regardless of the orientation of a pre-existing zone of weakness and deformation rate, never subducts, whereas thicker solid conductive surface layer can subduct more easily. The effects of the conductive layer thickness, displacement rate, and the orientation of the PWZ on subduction initiation is discussed in more detail below. It is important to note here that the solid, conductive layer thickness, deformation rate, and the PZW orientation are parameters which are related, as are the physical phenomena that control them. While the three parameters explored in our study may not represent a comprehensive list of the factors that control subduction initiation on Europa, the experiments demonstrate that subduction can occur over a broad range of conditions if important physical requirements are met.

4-1 Effect of the Conductive Layer Thickness

While the estimates of the total ice thickness on Europa vary from 0.1 km up to 40 km (Fig. 1, see discussion above and introduction) for an intra-ice subduction system to be feasible, the brittle conductive ice layer must be thin compared to the ductile convecting subsurface ice (Kattenhorn and Prockter, 2014), as previous modeling work indicates a minimum total ice thickness of 27 km for convection to initiate on Europa (Hussmann et al., 2002). The experiments in this study indicate that the conductive

surface layer thickness plays a role in the ability of that layer to be subducted. Deformation of the thinnest solid conductive layers, regardless of the orientation of the PZW and deformation rate, results in ductile roll back and is usually accompanied by widespread ductile surface deformation features, such as long-wavelength folds. This is most likely due to the higher heat flux that the thin layer experiences provided by the underlying warm, convecting subsurface layer. Thus, if the conductive icy surface layer on Europa is on the thinner side of the 0.1 to 6 km estimated thickness, the conductive surface ice layer should behave more ductilely, resulting in widespread long-wavelength folding and ductile roll back. Such surface features are not widely observed on the Europan surface (Kattenhorn and Hurford, 2009).

On the other hand, our experiments suggest that above some minimum initial thickness of the conductive layer, subduction initiation is possible over a wide range of thicknesses (Figs. 12, 13). Thus, widespread subduction on Europa could occur if the conductive icy surface layer is closer to the thicker side of the estimated 0.1 – 6 km thickness for this layer. Operation of subduction as a geologic process could be possible over a long span of Europa's geologic history, given that the brittle surface ice layer on Europa is most likely heterogeneous in thickness (Zahnel et al., 2003; Nimmo et al., 2005; Sotin et al., 2009), has potentially changed in thickness with time (Zahnel et al., 2003), and/or periodically thins and thickens (Hussmann and Spohn, 2004). Consequently, other more exotic re-surfacing mechanisms, such as large impacts and widespread cryo-volcanism, are not required at significant magnitudes to explain the 40-90 Ma young surface of Europa that is observed today. Therefore, it is possible that

subduction began early in Europa's geologic history, operated throughout that history, and could be responsible for recycling most of the aging terranes.

4-2 Effect of Deformation Rate

Our experiments indicate that deformation rate plays a significant role in the ability of the brittle conductive surface layer to undergo subduction. In the vertical PZW experiments, subduction only occurs at the fastest rates (Fig. 11). In the inclined PZW experiments deformation rate plays a lesser role with subduction occurring over a wider range of rates (Fig. 13). Assuming previously modelled dilational band spreading rates of up to 40 mm/year are comparable to subduction rates (Nimmo 2004; Stemple et al., 2005), Kattenhorn and Prockter (2014) calculated that Europa could have recycled enough surface material in the 40 – 90 Myr surface age time frame through this process (at a cumulative rate of 0.34 – 0.77 km^2/yr). These rates are directly tied to the forces of icy shell dynamics, which drive the mobile lid similar to ridge-push, slab-pull, and basal shear stresses of terrestrial subduction systems (Kattenhorn and Prockter, 2014). Understanding the forces that initiate and drive subduction is of fundamental importance, yet very little, if any, is known about them (Kattenhorn and Prockter, 2014). Although subduction on Earth is similar to the inferred subduction on Europa in that it is driven primarily by density contrasts of the two plates, the specifics of subduction on Europa are likely different. The density difference between the inferred brittle conductive ice (~943 kg/m^3) and the warmer convecting subsurface ice (~920 kg/m^3) is sufficient to subduct the surface layer (Kattenhorn and Procter, 2014). Stresses to initiate and more importantly drive subduction need to reach magnitudes of ~10 MPa to overcome the

compressive strength of the ice shell (Pappalardo and Davis, 2007). Although still poorly understood (e.g. see Bills et al., 2009), diurnal tidal stress does not seem to play a significant role in the subduction process on Europa, because this mechanism usually does not exceed stresses of 90 kPa (Wahr et al., 2009). However, diurnal tidal stress could be responsible for driving subsurface ice convection (Pappalardo et al., 1998). This stress could be responsible for many of the surface fractures observed on Europa (e.g., Kattenhorn and Hufford, 2009 and references therein), which could serve as PZWs where subduction could start. Evidence for non-synchronous rotation (NSR) exists on Europa and likely plays a significant role in Europa's surface processes (Greenberg et al., 1998; Sotin et al., 2009; Kattenhorn and Hurford, 2009), because it produces stresses much larger than diurnal tidal stress, up to several MPa (Bills et al., 2009). Another mechanism that could create large stresses of several MPa is true polar wander (TPW) (e.g. Sarid et al., 2002; Matsuyama and Nimmo, 2008; Schenk et al., 2008) and may even accompany NSR (Bills et al., 2009). NSR is potentially a source of relatively short time scale, high magnitude stress, while TPW is potentially a source of longer time scale, high magnitude stress (Matsuyama and Nimmo, 2008). The exact crustal responses to these stresses depend heavily on Europa's ice rheology, which is also poorly understood.

In this study, the experiments indicate that the orientation of the PZW plays a significant role on how deformation rates affect subduction (see 4-3). For vertical PZWs subduction only occurs at the fastest deformation rates (Fig. 12). Thus, NSR alone may not be sufficient for the creation of such a large thrust fault to physically initiate subduction on Europa if only a vertical zone of weakness exists and may also require the contribution of other mechanisms such as ridge-push (Kattenhorn and Prockter, 2014).

However, as indicated by the inclined PZW experiments, if an inclined zone of weakness exists on the surface of Europa, less stress would be needed to overcome frictional resistance along the initial thrust that physically initiates subduction (see Section 4-3 for more detail). Thus, at present, NSR seems to represent the best mechanism that has the potential to create high stress over relatively short time periods, which could drive brittle deformation. In general, deformation behavior becomes less ductile (more brittle) as strain-rate increases. However, stress created by TPW, despite being potentially of equal magnitude to NSR, is spread out over longer time scales, and thus strain-rate is likely lower than NSR, which may allow the icy shell to accommodate that stress by undergoing viscous relaxation. Therefore, NSR could represent the driving mechanism for processes that recycle aging terranes. As it is also likely the driving force responsible for the creation of new surface material at dilational bands (Prockter and Patterson, 2009) it, thus, plays a vital role in Europa's surface geologic processes.

4-3 Effect of Orientation of the PZW

Many natural zones of weakness are present on the Europan surface. These zones of weakness can form through exogenic (e.g., impacts) and endogenic processes (e.g., extension, cryovolcanism, ice-fatigue) that create lineaments such as ridges, troughs, and cycloidal bands (Pappalardo et al., 1999, Kattenhorn and Hufford, 2009 and references therein) where subduction could potentially begin. A variety of orientations of these zones of weakness are likely present on Europa, ranging from vertical or near vertical faults or cracks in some ridge formation conceptual models (e.g., Greenberg et al., 1998; Head et al., 1999; Tufts et al., 2000, Fagents, 2003) to inclined faults that are observed

primarily as normal faults (Prockter and Patterson, 2009; Kattenhorn and Hurford, 2009). Therefore, the vertical PZW experiments and the inclined PZW experiments represent two scenarios of possible orientations to test their effect on subduction.

The results of the experiments indicated that the inclination of the PZW plays a crucial role in the ability of a brittle conductive layer to undergo subduction. It was much more difficult to initiate subduction at vertical PZWs compared to inclined PZWs. Inclined PZWs allowed subduction to occur over a much wider range of deformation rates compared to vertical PZWs (see section 4-2). In an inclined PZW experiment the resolved normal stress is less than the resolved shear stress times the coefficient of friction, promoting offset along the inclined PZW, whereas the balance of shear and normal stresses prevents fault displacement across a vertical PZW.

Further, the orientation of the PZW greatly influences the pre-subduction and post-subduction morphology (see section 4-4 for a detailed comparison of model surface morphology and Europan surface features). In the vertical PZW experiments, subduction is mostly preceded by or accompanied by, long-wavelength folding, which is not widely observed on Europa. The overturning of blocks has been observed on Europa (Fig. 14), and occasionally accompanies subduction in the vertical PZW experiments (Fig. 15). However, convection of the subsurface ice can effectively erase large scale topography variations in geologically instantaneous time frames (Nimmo and Manga, 2009). Therefore, it may be possible that subduction has or does occur at vertical PZWs on Europa, and obvious evidence of the resultant topography has been effectively erased.

While the experimental results do not preclude the initiation of subduction at vertical or near vertical PZWs on the surface of Europa, i.e., at vertical or near vertical

faults and cracks, subduction would be much more likely to initiate at inclined PZWs, for example at the numerous normal faults that have been observed on the Europan surface (Prockter and Patterson, 2009; Kattenhorn and Hurford, 2009).

The depth of the PZW also seems to play an important role in subduction initiation. With one exception, all experiments had PZWs that penetrated through the entire conductive layer thickness. The exception, experiment "2.5 cm at 30 cm/hr vertical half cut" did not result in subduction (Appendix Fig. X), while the "2.5 cm at 30 cm/hr vertical full cut" did result in subduction (Appendix Fig. I). Inclined half cuts were not tested due to time constraints. Our half-cut experiment only penetrated the solid upper brittle layer, but not the lower solid plastic layer (Fig. 2c). Consequently, to initiate subduction on Europa, a fault (or zone of weakness) likely needs to breach the entire solid (brittle + plastic), conductive ice surface layer. It is unlikely that diurnal tidal stresses, with their low magnitudes, can result in cracks or faults that penetrate beyond a few hundred meters (Crawford and Stevenson, 1988; Hoppa et al., 1999; Lee et al., 2003). Whether this depth is sufficient to completely penetrate the entire solid conductive layer is unclear. NSR, on the other hand, has the potential to create enough stress (see 4-2) to fracture through the entire brittle, conductive surface ice layer.

4-4 Morphology Comparison

On the surface of Europa, little evidence has been found for large-scale contractional features sufficient to counter-balance the creation of new surface material at dilational bands (Kattenhorn and Prockter, 2014). Although rare, convergence bands imply high contractional strain in some areas on Europa (Figueredo, 2002; Sarid et al.,

2002), however, the topography expected to accompany this contractional strain is lacking (Kattenhorn and Prockter, 2014). No substantial surface erosion mechanism has been proposed that could explain this lack of topography. In the sections below, the experimental morphologies are compared to those observed on the Europan surface.

4-4-1 Subduction Zone Morphology

In the conceptual model proposed by Kattenhorn and Prockter (2014) (Fig. 1), subduction is accompanied by the development of so-called subsumption bands with a hummocky surface texture that they propose forms similarly to accretionary wedges found in terrestrial subduction zones. However, the bands observed by Kattenhorn and Prockter (2014) are asymmetric: that is, one side is hummocky while the other is smooth. They do not propose a mechanism for this asymmetry. In the experiments, bands with similar hummocky/smooth asymmetric texture form when warmer subsurface wax migrates up through the subduction fault, extrudes onto the surface, and is subsequently deformed on the subducting slab by the ongoing subduction process (Fig. 16). Conversely, the subsurface wax that is extruded onto the over-riding slab remains un-deformed throughout the experiment. The result is an asymmetrical smooth/hummocky surface feature that closely resembles the asymmetric subsumption bands observed on Europa (Fig. 17) (Kattenhorn and Prockter, 2014). Many of the other experiments result in similar hummocky surface geometries, independent of the orientation of the PZW. Therefore, a similar process could explain the hummocky textured bands occurring on Europa when less dense underlying warmer ice is extruded onto the surface along the subduction thrust fault. Further, asymmetric smooth/hummocky bands are potentially an easily recognizable marker for ongoing or recently ceased subduction on Europa.

Topography across the experimental subduction zones depends almost exclusively on the orientation of the PZW (Fig. 18). All our experiments with inclined PZWs result in final topographic profiles across the subduction zone similar to that observed by Kattenhorn and Prockter (2014). Despite the lack of obvious high topographic variation, the overriding plate in many of the experiments exhibits broad regional uplift across the subduction zone (Fig. 19). Regional uplifts have been observed on Europa (Prockter et al., 2002), albeit not yet in conjunction with subduction zones. However, it is likely that regional uplift resulting from subduction zones may decrease with time considering the relaxation timeframes (Nimmo and Manga, 2009), and/or isostatic compensation (Kattenhorn and Prockter, 2014). In contrast, in most of our vertical PZW experiments, subduction initiation is accompanied or preceded by long-wavelength folding resulting in high topography. Such high topographic features have not yet been observed on Europa. Convection in the subsurface ice layer can potentially erase topography variations on Europa, as previously discussed (Nimmo and Manga, 2009). In models where the analogue material is too strong compared to the natural system, higher topography in the experiments is common. In some of the vertical PZW experiments, however, subduction is accompanied by the overturning of small and large scale surface blocks, resulting in subduction without long-wavelength folding (Fig. 15; Appendix Fig. I) and instead exhibits a final topographic profile like that observed by Kattenhorn and Prockter (2014) (Fig. 16a). This is evidence that subduction could be initiated at vertical PZWs without the predicted long-wavelength folding. The numerous ridges observed on Europa could act as fracture zones to facilitate overturning of plates (small or large) during shortening. In fact, evidence for block overturning does exist on Europa, for example, in the

Conamara Chaos region (e.g., Collins and Nimmo, 2009). In this region, some blocks and plates appear to have been at least partially overturned and/or dip into the subsurface (Fig. 13). While this region is not associated with subduction processes (and we do not suggest this here either), it does indicate that blocks and plates can move independently from the main surface plates and potentially overturn. In addition, in one of our experiments, the subduction zone developed a transform fault (Fig. 16b and App. A Fig. Mc). This is most likely the result of a slightly kinked initial orientation of the vertical PZW. Its kink serves as the nucleation site for the transform fault (App. A Fig. Ma). While many of the ridges on Europa are straight, numerous examples of similar kinks exist (e.g., in double ridges or cycloids; Prockter and Patterson, 2009) and, thus, it could be possible for similar subduction geometries to develop on Europa. Therefore, evidence for subduction processes involving vertical PZWs cannot completely be disregarded based solely on morphology.

In summary, while some of the vertical PZW experiments result in topographic profiles remarkably similar to those observed on Europa, most of the vertical PZW experiments that result in subduction do not (e.g. see App. Figs. G, J, K, L). This fact, combined with numerous observed inclined PZWs on Europa, the absence of evidence for widespread large-scale folding or overturning, and consideration of relaxation time frames, indicates that, if subduction does occur on Europa, it would initiate more likely at inclined PZWs rather than at vertical PZWs. Thus, the inclined PZW experiments are likely more representative of potential subductions zones on Europa like those observed by Kattenhorn and Prockter (2014). Subsumption bands as well as convergence bands observed on Europa (Kattenhorn and Prockter, 2014; Sarid et al., 2002) could be used as

an indicator of past or present subduction zones. They could have formed either from a process similar to that of an accretionary wedge in terrestrial subduction zones or, alternatively, from upwelling of warmer, less dense, subsurface material that continued to be deformed during the ongoing subduction process, as in the experiments.

4-4-2 Ductile Roll Back Morphology

Besides potential subduction zones and convergence bands, little evidence exists on Europa for other large-scale contraction mechanisms that could counter-balance the creation of new surface areas at dilational bands (Kattenhorn and Prockter, 2014; Sarid et al., 2002). However, evidence exists that double ridges on Europa exhibit limited lateral offset and contraction (Bader and Kattenhorn, 2008) and may even behave non-rigidly (Patterson et al., 2006). Recent work by Culha et al. (2014) demonstrates that double ridges on Europa can accommodate some shortening ductilely and implies that some surface material could get recycled at these ridges. The underlying shortening and recycling mechanism, however, is unknown. Ductile roll back, which occurs in almost all our 1 cm conductive solid layer experiments, does provide a potential underlying mechanism. Ductile roll back accommodates most of the experimental contraction and recycles a significant amount of surface material at the PZW. This process results in relatively low topographic variation across the experimental PZW, producing ridges that are morphologically similar to those observed on Europa (Fig. 20) but that exhibit less relief (Fig. 20b, c),. The total surface removal at the observed double ridges on Europa today (Culha et al., 2014) is significantly less than that observed by Kattenhorn and Prockter (2014) at subduction zones. It is possible however, that ductile roll back could have occurred early in Europa's geologic history if the icy shell was thinner and could

have recycled significantly more surface material as indicated in the experiments. However, the evidence for this older process could be difficult to recognize today, as further resurfacing and deformation have modified the surface of Europa, likely erasing older expressions of this process (Culha et al., 2014). Thus, based on current observations, ductile roll back at double ridges is plausible. If ductile roll back did occur at some double ridges (past and/or present), even if playing a limited role today, this process in combination with subduction, could represent an additional recycling mechanism that operates(ed) on Europa.

4-5 Paraffin Wax and Scaling

Ideally, analogue models should be geometrically, kinematically, and dynamically similar to the natural system. Paola et al. (2009) explored this concept in detail and noted the "unreasonable effectiveness" of un-scaled stratigraphic and geomorphic experiments because these un-scaled experiments appear strikingly morphologically similar to natural systems. Many important aspects of natural processes are scale independent and operate over a wide range of scales, e.g., grain size in fluvial experiments (Paola et al., 2009). Therefore, analogue experiments need only include enough relevant dynamics to serve as a plausible test of the natural system, are not required to be fully scaled models to gain scientifically useful insight into that system (Paola et al., 2009). These experiments are not fully scaled models, and are therefore not "simulations" of Europan processes. Rather, the experiments serve as a theoretical framework through which to examine subduction initiation processes on Europa, and aid in the interpretation of observed features on Europa.

We investigated many avenues for modeling Europa in a physical laboratory setting and found no substance that would fully scale dynamically, kinematically, and geometrically to ice on Europa, while also having a strongly temperature dependent response to deformation at laboratory conditions. The viscosity of paraffin wax is strongly dependent on temperature (Rosseletti et al., 1999; Ukrainczyk et al., 2010) within a temperature range that can easily be achieved in a laboratory setting (Manga and Sinton, 2004). Thus, it has been previously used as a brittle-ductile analogue modeling material for terrestrial continental extension (Brune and Ellis, 1997). In addition, Manga and Sinton (2004) used paraffin wax as a brittle-ductile analogue to model the formation of bands and ridges on Europa. Since proposed subduction on Europa is fundamentally a relationship between heat transfer (and by proxy, viscosity) and deformation, we can thus perform lab experiments using paraffin wax, which can be compared to brittle-ductile deformation of the brittle solid icy surface and the underlying ductile warmer ice on Europa (Manga and Sinton, 2004).

Dynamic similarities between analogue models and the natural system require that the mechanical equations of state that relates differential flow stress to strain rate only differ in the proportionality constant (Manga and Sinton, 2004). For power-law creep, where the strain rate $\dot{\varepsilon}$ is proportional to σ^n (with σ = differential stress), paraffin wax has a stress exponent of n = 2.4. This value is similar to the power-law creep stress exponent for ice on Europa, which ranges from n = 1.8 to 4 (Nimmo, 2004). Grain-boundary sliding accommodated basal slip is thought to be the most likely dominant deformation mechanism on Europa (Nimmo, 2004) and has n = 1.8; basal slip accommodated grain-boundary sliding has n = 2.4 (Goldsby and Kohlstedt, 2001). Thus, wax in the analogue

model and ice on Europa should respond similarly to stress as shown by Manga and Sinton (2004) and Nimmo (2004).

Current estimates for viscosity of pure water ice present on icy moons range from 10^{13} Pa·s (warmer, convecting ice) to 10^{21} Pa·s (cold, brittle ice) (Showman et al., 2004; Jara-Orue and Vermeersen, 2011; Leonard et al., 2017). Paraffin wax has viscosities ranging from 10 Pa·s (liquid) to 10^{10} Pa·s (Rossetti et al., 1999) and, thus, the viscosity change from liquid to solid is similar in magnitude between both mediums.

On Europa, the ice shell can be separated into a thin, brittle surface layer with a thickness of L that conducts heat, and the remaining underlying warmer bulk subsurface ice layer that convects on a geologic time scale (Pappalardo et al., 1998; Prockter et al., 2002; Showman and Han, 2004; Manga and Sinton, 2004; Schuman et al., 2009; Kattenhorn and Prockter, 2014). Heat transport within the solid layer of wax, with a relative thickness of L, is dominated by conduction and therefore, can be assumed to be equivalent to the thickness of the solid ice layer on Europa that also transports heat primarily by conduction (Manga and Sinton, 2004). The molten subsurface wax layer in the experiments convects heat similar to the convecting warmer subsurface ice layer on Europa (Fig. 2a,b) (Manga and Sinton, 2004). The solid conductive surface ice layer on Europa can further be divided into a brittle layer and a plastic layer (see introduction, Fig. 2b) (Billing and Kattenhorn, 2005; Nimmo and Manga, 2009; Schubert et al., 2009). Thickness of the elastic lithosphere on Europa, Te (representing the depth of brittle to plastic transition), is controlled mainly by the brittle portion of that layer under equilibrium conditions (Manga and Sinton, 2004; Nimmo and Manga, 2009). Depending on the strain-rate and deformation mechanism, Te on Europa is estimated to be between

0.2 times the thickness of the conductive surface ice layer (L) (i.e., 0.2L) and 0.6L (Nimmo et al., 2002; Nimmo and Manga, 2002). Paraffin wax undergoes a solid-solid phase transition at ~35°C (Manga and Sinton, 2004; Ukrainczyk et al., 2010), in which the warmer solid phase behaves plastically, while the colder phase behaves brittlely (Manga and Sinton, 2004). Thus, the solid wax can be divided into two regions similar to the conductive ice layer on Europa with: (a) an upper region that behaves brittlely, in which strain is accommodated by forming cracks during compression (e.g., Appendix Fig. G, J); and (b) an underlying region that behaves plastically, in which strain is accommodated mostly by ductile flow during compression (Fig. 2b). The transition from (a) to (b) can be observed in the experiments by a transition in wax color from white (the brittle layer) to translucent (plastic layer) (Fig. 2c). By assuming a linear temperature gradient, Manga and Sinton (2004) showed that the thickness Te in their analogue experiments is 0.3L. In our experiments, however, we cannot assume a linear temperature gradient. Based on the temperature measurements (Table 4) of the box air (T_{air}) and the solid (brittle) layer at a depth of ~2mm ($T_{brittle}$) and considering the melting temperature of the paraffin wax at ~53°C (T_{liquid}), the temperature gradient profile of the experiments follows an exponential function (Fig. 21) with:

$$f(x) = a^{bx} \qquad \text{Eq. 2}$$

rather than a linear trend assumed by Manga and Sinton (2004). However, Te in our experiments ranges from 0.43L and 0.4L depending on the thickness of the conductive layer (Table 5) and hence, is comparable to Te on Europa and in experiments by Manga and Sinton (2004).

In laboratory subduction experiments, a low Reynolds number (Re) is essential (Schellart and Strak, 2016). The Reynolds number is defined as:

$$Re = \frac{pdv}{n} \qquad \text{Eq.3}$$

where p is density of the ambient fluid, d is the characteristic length scale (in our experiments, conductive layer thickness), v is characteristic velocity, and n is the viscosity of the ambient fluid (Schellart and Strak, 2016). In such experiments, Re needs to be << 1 so that laminar flow around the subducting slab can be assumed without eddy formation around the slab (Hudson and Dennis, 1985; Schellart, 2008; Schellart and Strak, 2016). The calculated Reynolds numbers for Europa and our experiments are 8.17×10^{-16} and 1.97×10^{-4}, respectively (Table 6); both values are <<1.

In this study, the analytical framework aims to understand resurfacing processes in a single medium where temperature alone is the major controlling factor for its mechanical behavior. Therefore, the experiments need only to include enough relevant dynamics to serve as a plausible test (Paola et al., 2009). For more details on scaling properties of wax to ice on Europa, see Manga and Sinton (2004). Based on the above discussion, paraffin wax represents the best available material to study Europan surface processes in analogue experiments.

4-6 Limitations

Europa has one of the most complex geologic surfaces in our Solar System. In this study, we have attempted to greatly simplify a specific phenomenon into a few parameters that are most likely important to subduction on Europa. While the

experiments are a plausible test for Europan subduction as a basic process, there are important differences between the two systems. Many factors likely influence ice shell tectonics and the resulting observed morphology on Europa, including curvature, ice grain size, ice grain to grain interactions, shear heating, total amount and composition of ice contaminants (brine), ice fatigue, cyrovolcanic processes, space weathering, and probably other unknown factors (Manga and Sinton, 2004; Moor et al., 2009). Simulating these processes in our experiments is outside the scope of this study. In addition, the Europan surface is completely covered by deformation structures, each a potential PZW for further deformation initiation. Our experimental wax surface is smooth and only includes one large imposed PZW.

4-7 Future Work

Future work should first include testing of more complex PZW geometries. Multiple PZWs, PZWs sub-parallel to the displacement direction, and more diverse inclined angles are some examples. Additionally, given that the surface of Europa is completely covered with PZWs, experiments with similar geometries should be tested: that is, the surface covered with PZWs in a variety of orientations, to study how this complex geometry impacts subduction initiation. Future experiments should also consider utilization of both sides of the moving wall: this way one experiment could potentially test a variety of conditions for compression and extension simultaneously, though this will likely require a larger plexiglass box. Finally, future work should include testing a more diverse range of displacement rates beyond the 10 cm/hr, 20 cm/hr, and 30 cm/hr rates examined here. This could include testing a variety of rates within one experiment.

For example, an experiment could first have several rounds of low boundary displacement rate back and forth (north and south) moving wall motion, analogous to diurnal tidal stresses, followed by a period of high boundary displacement rate motion in one direction, analogous to NSR or TPW.

Additionally, several equipment upgrades should be considered. Making the base of the experiment box out of stainless steel would eliminate the requirement to have a heat array within the box, and would allow for more even heating from below, provided that beneath the stainless steel base, 1 large heat mat could heat the entire base. Further, a more consistent cooling manifold design should be considered, one which more reliably delivers consistent cooling to the experiment surface without near constant adjustments. Finally, including 3D surface scanning technology, such as Microsoft® Kinect, would allow more quantitative analysis of the experiment surface topography throughout an experimental run, and thus should be considered in any future experiments.

5. Conclusions

In this study, we aimed to understand resurfacing processes on Europa through physical analogue experiments using a single medium – wax – where temperature alone is the major controlling factor for its mechanical behavior. We have investigated three basic parameters and their constraints on subduction and subduction initiation: 1) the role of the solid conductive layer thickness on the ability of that layer to undergo subduction, 2) the role of deformation rate in the initiation of subduction, and 3) the role of dip angle of the pre-existing zone of weakness on subduction initiation.

Subduction does not occur for conductive layer thicknesses below 1 cm in our experiments; therefore we hypothesize that solid ice layer thickness influences subduction initiation on Europa i.e., below a minimum thickness of the solid conductive ice layer subduction would not initiate. Consequently, if widespread subduction does occur on Europa (past or present), conductive ice layer thickness is unlikely to be on the thinnest end of the estimated 0.1 – 6 km range. Above some minimum thickness, subduction is possible over a range of solid conductive surface thicknesses, deformation rates, and PZW dip angles in the experiments, although higher deformation rates and inclined PZWs result more readily in subduction. Experimental results imply that subduction could also initiate within a range of conditions on Europa. To overcome the compressive strength of the ice shell at depth, subduction initiation would most likely be caused by stresses induced by non-synchronous rotation and/or by true polar wander. In addition, our result of the "half-cut" (partial PZW) experiment indicates that a PZW must penetrate throughout the entire conductive lid for initiation of subduction to occur. This result supports the hypothesis of non-synchronous rotation and/or true polar wander as a source for the stress needed to initiate and drive subduction on Europa.

While subduction in some of the vertical PZW experiments results in topographic profiles remarkably similar to those observed on Europa, most of the vertical PZW experiments do not. This, combined with numerous observed inclined PZWs on Europa, the absence of evidence for widespread large-scale folding or overturning, and consideration of relaxation time frames, suggests that subduction on Europa initiates at inclined PZWs rather than at vertical PZWs.

The observed asymmetric subsumption bands on Europa (Kattenhorn and Prockter, 2014) and the observed regional uplift (Prockter et al., 2002) can be used as indicators for past or present subduction zones. The asymmetric subsumption bands most likely formed from upwelling of less dense subsurface material. On the down-going plate this new material is subsequently deformed during the ongoing subduction process resulting in hummocky textures, while the material on the overriding plate remains un-deformed (smooth). The regional uplift could indicate an overriding plate during ongoing or recently ceased subduction.

Ductile roll back represents another recycling process that accommodated significant boundary displacement in our experiments. This process, in which surface material gets pushed into the subsurface where it eventually is subsumed, results in experimental morphologies similar to double ridges on Europa and, thus, could explain the shortening observed at these surface features. It is likely that ductile roll back only plays a minor role in resurfacing at double ridges today but could have played a larger role earlier in the history of Europa, if the conductive ice layer was thinner. In addition, if the icy shell is currently heterogeneous in thickness, it is possible that ductile roll back could play a more important resurfacing role today in local areas with a thin icy layer.

In summary, according to our results, significant resurfacing on Europa is possible tectonically, either by subduction above some minimum conductive ice layer thickness or by ductile roll back below that thickness. These two processes can operate over a wide range of conditions on Europa and throughout geologic time, and may represent the dominant mechanisms for recycling a significant portion of aging surface material on Europa. Consequently, other more exotic re-surfacing mechanisms, such as

large impacts and widespread cryo-volcanism, are not required at significant magnitudes to explain the 40-90 Ma young surface of Europa that is observed today. In addition, asymmetric subsumption bands and regional uplift can be used as indicators to located past or presently ongoing subduction, which could be useful for future exploration mission to Europa.

References

Allupeddinti, D., and A. K. McNamara. 2017. Formation of Ice-Shell: Geodynamical Modeling of Temporal Variation of Shell Thickness in Two-Phase Systems. *Lunar and Planetary Science XLVIII (2017).*

Anderson, E. M. 1951 *The Dynamics of Faulting and Dyke Formation with Applications to Britain*. Edinburgh, Oliver and Boyd.

Andreas, E. L. 2007. New Estimates for the Sublimation Rate for Ice on the Moon. *Icarus* 186, no. 1: 24-30.

Bader, C. E., and Simon A. Kattenhorn. 2008. Formation Mechanisms of Europan Ridges with Apparent Lateral Offsets. In *Lunar and Planetary Science XXXIX*,

Billings, S. E., and S. A. Kattenhorn. 2005. The Great Thickness Debate: Ice Shell Thickness Models for Europa and Comparisons with Estimates Based on Flexure at Ridges. *Icarus* 177, no. 2: 397-412.

Bills, Bruce, G., F. Nimmo, Ö Karatekin, T. V. Hoolst, B. Levrard, and J. Laskar. 2009. Rotational Dynamics of Europa. In *Europa*, edited by R. T. Pappalardo, W. B. McKinnon and K. Khurana, 119-36: University of Arizona Press

Bland, M. T., R. A. Beyer, and A. P. Showman. 2007. Unstable Extension of Enceladus' Lithosphere. *Icarus* 192, no. 1: 92-105.

Boutelier, D., C. Schrank, and A. Cruden. 2008. Power-Law Viscous Materials for Analogue Experiments: New Data on the Rheology of Highly-Filled Silicone Polymers. *Journal of Structural Geology* 30, no. 3: 341-53.

Bray, Veronica J., Gareth S. Collins, Joanna V. Morgan, H. Jay Melosh, and Paul M. Schenk. 2014. Hydrocode Simulation of Ganymede and Europa Cratering Trends – How Thick Is Europa's Crust? *Icarus* 231: 394-406.

Brune, J. N., and M. A. Ellis. 1997 Structural Features in a Brittle-Ductile Wax Model of Continental Extension. *Nature* 387, no. 6628: 67-70.

Canup, R. M., and W. R. Ward. 2009. Origin of Europa and the Galilean Satellites. In *Europa*, edited by R. T. Pappalardo, W. B. McKinnon and K. Khurana: University of Arizona Press.

Carr, M. H., M. J. S. Belton, C. R. Chapman, Merton E. Davies, P. E. Geissler, R. Greenberg, A. S. McEwen*, et al.* 1998. Evidence for a Subsurface Ocean on Europa. *Nature* 391: 363-65.

Chyba, C. F., Whitmire, D. P., Reynolds. R. 2002. Planetary Habitablility and the Origins of Life. In *Protostars and Planets IV*, edited by Mannings, V., Boss, A.P., Russell, S.S.: University of Arizona Press.

Chyba, C. F., and Phillips, C. B. 2001. Possible Ecosystems and the Search for Life on Europa. *PNAS* 98: 801-04.

Collins, G. C., and F. Nimmo. 2009. Chaotic Terrain on Europa. Chap. 259 In *Europa*, edited by R. T. Pappalardo, W. B. McKinnon and K. Khurana, 259-81: University of Arizona Press.

Cox, R., and A. W. Bauer. 2015. Impact Breaching of Europa's Ice: Constraints from Numerical Modeling. *Journal of Geophysical Research-Planets* 120, no. 10: 1708-19.

Crawford, G. D., and D. J. Stevenson. 1988. Gas-Driven Water Volcanism and the Resurfacing of Europa. *Icarus* 73, no. 1: 66-79.

Culha, C., A. G. Hayes, M. Manga, and A. M. Thomas. 2014. Double Ridges on Europa Accommodate Some of the Missing Surface Contraction. *Journal of Geophysical Research-Planets* 119, no. 3: 395-403.

Fagents, S. A. 2003. Considerations for Effusive Cryovolcanism on Europa: The Post-Galileo Perspective. *Journal of Geophysical Research-Planets* 108, no. E12.

Figueredo, P. H., R. Greeley, S. Neuer, L. Irwin, and D. Schulze-Makuch. 2003. Locating Potential Biosignatures on Europa from Surface Geology Observations. *Astrobiology* 3, no. 4: 851-61.

Goldsby, D. L. and D. L. Kohlstedt. 2001. Superplastic deformation of ice: Experimental observations. *Journal of Geophysical Research-Solid Earth* **106**(B6): 11017-11030.

Greenberg, R., P. E. Geissler, G. Hoppa, B. Tufts, and D. D. Durda. 1998. Tectonic Processes on Europa, Tidal Stresses, Mechanical Response, and Visible Features. *Icarus* 135: 64-78.

Greenberg, R., M. A. Leake, G. V. Hoppa, and B. R. Tufts. 2003. Pits and Uplifts on Europa. *Icarus* 161, no. 1: 102-26.

Hand, K., and C. Chyba. 2007. Empirical Constraints on the Salinity of the Europan Ocean and Implications for a Thin Ice Shell. *Icarus* 189, no. 2: 424-38.

Harada, Y., and K. Kurita. 2006. The Dependence of Surface Tidal Stress on the Internal Structure of Europa: The Possibility of Cracking of the Icy Shell. *Planetary and Space Science* 54, no. 2: 170-80.

Head, J. W., R. T. Pappalardo, and R. Sullivan. 1999. Europa: Morphological Characteristics of Ridges and Triple Bands from Galileo Data (E4 and E6) and Assessment of a Linear Diapirism Model. *Journal of Geophysical Research-Planets* 104, no. E10: 24223-36.

Hoppa, G., B. Tufts, R. Greenberg, and P. E. Geissler. 1999. Strike-Slip Faults on Europa: Global Shear Patterns Driven by Tidal Stress. *Icarus* 141: 287-98.

Hoppa, G., B. R. Tufts, R. Greenberg, and P. Geissler. 1999. Strike-Slip Faults on Europa: Global Shear Patterns Driven by Tidal Stress. . *Icarus* 141, no. 2: 287-98.

Hoppa, G. V., B. R. Tufts, R. Greenberg, and P. E. Geissler. 1999. Formation of Cycloidal Features on Europa. *Science* 285, no. 5435: 1899-902.

Hudson, J. D., and S. C. R. Dennis. 1985. The Flow of a Viscous Incompressible Fluid Past a Normal Flat-Plate at Low and Intermediate Reynolds-Numbers – the Wake. *Journal of Fluid Mechanics* 160, 369-83.

Hussmann, H., T. Spohn and K. Wieczerkowski. 2002. Thermal Equilibrium States of Europa's Ice Shell: Implications for Internal Ocean Thickness and Surface Heat Flow. *Icarus* **156**: 143-151.

Hussmann, H., and T. Spohn. 2004. Thermal-Orbital Evolution of Io and Europa. *Icarus* 171, no. 2 (Oct): 391-410.

Jara-Orué, Hermes M., and Bert L.A. Vermeersen. 2011. Effects of Low-Viscous Layers and a Non-Zero Obliquity on Surface Stresses Induced by Diurnal Tides and Non-Synchronous Rotation: The Case of Europa. *Icarus* 215, no. 1: 417-38.

Kadel, S. D., F. C. Chuang, R. Greeley, J. M. Moore, and Galileo SSI Team. 2000. Geological History of the Tyre Region of Europa: A Regional Perspective on Europan Surface Features and Ice Thickness. *Journal of Geophysical Research-Planets* 105, no. E9: 22657-69.

Kattenhorn, Simon A., and Terry Hurford. 2009. Tectonics of Europa. In *Europa*, edited by R. T. Pappalardo, W. B. McKinnon and K. Khurana, 199-236: University of Arizona Press.

Kattenhorn, S. A., and L. M. Prockter. 2014. Evidence for Subduction in the Ice Shell of Europa. *Nature Geoscience* 7, no. 10: 762-67.

Katz, R. F., R. Ragnarsson, and E. Bodenschatz. 2005. Tectonic Microplates in a Wax Model of Sea-Floor Spreading. *New Journal of Physics* 7: 37-37.

Kivelson, Margaret G., Krishan K. Khurana, Christopher T. Russell, Martin Vowerk, Raymond J. Walker, and Crhistophe Zimmer. 2000. Galileo Magnetometer Measurements: A Stronger Case for a Subsurface Ocean at Europa. *Science* 289: 1340-43.

Lee, S. W., M. Zanolin, A. M. Thode, R. T. Pappalardo, and N. C. Makris. 2003. Probing Europa's Interior with Natural Sound Sources. *Icarus* 165, no. 1: 144-67.

Leonard, E. J., A. Yin, and R. T. Pappalardo. 2017. Constraining the Viscosity of Enceladus's Ice Shell through the Crater Islands. *Lunar and Planetary Science XLVIII (2017)*, no. 2336.

Leonard, E. J., A. Yin, R. T. Pappalardo, D. A. Patthoff, and J. Lin. 2016. Analyzing Surface Structures on Icy Satellites: A Physical Analogue Modeling Approach. *Lunar and Planetary Science XLVII (2016)*, no. 2278.

Manga, M., and A. Sinton. 2004. Formation of Bands and Ridges on Europa by Cyclic Deformation: Insights from Analogue Wax Experiments. *Journal of Geophysical Research-Planets* 109, no. E9.

Matsuyama, I., and F. Nimmo. 2008. Tectonic Patterns on Reoriented and Despun Planetary Bodies. *Icarus* 195, no. 1: 459-73.

Mitri, Giuseppe, and Adam P. Showman. 2005. Convective–Conductive Transitions and Sensitivity of a Convecting Ice Shell to Perturbations in Heat Flux and Tidal-Heating Rate: Implications for Europa. *Icarus* 177, no. 2: 447-60.

Moore, J. M., G. Black, B. Buratti, C. B. Phillips, J. Spencer, and R. J. Sullivan. 2009. Surface Properties, Regolith, and Landscape Degradation. In *Europa*, edited by R. T. Pappalardo, W. B. McKinnon and K. Khurana: University of Arizona Press.

Nimmo, F. 2004. Dynamics of Rifting and Modes of Extension on Icy Satellites. *Journal of Geophysical Research-Planets* 109, no. E1.

Nimmo, F., L. Prockter, and P. Schenk. 2005. Europa's Icy Shell: Past and Present State, and Future Exploration. *Icarus* 177, no. 2: 293-96.

Nimmo, F., P. Thomas, R. Pappalardo, and W. Moore. 2007. The Global Shape of Europa: Constraints on Lateral Shell Thickness Variations. *Icarus* 191, no. 1: 183-92.

Nimmo, F., P., Manga, M. 2009. Geodynamics of Europa's Icy Shell. In *Europa*, edited by R. T. Pappalardo, W. B. McKinnon and K. Khurana: University of Arizona Press.

Ojakangas, G. W., and D. J. Stevenson. 1989. Thermal State of an Ice Shell on Europa. *Icarus* 81, no. 2: 220-41.

Paola, Chris, Kyle Straub, David Mohrig, and Liam Reinhardt. 2009. The "Unreasonable Effectiveness" of Stratigraphic and Geomorphic Experiments. *Earth-Science Reviews* 97: 1-43.

Pappalardo, R. T., M. J. S. Belton, H. H. Breneman, M. H. Carr, C. R. Chapman, G. C. Collins, T. Denk*, et al.* 1999. Does Europa Have a Subsurface Ocean? Evaluation of the Geological Evidence. *Journal of Geophysical Research: Planets* 104, no. E10: 24015-55.

Pappalardo, R. T., and D.M. Davis. 2007. Where's the Compression? Explaining the Lack of Contractional Structures on Icy Satellites. 108-09.

Pappalardo, R. T., J. W. Head, R. Greeley, R. J. Sullivan, C. Pilcher, G. Schubert, W. B. Moore*, et al.* 1998. Geological Evidence for Solid-State Convection in Europa's Ice Shell. *Nature* 391: 365-68.

Park, R. S., B. Bills, B. B. Buffington, W. M. Folkner, A. S. Konopliv, T. J. Martin-Mur, N. Mastrodemos*, et al.* 2015. Improved Detection of Tides at Europa with Radiometric and Optical Tracking During Flybys. *Planetary and Space Science* 112: 10-14.

Patterson, G. W., J. W. Head, and R. T. Pappalardo. 2006. Plate Motion on Europa and Nonrigid Behavior of the Icy Lithosphere: The Castalia Macula Region. *Journal of Structural Geology* 28, no. 12: 2237-58.

Prockter, L. M., J. W. Head, R. T. Pappalardo, R. J. Sullivan, A. E. Clifton, B. Giese, R. Wagner, and G. Neukum. 2002. Morphology of Europan Bands at High Resolution: A Mid-Ocean Ridge-Type Rift Mechanism. *Journal of Geophysical Research-Planets* 107, no. E5.

Prockter, L. M., and R. T. Pappalardo. 2000. Folds on Europa: Implications for Crustal Cycling and Accommodation of Extension. *Science* 289, no. 5481: 941-3.

Prockter, L. M., and G. W. Patterson. 2009. Morphology and Evolution of Europa's Ridges and Bands. In *Europa*, edited by R. T. Pappalardo, W. B. McKinnon and K. Khurana, 237-58: University of Arizona Press.

Rhoden, A. R., B. Militzer, E. M. Huff, T. A. Hurford, M. Manga, and M. A. Richards. 2010. Constraints on Europa's Rotational Dynamics from Modeling of Tidally-Driven Fractures. *Icarus* 210, no. 2: 770-84.

Rossetti, F., G. Ranalli, and C. Faccenna. 1999. Rheological Properties of Paraffin as an Analogue Material for Viscous Crustal Deformation. *Journal of Structural Geology* 21, no. 4: 413-17.

Roth, L., J. Saur, K. D. Retherford, D. F. Strobel, P. D. Feldman, M. A. McGrath, and F. Nimmo. 2014. Transient Water Vapor at Europa's South Pole. *Science* 343, no. 6167: 171-4.

Sarid, A. R., R. Greenberg, G. V. Hoppa, T. A. Hurford, B. R. Tufts, and P. Geissler. 2002. Polar Wander and Surface Convergence of Europa's Ice Shell: Evidence from a Survey of Strike-Slip Displacement. *Icarus* 158, no. 1: 24-41.

Schellart, W. P., and V. Strak. 2016. A Review of Analogue Modelling of Geodynamic Processes: Approaches, Scaling, Materials and Quantification, with an Application to Subduction Experiments. *Journal of Geodynamics* 100: 7-32.

Schenk, P., I. Matsuyama, and F. Nimmo. 2008. True Polar Wander on Europa from Global-Scale Small-Circle Depressions. *Nature* 453, no. 7193: 368-71.

Schenk, P., and E. P. Turtle. 2009. Europa's Impact Craters: Probes of the Icy Shell. In *Europa*, edited by R. T. Pappalardo, W. B. McKinnon and K. Khurana: University of Arizona Press.

Schenk, P. M. 2002. Thickness Constraints on the Icy Shells of the Galilean Satellites from a Comparison of Crater Shapes. *Nature* 417, no. 6887: 419-21.

Schenk, Paul M., and W. B. McKinnon. 1989. Fault Offsets and Lateral Crustal Movement on Europa: Evidence for a Mobile Ice Shell. *Icarus* 79: 75-100.

Schubert, G., F. Sohl, and Hauke Hussmann. 2009. Interior of Europa. In *Europa*, edited by R. T. Pappalardo, W. B. McKinnon and K. Khurana: University of Arizona Press.

Shoji, D., K. Kurita, and H. K. M. Tanaka. 2011. Constraint of Europan Ice Thickness by Measuring Electromagnetic Emissions Induced by Neutrino Interaction. *Geophysical Research Letters* 38, no. 8

Showman, Adam P. 2003. Numerical Simulations of Convection in Europa's Ice Shell: Implications for Surface Features. *Lunar and Planetary Science XLVIV (2003)*, no. 1806.

Showman, A. P., and L. J. Han. 2004. Numerical Simulations of Convection in Europa's Ice Shell: Implications for Surface Features. *Journal of Geophysical Research-Planets* 109, no. E1.

Sotin, C., and G. Tobie. 2004. Internal Structure and Dynamics of the Large Icy Satellites. *Comptes Rendus Physique* 5, no. 7: 769-80.

Sotin, C., G. Tobie, John Wahr, and W. B. McKinnon. 2009. Tides and Tidal Heating on Europa. In *Europa*, edited by R. T. Pappalardo, W. B. McKinnon and K. Khurana, 85-118: University of Arizona Press.

Stempel, M. M., A. C. Barr, and R. T. Pappalardo. 2005. Model Constraints on the Opening Rates of Bands on Europa. *Icarus* 177, no. 2: 297-304.

Tufts, B. R., R. Greenberg, G. Hoppa, and P. Geissler. 2000. Lithospheric Dilation on Europa. *Icarus* 146, no. 1: 75-97.

Turtle, E. P., and E. Pierazzo. 2001. Thickness of a Europan Ice Shell from Impact Crater Simulations. *Science* 294, no. 5545: 1326-8.

Ukrainczyk, N., S. Kurajica, and J. Šipušić. 2010. Thermophysical Comparison of Five Commercial Paraffin Waxes as Latent Heat Storage Materials. *Chemical and Biochemical Engineering Quarterly* 24, no. 2: 129-37.

Wahr, J., Z. A. Selvans, M. E. Mullen, A. C. Barr, G. C. Collins, M. M. Selvans, and R. T. Pappalardo. 2009. Modeling Stresses on Satellites Due to Nonsynchronous Rotation and Orbital Eccentricity Using Gravitational Potential Theory. *Icarus* 200, no. 1: 188-206.

Williams, K. K., and R. Greeley. 1998. Estimates of Ice Thickness in the Conamara Chaos Region of Europa. *Geophysical Research Letters* 25, no. 23: 4273-76.

Zahnle, K., P. Schenk, H. Levison, and L. Dones. 2003. Cratering Rates in the Outer Solar System. *Icarus* 163, no. 2: 263-89.

Zimmer, C., K. K. Khurana, and M. G. Kivelson. 2000. Subsurface Oceans on Europa and Callisto: Constraints from Galileo Magnetometer Observations. *Icarus* 147, no. 2: 329-47.

Table 1: Average experiment run temperatures, and required initial cooling durations for the 3 three common conductive layer thicknesses tested. Air-box temp temperature is monitored ~5 cm above wax surface, surface wax temperature is monitored ~2 mm below the surface, and sub surface wax temperature is monitored directly above the heat mat array.

Conduct. Layer Thickness	Air Box Temperature (T_{air})	Surface Wax Temperature ($T_{brittle}$)	Sub Surface Wax Temp. (T_{liquid})	Duration of initial cooling
1 cm	-5.0°C	33.5° C	63° C	30-45 min
2 cm	-10° C	23.5° C	60° C	90 min
3 cm	-18° C	18° C	58° C	120 min

Table 2: Solutions for the error calculation $\mathrm{X} - (\mathrm{X}COS\angle) = Error$ for common dip angles observed in the experiments.

Angle	Error
5°	0.02 cm
10°	0.08 cm
20°	0.3 cm
30°	0.67 cm
45°	1.46 cm

Table 3: Summary of results for Vertical PZW experiments, with conductive layer thickness, deformation rate, subduction initiation, percent shortening at subduction initiation, boundary displacement accommodated by subduction, and maximum boundary displacement for each experiment.

Conduct. Layer Thickness	Deformation Rate	Subduction?	% Shortening at Sub. Initiation	Boundary Disp. Accommodated by Subduction	Max. Boundary Displacement
1 cm	10 cm/hr.	No	N/A	N/A	9.5 cm
1 cm	20 cm/hr.	No	N/A	N/A	10 cm
1 cm	30 cm/hr.	No	N/A	N/A	13 cm
1.5 cm	30 cm/hr.	No for 5.5, Yes for Max	4.4 %	9.5 cm	13 cm
2 cm	10 cm/hr.	Yes	3.3 %	2-5.3 cm	6 cm
2 cm	20 cm/hr.	No for 5.5, Yes for Max	16.6 %	2.9 cm	13.3 cm
2 cm	30 cm/hr.	Yes	4.4 %	2.1-5.8 cm	13 cm
2.5 cm	20 cm/hr.	No	N/A	N/A	10.8 cm
2.5 cm	30 cm/hr.	Yes	2.2 %	7.8-12 cm	13 cm
3 cm	10 cm/hr.	No	N/A	N/A	6 cm
3 cm	20 cm/hr.	Partial	4.4 %	1-7.6 cm	11 cm
3 cm	30 cm/hr.	Yes	2.2 %	2-11 cm	13 cm
4 cm	30 cm/hr.	Yes	4.4 %	7-10 cm	14 cm

Table 4: Summary of results for inclined PZW experiments with conductive layer thickness, deformation rate, subduction initiation, percent shortening at subduction initiation, boundary displacement accommodated by subduction, and maximum boundary displacement for each experiment.

Conduct. Layer Thickness	Deformation Rate	Subduction?	% Shortening at Sub. Initiation	Boundary Disp. Accommodated by Subduction	Max. Boundary Displacement
1 cm	10 cm/hr.	No	N/A	N/A	7 cm
1 cm	20 cm/hr.	No	N/A	N/A	11.6 cm
1 cm	30 cm/hr.	No	N/A	N/A	13 cm
2 cm	10 cm/hr.	Partial	2.2 %	4.2 cm	5 cm
2 cm	20 cm/hr.	Yes	2.2 %	11-11.6 cm	11.6 cm
2 cm	30 cm/hr.	Yes	2.2 %	8.5-12.7 cm	13 cm
2.5 cm	30 cm/hr.	Yes	2.2 %	7.75-10 cm	11 cm
3 cm	10 cm/hr.	Yes	2.2 %	6.8-7 cm	7.5 cm
3 cm	20 cm/hr.	Yes	2.2 %	13 cm	13.3 cm
3 cm	30 cm/hr.	Yes	2.2 %	12.3-12.5 cm	13 cm

Table 5: Values of Te for various experiment solid conductive layer thicknesses. Te is defined as elastic thickness of the solid layer: that is, the fraction of total length L that is elastic, below which is plastic. Te on Europa is estimated between 0.2L and 0.6L (Nimmo et al., 2002)

Solid Conductive Layer Thickness	Te	Average Temp. of Wax Surface
1 cm	0.43 L	33.5° C
2 cm	0.40 L	23.5° C
3 cm	0.40 L	18° C

Table 6: Parameters and solutions to Reynolds number calculations for experiments and Europa. [1] Ukrainczyk et al., 2010; [2] Rossetti et al., 1999; [3] Kattenhorn and Prockter, 2014; [4] Showman et al., 2004. [5] Typical thickness of solid layer of wax.

Parameters	Experiments	Europa
Density (p)	790 kg/m^3 [1]	920 kg/m^3 [3]
Length Scale (d)	0.03 m [5]	7000 m [3]
Velocity (v)	8.3x10^{-5} m/s	1x10^{-9} m/s [3]
Viscosity (n)	10 Pa [2]	1x10^{13} Pa [4]
Solutions $Re = \frac{pdv}{n}$	1.97x10^{-4}	8.17x10^{-16}

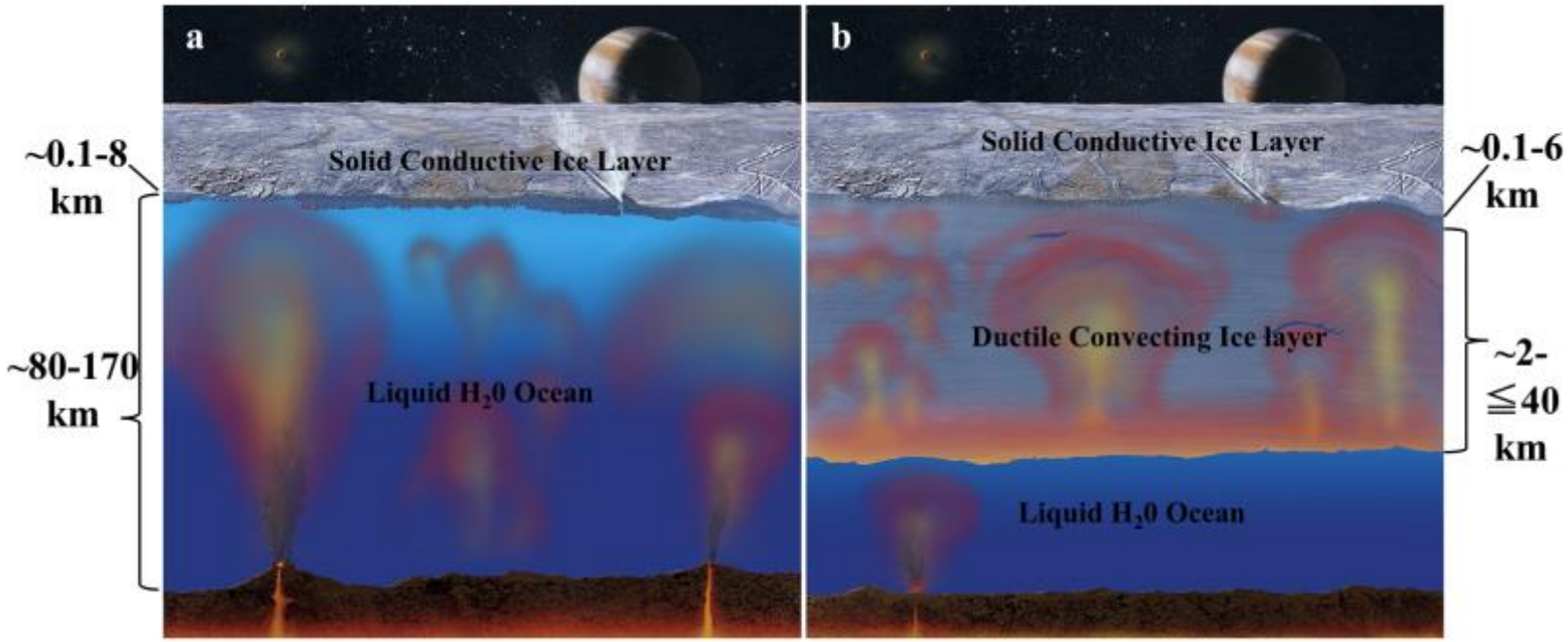

Figure 1: Conceptual cross section of Europa with proposed thickness ranges. a) A thin conductive ice layer overlying a liquid water ocean (thin-ice layer model); b) a thin conductive layer overlying a thicker convecting ice layer (thick- ice layer model), all above a liquid water ocean. The ~80-170 km total H_2O package thickness estimate is independent of thin-shell or thick-shell models. Modified from NASA/JPL, artwork by Michael Carroll.

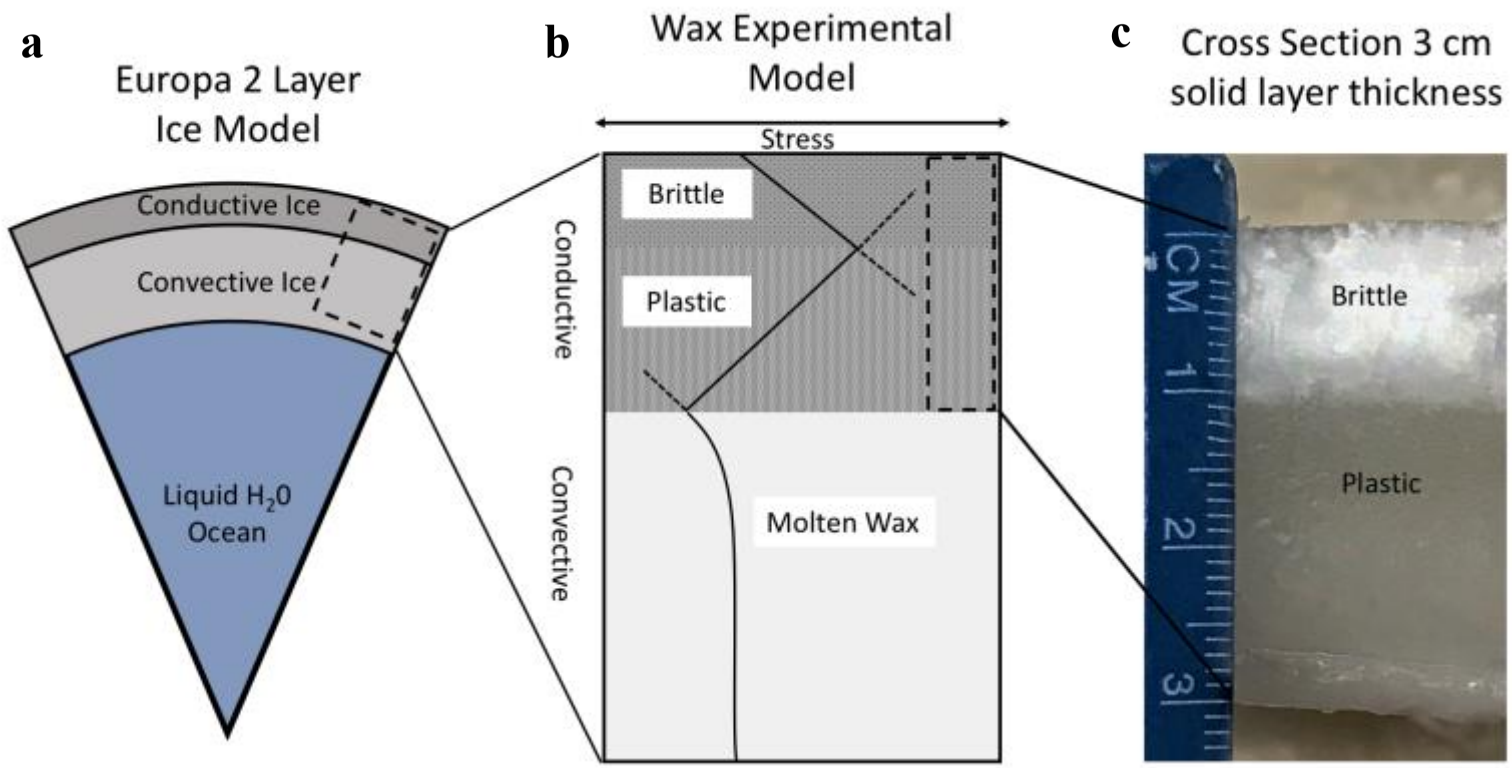

Figure 2: Conceptual cross section model of Europa, wax experiment, and actual cross section of 3 cm conductive layer experiment. (a) Conceptual Europa model.; (b) conceptual wax model; (c) photo of cross section of a 3 cm solid layer experiment. Note solid phase transition from brittle to plastic wax in (c) noted by transition from white upper to more translucent lower layers. (b) adapted from Nimmo and Manga (2009).

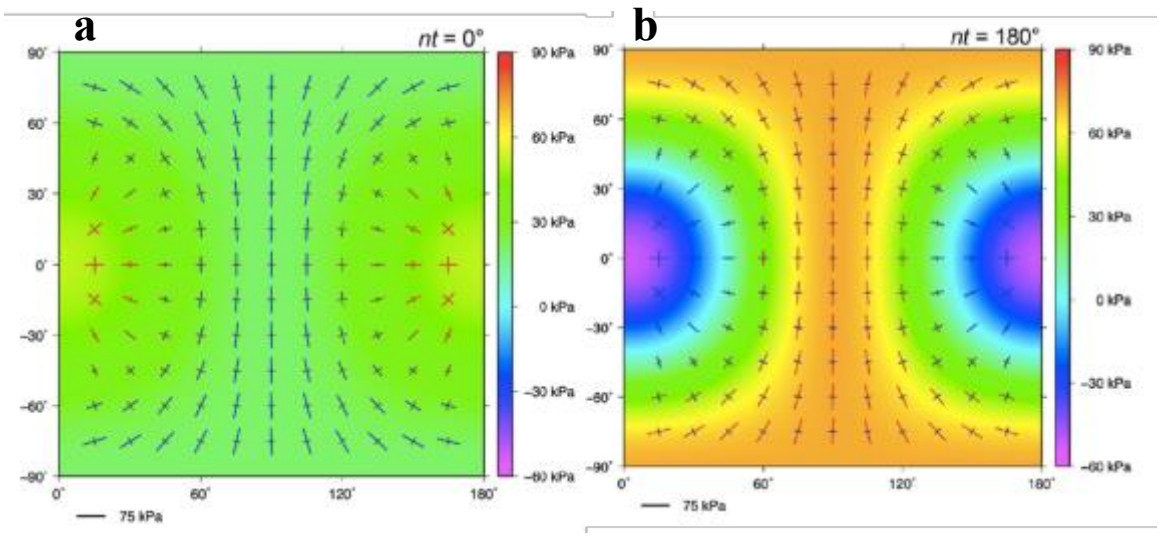

Figure 3: Global stress fields for surface stress during Europa's orbit around Jupiter (diurnal tides) at the beginning (a) and midpoint (b) of each orbit. Line length indicates stress magnitude, line orientation indicates stress orientation, red line color indicates compression, blue line color indicates extension. Back ground color indicates stress magnitude shown on right of each image. Modified from Wahr et al.. 2009.

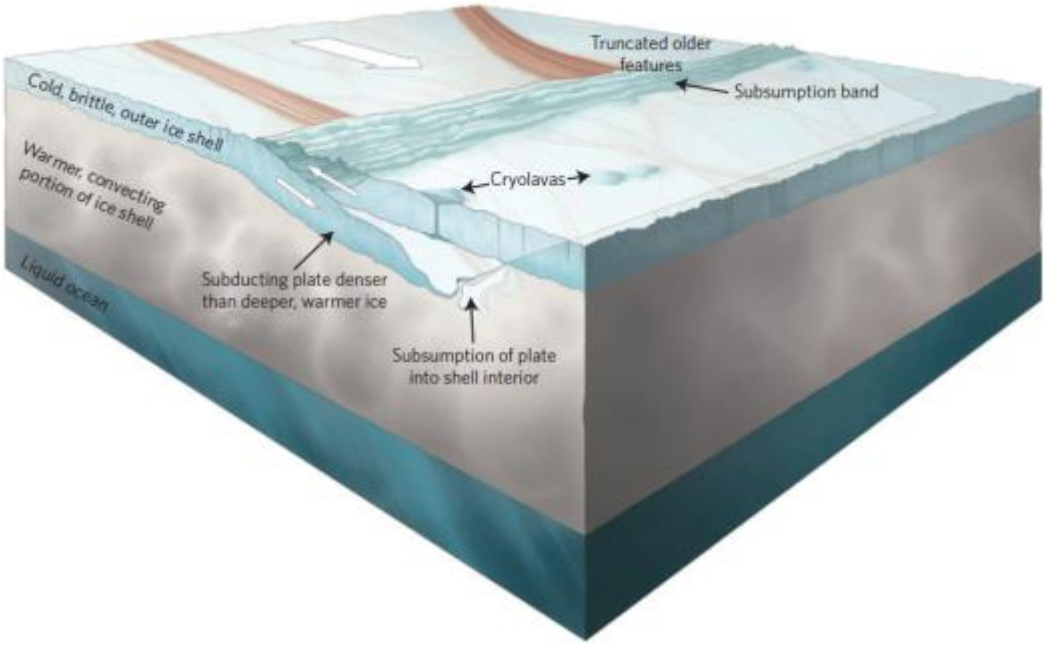

Figure 4: Conceptual model of subsumption proposed by Katttenhorn and Prockter (2014). Colder, denser brittle ice subducts into warmer convecting subsurface ice where it is subsumed, above a liquid water ocean. From Kattenhorn and Prockter (2014).

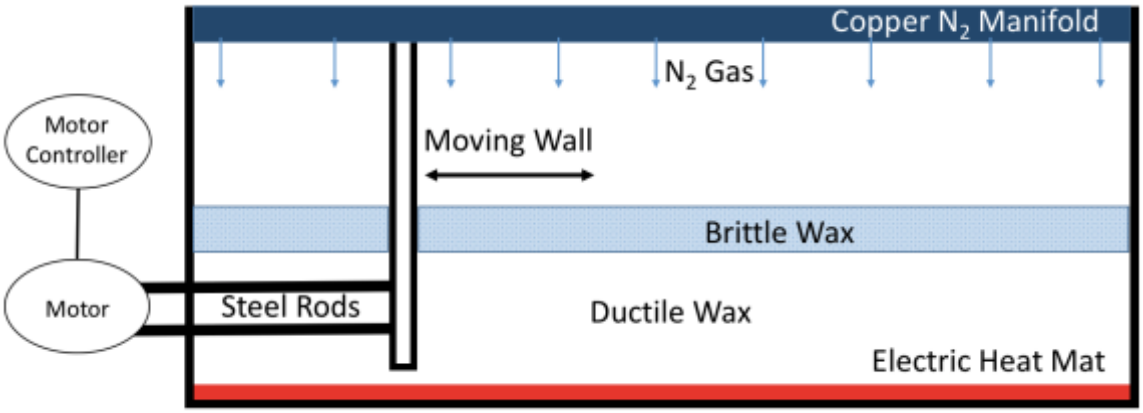

Figure 5: Schematic sketch of experimental apparatus box set up, in cross section. Box dimensions are 61 cm (length) x 58.4 cm (width) x 30.5 cm (height). Not to scale.

Figure 6: Experimental apparatus box set-up, with overhead, cross section, and moving wall coupling views. (a) Overhead view, (b) side view (looking east), and (c) moving wall couple. Note: orange heat mat array in (a), (b); scale on the side wall in (b); and U-shaped copper cooling manifold at the top of the box of (c).

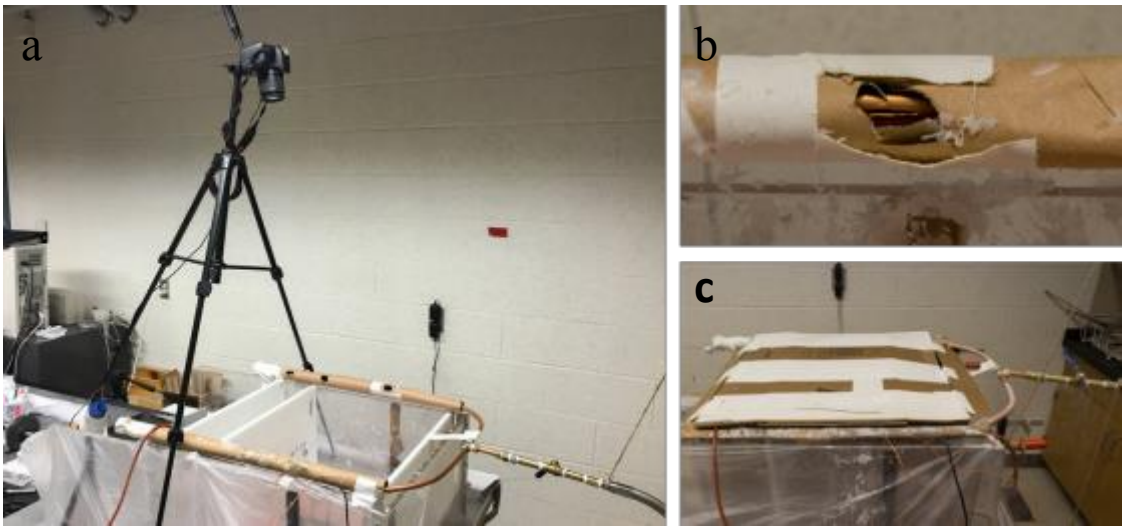

Figure 7: Camera set-up and cooling system of the experimental box set-up. (a) Camera position and U-shaped copper manifold with card-board tubes, (b) close up of copper manifold cooling slit, and (c) experimental box with closed cardboard lid to insulate experiment.

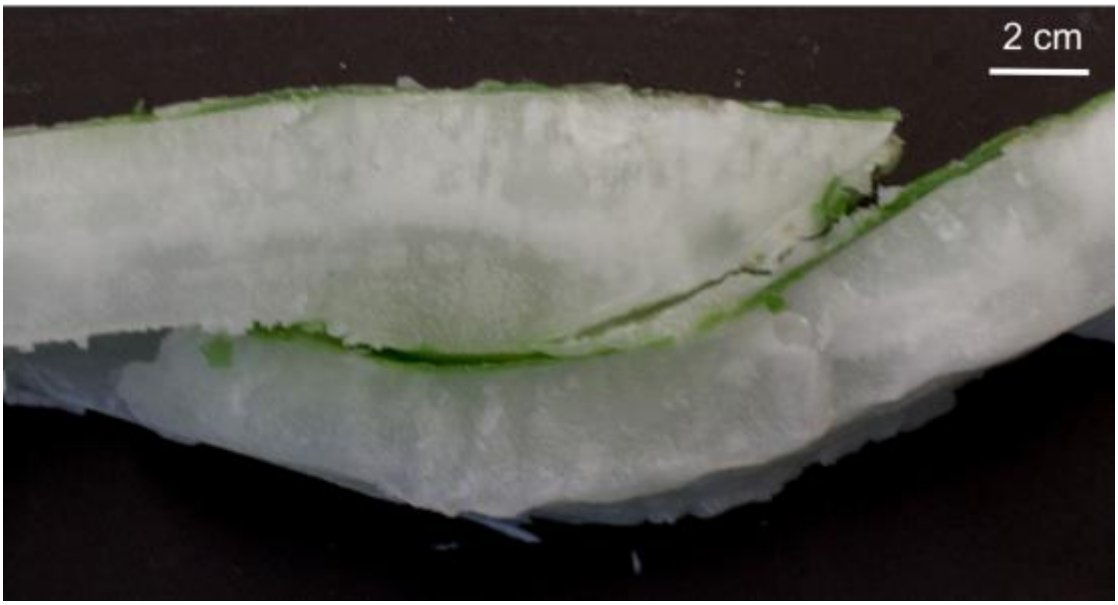

Figure 8: Example of a cross-section view (looking west) of a typical subsumption experiment. The thin green layer is colored wax painted onto the experimental wax surface before the onset of boundary displacement. Inclined PZW, 30 cm/hr. boundary displacement rate. Total boundary displacement was 13 cm.

Figure 9: Example of a cross-section view (looking west) of ductile roll back experiment. The thin green layer is colored wax that was painted onto the experimental wax surface before the onset of boundary displacement and traces the path of ductile roll back. Wax between both plates upwelled during PZW cut. Vertical PZW, 1 cm conductive layer thickness, 30 cm/hr. displacement rate. Total boundary displacement for this experiment was 13 cm.

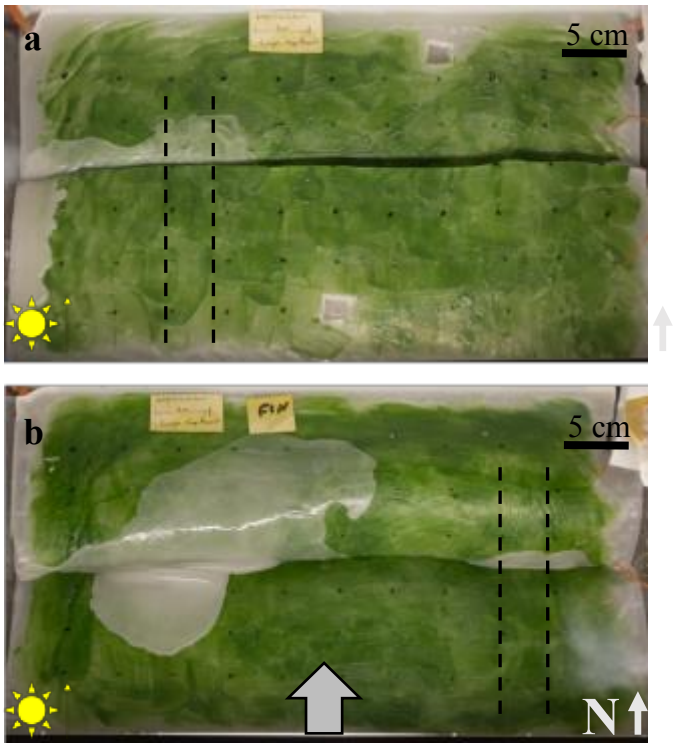

Figure 10: Overhead view of a comparison of the topography which develops from ductile roll back and subduction. (a) Subduction zone, (b) ductile roll back (b). Sun icon indicates lighting direction, thick grey arrow indicates displacement direction, and "N" indicates north direction in experiment. Dotted lines in (a**)** indicate cross section cut for Fig. 7, dotted lines in (b) indicate cross section cut for Fig. 8.

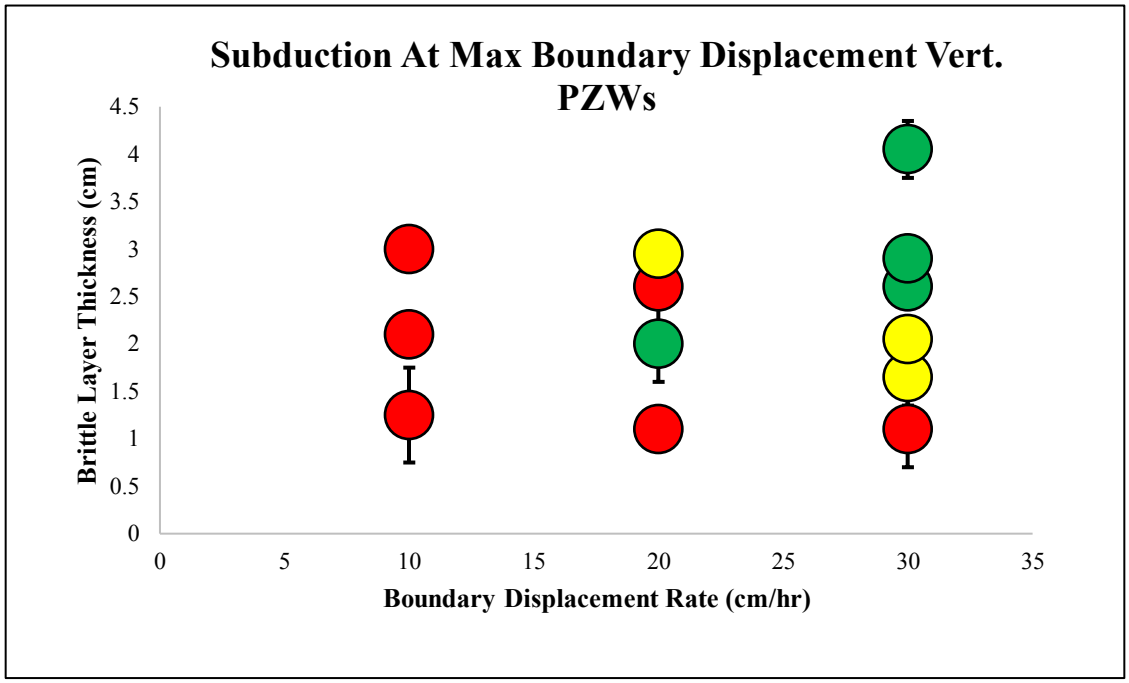

Figure 11: Scatter Plot of subduction initiation at maximum boundary displacement for vertical PZWs. The maximum boundary displacement varies by experiment. Vertical PZWs. Red dots indicate no subduction. Yellow dots indicate partial subduction, Green dots indicate subduction.

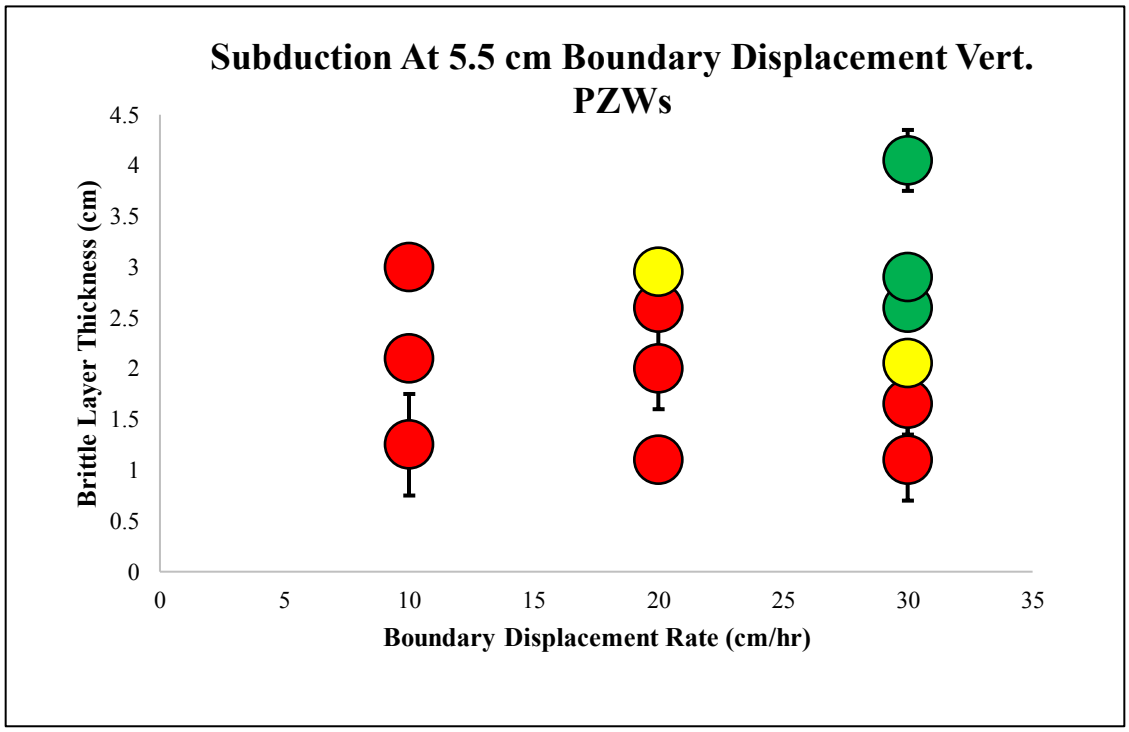

Figure 12: Scatter Plot of subduction initiation at 5.5 cm boundary displacement for vertical PZWs. Red dots indicate no subduction. Yellow dots indicate partial subduction, Green dots indicate subduction.

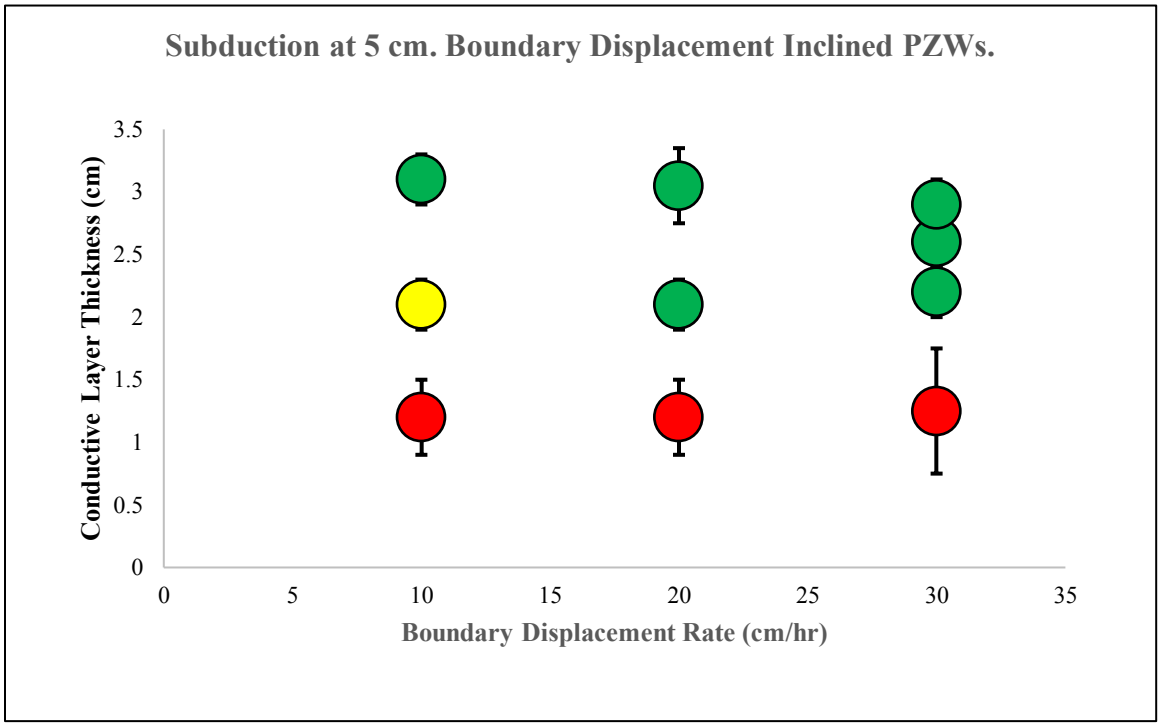

Figure 13: Scatter Plot of subduction initiation at 5 cm boundary displacement for inclined PZWs. Red dots indicate no subduction. Yellow dots indicate partial subduction, Green dots indicate subduction.

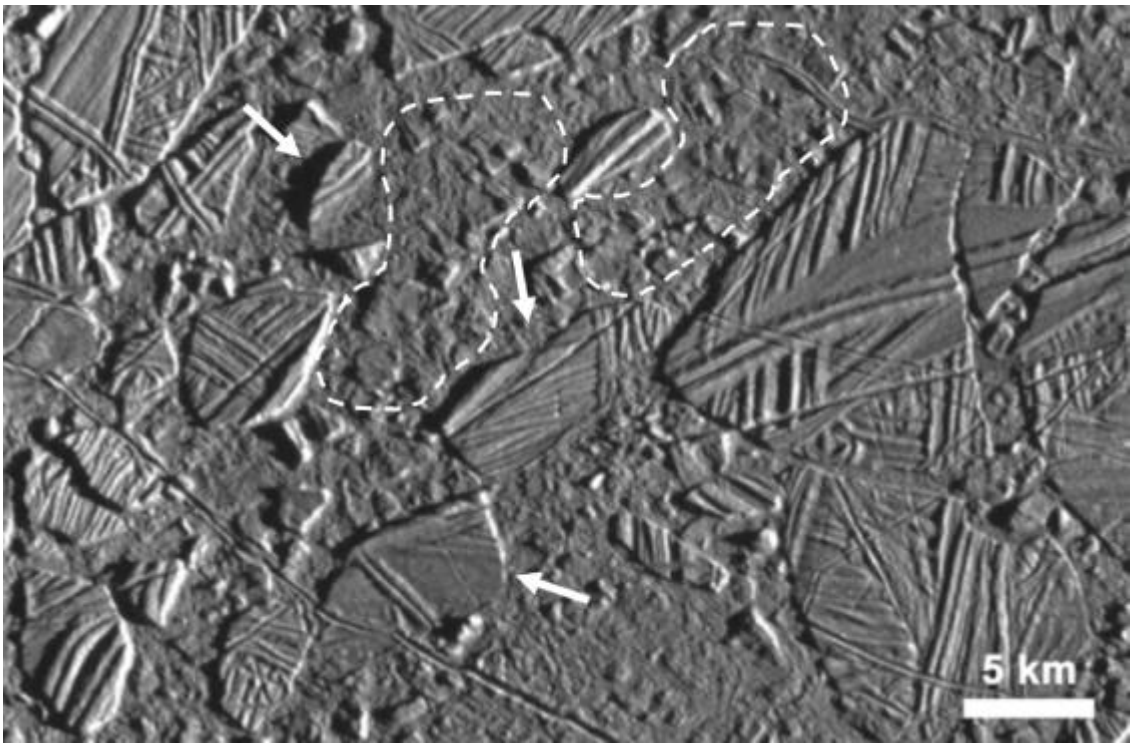

Figure 14: Center of Conamara Chaos region on Europa. White arrows indicate tilted blocks, white dotted lines highlight matrix with possible overturned blocks. Galileo E6ESBRTPLN01 observation, illumination from the right. Modified from Collins and Nimmo (2009).

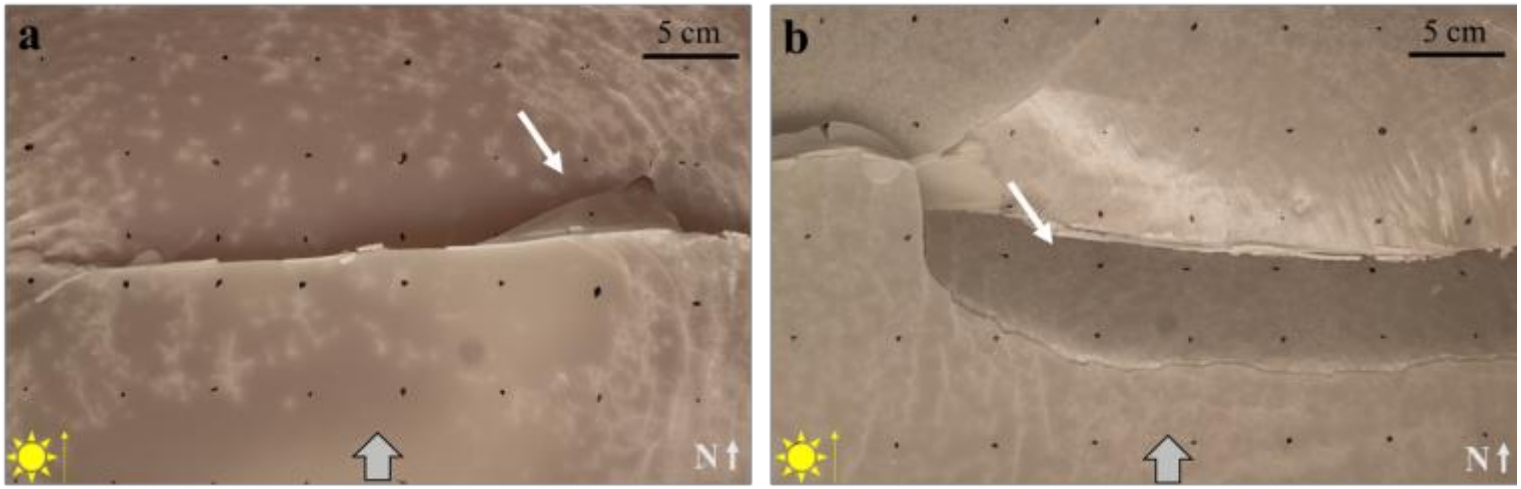

Figure 15: Comparison of small scale overturning vs. large scale over-turning in experiments accompanying subduction. A) 2.5 cm at 30 cm/hr. vertical PZW experiment. B) 4 cm at 30 cm/hr. vertical PZW experiment. White arrows indicate overturning blocks. 2 cm boundary displacement in (a), 4 cm boundary displacement in (b). Lighting directions and other symbols as in Fig. 14.

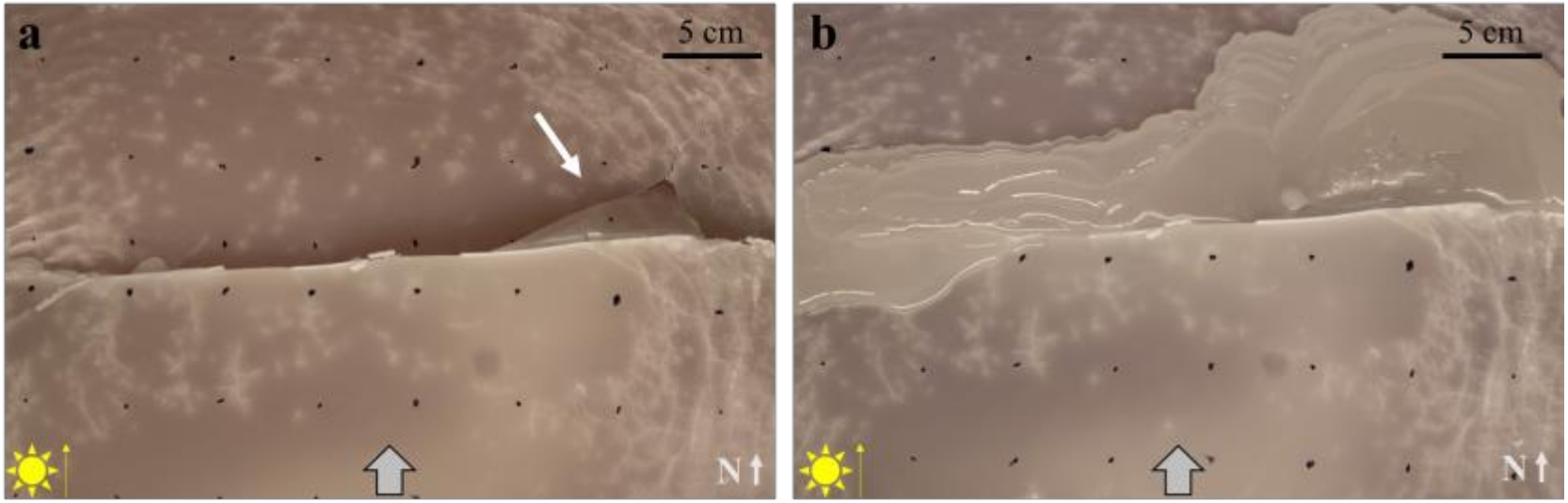

Figure 16: Close up of 2.5 cm at 30 cm/hr. vertical PZW experiment during subduction process. a) Subduction at 2 cm boundary displacement in which triangular block is overturning; b) Subduction at 4 cm boundary displacement after upwelling of subsurface molten wax creates a hummocky structure. White arrow in a) indicates small triangular block. Sun icon indicates lighting direction, grey arrow indicates displacement direction, "N" with arrow indicates north.

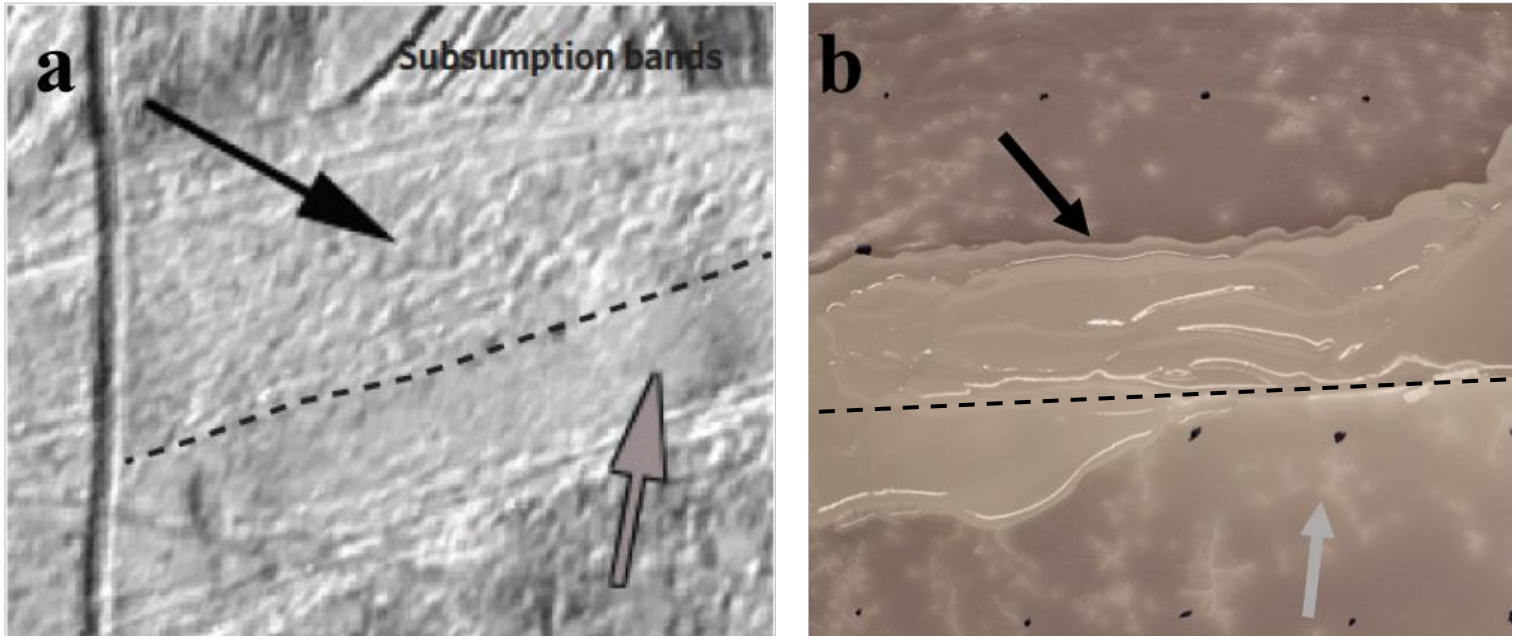

Figure 17: Comparison of hummocky structures observed on Europa and in experiment. a) Observed subsumption bands on Europa, with hummocky texture (black arrow). (b) Experimental subsumption band (2.5 cm at 30 cm/hr.) with hummocky texture (black arrow). Grey arrows indicate smooth surface in both images. Black dotted lines indicate sharp boundary between hummocky and smooth surfaces. In (b), black dotted line also indicates subsumption thrust fault. In (a) and (b) the plate at bottom of the image override the plate at the top of the image. (a) From Kattenhorn and Prockter (2014).

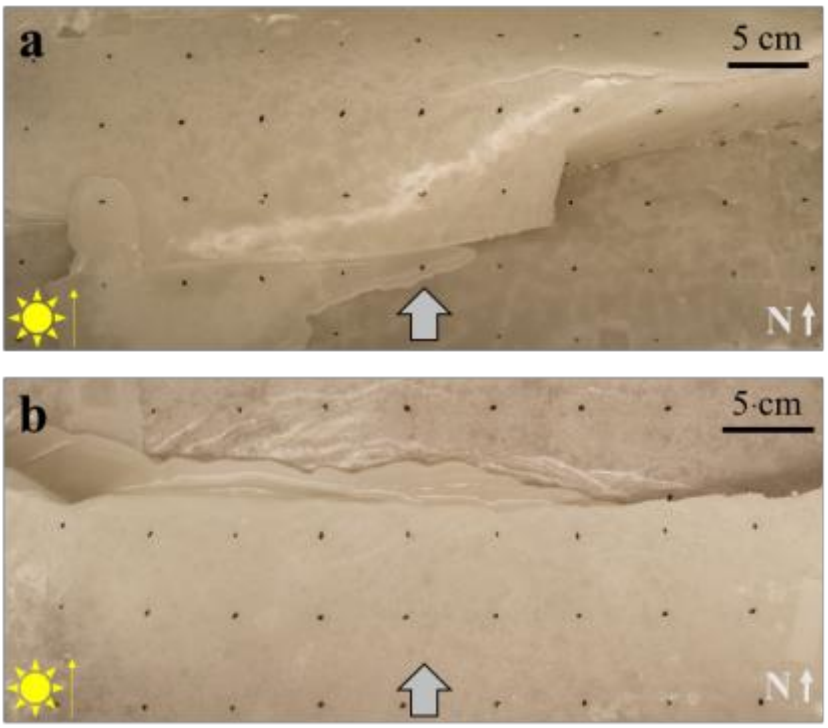

Figure 18: Comparison between vertical and inclined PZW experiments, and the resultant topography after 13 cm of boundary displacement. A) 3 cm at 30 cm/hr. vertical PZW experiment. B) and 3 cm at 30 cm/hr. inclined PZW experiment. Note relatively low topography across the PZW in b, compared to a. Lighting directions and other symbols as in Fig. 14.

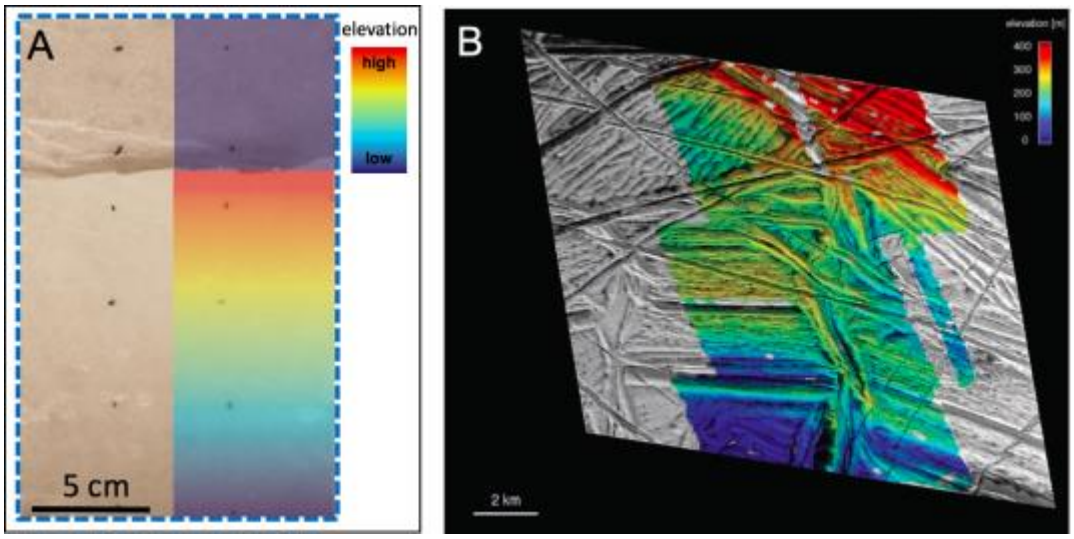

Figure 19: Comparison between inferred experimental regional topography and regional topography observed on Europa. A) overriding plate slightly increasing in elevation towards the subduction zone, while the overridden plate is slightly pushed down by the overriding plate. B) Observed regional topography on Europa, that could indicate an overriding plate, past or present. B modified from Prockter et al., 2002.

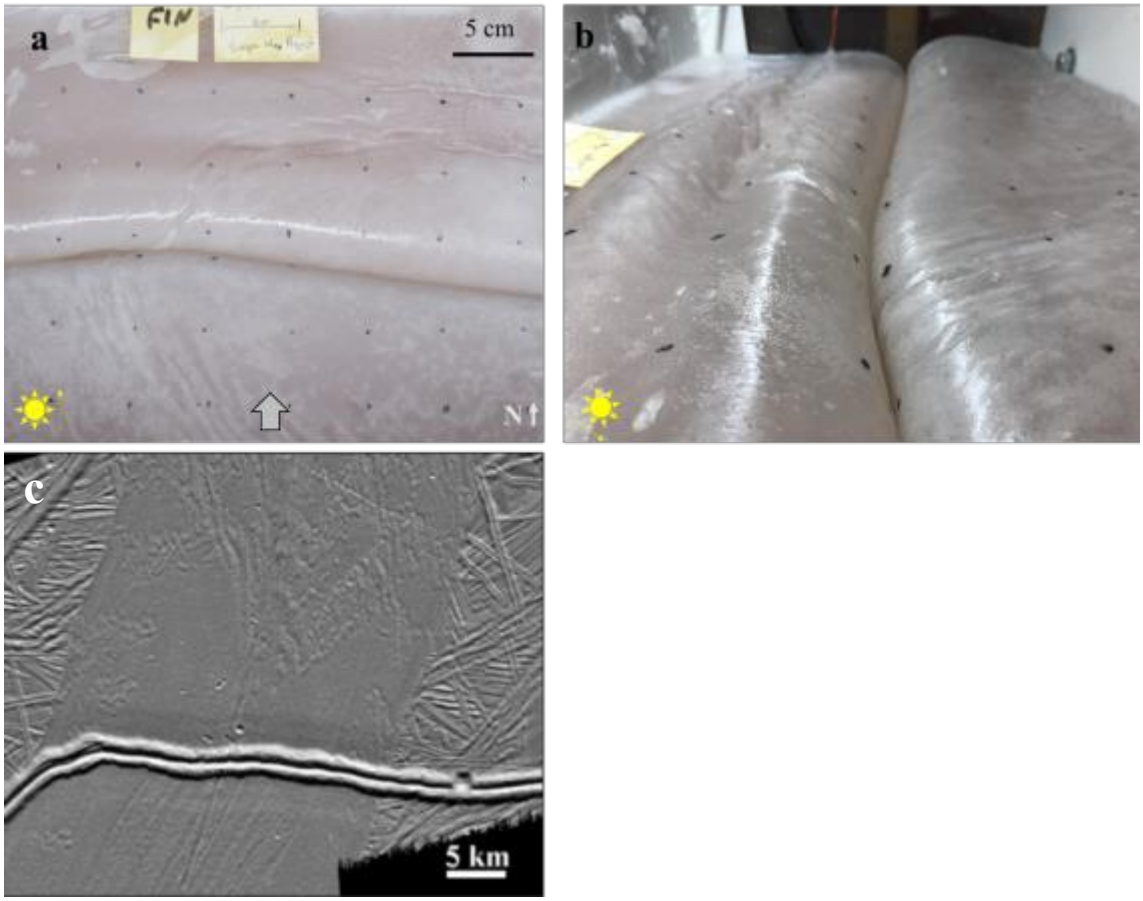

Figure 20: Comparison of double ridge structures from experiment (1 cm at 30 cm/hr.) and double ridges on Europa. (a) Map view of experimental ductile roll back and double ridges. (b) Side view of experimental ductile roll back and ridges. (c) Map view of double ridge observed on Europa. Symbols in a and b as in Fig. 14. (c) modified from Prockter et al. (2002).

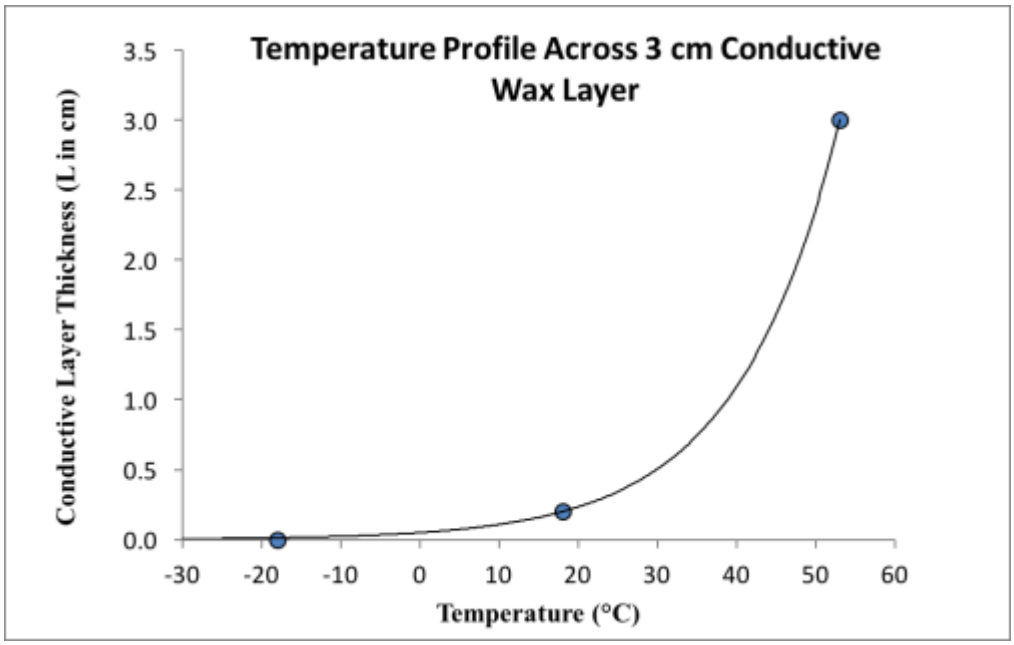

Figure 21: Exponential temperature profile across a 3 cm thick conductive layer, based on the measured surface temperature, subsurface temperature, and the melting temperature of wax.

Appendix A: Individual Experiment Result Descriptions and Figures

Vertical PZW Experiments

1 cm thickness at 10 cm/hr. deformation rate. In this experiment, pictures are taken every 3 minutes; each picture represents 0.5 cm of boundary displacement. The total boundary displacement is 9.5 cm of shortening.

This experiment does not result in subduction (Fig. A). Some of the displacement is accommodated by two wide anticline buckle folds (Fig. Ab-f) whose hinge lines are perpendicular to sub-perpendicular to the boundary displacement direction. The northern fold's southern limb and the southern fold's northern limb originate at the PZW, which serves as a hinge point between them (Fig. Ab). The PZW itself is driven into the subsurface with increasing boundary displacement (Fig. Ab-f). With increasing boundary displacement, additional surface material is pushed into the subsurface via ductile roll back at the PZW. Approximately 7.3 cm of surface material is driven into the subsurface by this process, with the remaining 2.2 cm of boundary displacement being accommodated mainly by the fold north of the PZW, which is larger and results in higher relief than the southern fold.

1 cm thickness at 20 cm/hr. deformation rate. In this experiment, pictures are taken every 2.5 minutes, each representing 0.83 cm of boundary displacement. Total boundary displacement is 10 cm of shortening.

This experiment does not result in subduction (Fig. B). The northern plate is dominated by a large anticline buckle fold near the northern edge (within 2.5 cm), which begins forming with the onset of boundary displacement (Fig. Bb,c). In the center, the

fold axis strike is perpendicular to the boundary displacement direction but the strike trends toward the PZW near the eastern and western edges of the experiment, eventually becoming subparallel to the boundary displacement direction (Fig Bf). Another anticline fold forms immediately above the PZW in the western half of the experiment; its strike is also perpendicular to the boundary displacement direction. On the southern plate, starting approximately 5 cm west of the eastern edge, a broader anticline fold with a strike perpendicular to the boundary displacement forms by 2.5 cm of boundary displacement (Fig Bc,d) and propagates westward with increasing boundary displacement to a maximum of 35 cm west of the eastern edge. By 6.6 cm of boundary displacement, this southern fold begins to pull the wax off the eastern edge of the experiment (Fig. Bf).

1 cm thickness at 30 cm/hr. deformation rate. In this experiment, pictures are taken every minute, each representing 0.5 cm of boundary displacement. Total boundary displacement is 13 cm of shortening.

This experiment does not result in subduction (Fig. C). At the onset of boundary displacement, two anticline buckle folds develop north and south of the PZW (Fig. Cb). The PZW serves as a hinge point between the northern fold's southern limb and the southern fold's northern limb. With increasing boundary displacement, the PZW is pushed into the subsurface (Fig. Cb-f). On the west side of the experiment, the PZW zone does not act as a hinge point between the northern and southern folds (Fig. Cc-f). Instead, north of the southern fold on this western side a triangular wedge between the fold and the PZW forms and the fold overturns onto it with increasing boundary displacement (Fig. C.c-f). A total of approximately 9.7 cm of surface material is pushed into the

subsurface via ductile roll back at the PZW (Fig. Cb-f). Near the end of the experimental run, molten wax upwells at the PZW between the two folds (Fig. Cf).

1.5 cm thickness at 30 cm/hr. deformation rate. In this experiment, pictures are taken every 2 minutes, each representing 1.0 cm of boundary displacement. Total boundary displacement is 13 cm of shortening.

This experiment results in partial subduction (Fig. D.). On the western edge of the experiment, partial subduction begins to develop by 2 cm of boundary displacement at the PZW with the plate south of the PZW overriding the plate north of the PZW (Fig. Dc). By 6 cm of boundary displacement, a strike-slip offset forms on the eastern edge of this partial zone (Fig. Dd). East of the strike slip offset, another subduction develops by 6 cm of boundary displacement that is approximately 10 cm wide, with opposite subduction orientation: the plate north of the PZW overrides the plate south of the PZW east of this transform fault (Fig. Dd). As boundary displacement increases, both adjacent zones, as well as the transform between them, subsuming approximately 9.5-10 cm of shortening (Fig. Dd-f). On the eastern edge of the experiment, a smaller partial subduction zone develops by 6 cm of boundary displacement (Fig. Dd). This side does not accommodate as much shortening and begins to rotate counter clockwise with increasing boundary displacement, eventually separating the wax from the eastern boundary plexiglass wall (Fig. Df). In contrast, the center of the experiment does not exhibit subduction (Fig. D). Here, the PZW becomes a hinge point for a syncline fold south of it. The fold's axial plan is perpendicular to the deformation direction and the fold itself is bounded by the two partial subduction zones on either side of it. This fold's

southern limb is near vertical by the end of the experimental run (Fig. Df). The area north of the PZW between the two subduction zones tilts up, dipping north, with increasing boundary displacement (Fig De,f).

2 cm thickness at 10 cm/hr. deformation rate. In this experiment, pictures are taken every 3 minutes, each representing 0.5 cm of boundary displacement. Total boundary displacement is 6 cm of shortening.

This experiment does not result in subduction (Fig. E). Upon the onset of boundary displacement, a single chevron buckle fold with the PZW as its hinge axis develops (Fig. Eb). The hinge of this fold rises with increasing boundary displacement (Fig. Eb-e). With increasing boundary displacement, north of the chevron buckle fold, a syncline fold co-develops with the PZW chevron fold. South of the PZW, a smaller syncline fold also co-develops with the chevron fold though it accommodates much less boundary displacement. Nearly all boundary displacement is accommodated by the PZW chevron fold and the syncline fold to the north of it.

2 cm thickness at 20 cm/hr. deformation rate. In this experiment, pictures are taken every 2.5 minutes, each representing 0.83 cm of boundary displacement. Total boundary displacement is 13.28 cm of shortening.

This experiment results in subduction only after extreme folding (Fig. F). North of the PZW, an anticline buckle fold with an axial plane perpendicular to the boundary displacement direction forms at the onset of boundary displacement, while the plate south of the PZW tilts and dips north towards the PZW (Fig. Fb). With increasing boundary

deformation, the fold limb dip increases (Fig. Fb-d). At 7.5 cm boundary displacement, deformation ceases on the northern buckle fold and subduction begins in the center (Fig. Fd). By 10 cm boundary displacement, subduction propagates to both edges (Fig. Fe). Approximately 2.9 cm of surface material is subsumed at the model center, with the plate north of the PZW overriding the plate south of the PZW (Fig. Fd-f). The southern fold limb is overturned at the eastern and western most edges of the experiment near the end of boundary displacement (Fig. Ff).

2 cm thickness at 30 cm/hr. deformation rate. In this experiment, pictures are taken every 2 minutes, each representing 0.5 cm of boundary displacement. Total boundary displacement is 13 cm of shortening.

This experiment results in subduction (Fig. G). Subduction begins at 2 cm of boundary displacement at the eastern side of the PZW with the northern plate overriding the southern plate (Fig. Gb). By 8 cm of boundary displacement, subduction propagates to the center of the experimental surface (Fig. Gd) and by 10 cm it propagates all the way to the western edge of the model (Fig. Ge). The total surface material subsumed decreases from east to west of the PZW with >5.8 cm at the eastern edge to 5.4 cm in the center to 0.9 cm at the western area, respectively (Fig. Gb-f). On both sides of the PZW, in the western half of the experiment, two folds with axial planes perpendicular to sub-perpendicular to the displacement direction develop with increasing boundary displacement (Fig. Gb-f). Both folds fracture at their hinge lines with the southern fold starting to fracture by 2 cm of boundary displacement (Fig. Gb) and the northern fold

starting to fracture by 3 cm, resulting in chevron folds (Fig. Gc). In the western half of the experiment these two folds accommodate most of the boundary deformation.

2.5 cm thickness at 20 cm/hr. deformation rate. In this experiment, pictures are taken every 2.5 minutes, each representing 0.83 cm of boundary displacement. Total boundary displacement is 10.8 cm of shortening.

This experiment does not result in subduction (Fig. H). In the center of the experiment a 25 cm wide anticline chevron buckle fold forms at the onset of boundary displacement with the PZW as the hinge axis (Fig. Hb-c). The hinge of this fold gains elevation with increasing boundary displacement and the dips of each limb approach 45° by 10.8 cm of boundary displacement (Fig. Hf). Immediately east of this fold, a syncline/anticline chevron buckle fold pair begins forming at the onset of boundary displacement (Fig Hb). For the southern syncline fold the PZW serves as the hinge axis. The hinge axis of this fold plunges vertically down with increasing boundary displacement and the dips of its limbs also approach 45° by 10.8 cm of boundary displacement (Fig. Hf). For the northern anticline chevron buckle fold on the eastern side, the hinge axis is approximately 8 cm north of the PZW. On the northern plate, approximately 10 cm south of the northern edge, a 35 cm wide syncline buckle fold begins forming at the onset of boundary displacement (Fig. Hb). The southern limb of this fold is the northern limb of the PZW chevron fold. The two fold limbs of this northern-most fold nearly join by maximum boundary displacement, almost pushing the entire fold into the subsurface (Fig. Hf).

2.5 cm thickness at 30 cm/hr. deformation rate. In this experiment, pictures are taken every 2 minutes, each representing 0.5 cm of boundary displacement. Total boundary displacement is 13 cm of shortening.

This experiment results in subduction (Fig. I). Subduction begins upon the onset of boundary displacement at the PZW with the southern plate overriding the northern plate (Fig. Ib). At 3 cm of boundary displacement a small triangular micro-block immediately north of the PZW begins to overturn (Fig. Ib-c), approximately 5 cm east of surface center. The northern point of this overturning micro-block punctures the surface and allows subsurface molten wax to be extrude onto the eastern surface at 4 cm of boundary displacement (Fig. Id). With increasing boundary displacement, additional subsurface molten wax is extruded covering the entire length of the surface around the PZW (Fig. Id-e). No further wax is extruded after 6 cm of boundary displacement. During the extrusion, the new wax cools and solidifies and is subsequently deformed by the increasing boundary displacement. Visible buckle folds form, which have axes that generally trend perpendicular to the boundary displacement direction (Fig. Ie,f). Total surface material subsumed at the PZW is 7.8 cm, 12 cm, and 8.3 cm for the western, central, and eastern areas. Approximately 2.5 cm from the eastern most edge at the PZW a transform fold develops by 3 cm of boundary displacement, though it is obscured by extruded subsurface wax by 5 cm of boundary displacement (Fig. Ic,d). West of this small transform fold, the plate south of the PZW overrides the northern plate, while east of the transform fold the northern plate overrides the southern plate.

3 cm solid layer at 10 cm/hr. deformation rate. In this experiment, pictures are taken every 3 minutes, each representing 0.5 cm of boundary displacement. Total boundary displacement is 6 cm of shortening.

This experiment does not result in subduction (Fig. J). At the onset of boundary displacement, north and south of the PZW, two experiment wide buckle folds develop (Fig. Jb). Each buckle fold has an axis perpendicular to the displacement direction and are approximately 15 cm north and south of the PZW, respectively. These two folds meet at the PZW, which serves as a hinge point for the southern limb of the northern fold and the northern limb of the southern fold. With increasing boundary displacement these folds drive the PZW ~3 - 3.5 cm vertically down towards the bottom of the experiment (Fig. Jb-f). At 3 - 4 cm of boundary displacement, both the northern and southern folds begin fracturing roughly along their hinge axes (Fig. Jd,e). These fractures widen with increasing boundary displacement to the end of the experimental run. All boundary displacement is accommodated by these two buckle folds.

3 cm solid layer at 20 cm/hr. deformation rate. In this experiment, pictures are taken every 3 minutes, each representing 1 cm of boundary displacement. Total boundary displacement is 11 cm of shortening.

This experiment results in partial subduction (Fig. K). Subduction begins at 3 cm of boundary displacement at the PZW and is limited to the western 20 cm of the experiment with the northern plate overriding the southern plate (Fig. Kc). At the onset, subduction is limited to a 7.5cm wide zone (Fig. Kc) but propagates east with increasing boundary displacement (Fig. Kc-f). The total surface material subsumed decreases from

west to east, with 7.6 cm of surface material being subsumed 5 cm east of the experiment edge, 6.6 cm subsumed 10 cm east of the western edge, 4.6 cm subsumed 15 cm east of the western edge, and 1 cm being subsumed 20 cm east of the western edge. North of the PZW a chevron buckle fold begins to form at 2 cm of boundary displacement at the eastern edge and propagates westward with increasing boundary displacement (Fig. Kb-f). The axis of this fold starts to fracture by 4 cm of boundary displacement (Fig. Kc). The axis of this fold is perpendicular to the deformation direction, until approximately 37 cm west of the eastern edge where it begins to bend towards the PZW, terminating at the PZW approximately 6 cm from the western edge of the experiment (Fig. Kc-f). South of the PZW, the southern block tilts and dips north. The dip angle increases with increasing boundary displacement (Fig. Kb-f). Small surface fractures form on the southern block with increasing boundary displacement (Fig. Kb-f).

3 cm solid layer at 30 cm/hr. deformation rate. In this experiment, pictures are taken every 2 minutes, each representing 1 cm of boundary displacement. Total boundary displacement is 13 cm of shortening.

This experiment results in subduction (Fig. L). Subduction begins at the onset of boundary displacement at the PZW, 10 cm west of center, with the northern plate overriding the southern plate (Fig. Lb). With increasing boundary displacement subduction propagates in both directions, east and west. At 6 cm of boundary displacement subduction has reached the western edge of the experiment (Fig. Ld) and in addition, propagated eastward to approximately 15 cm from the eastern edge of the experiment (Fig. Ld). By 11 cm of boundary displacement subduction occurs across the

entire PZW (Fig. Lf). The total surface material subsumed is 6.6 cm, 11 cm, and 1.5 cm for the western, central, and eastern sections of the PZW, respectively. At the eastern edge most boundary displacement is accommodated by a large chevron buckle fold that starts to form at the onset of boundary displacement. Its hinge axis starts to fracture at 2 cm of boundary displacement (Fig. Lb). The southern limb of this fold terminates at the PZW and the fold itself propagates westward with increasing boundary displacement. The westward propagation stops roughly in the center of the experiment at 4 - 5 cm of boundary displacement (Fig. Lc,d). At the western edge of the experiment, two roughly triangular blocks begin to rotate into the subsurface at 3 cm of boundary displacement. These blocks meet at the PZW, which serves as their rotation axis (Fig. Lc) and are bounded by fractures on their northern or southern edges, respectively. At 6 cm of boundary displacement the southern triangular block is thrust beneath the northern triangular block. With increasing boundary displacement the northern triangular block is overturned and eventually subsumed (Fig. Ld-f). Upwelling of fresh subsurface wax at the PZW marks the onset of subduction at the western edge where the two small triangular blocks meet. The plate south of the PZW dips slightly north with the onset of subduction (Fig. Lb).

4 cm solid layer at 30 cm/hr. deformation rate. In this experiment, pictures are taken every 2 minutes, each representing 1 cm of boundary displacement. Total boundary displacement is 14 cm of shortening.

This experiment results in subduction (Fig. M). Subduction initiates upon the onset of boundary displacement at the PZW, approximately 15 cm west of center with the

southern plate overriding the northern plate in a 20 cm wide subduction zone (Fig. Mb). The northern plate dips slightly south toward the PZW at the onset of subduction (Fig. Mb). At 3 cm of boundary displacement the eastern edge of the western subduction zone is bounded by a transform fault (Fig. Mc). East of the transform fault, subduction orientation is reversed with the northern plate overriding the southern plate at the PZW (Fig. Mc). The western subduction zone retains its geometry/orientation throughout the experiment, while the eastern subduction zone does not. On the southern plate a fracture forms, which strikes east/west from the southern edge of the transform fault to the eastern edge of the experiment surface. This fracture becomes the southern boundary of a new plate that is composed of the subduction zone to the north of this fracture. The transform fault represents the western boundary and the eastern edge of the experiment represents the eastern boundary of this plate. Its dimensions are approximately 30 cm x 7 cm before subduction (Fig. Mb). At 10 cm of boundary displacement, this plate is almost completely subsumed. Its southern-most edge, restricted by the fracture, overturns and subduction orientation is reversed. Now the entire southern plate overrides the northern plate with continues boundary displacement (Fig. Me). The onset of subduction reversal on the eastern side of the transform fault is marked by the upwelling of molten wax onto the surface immediately above the subduction zone (Fig. Me). The total surface volume subsumed is 13.7 cm, 13 cm, and 13.5 cm for the western, central, and eastern sections of the PZW respectively.

Inclined PZW Experiments

1 cm solid layer at 10 cm/hr. deformation rate. In this experiment, pictures are taken every 3 minutes, each representing 0.5 cm of boundary displacement. Total boundary displacement is 7 cm of shortening. The inclined PZW in this experiment dips south.

This experiment does not result in subduction (Fig. N). Two buckle folds begin to develop with the onset of boundary displacement north and south of the PZW that stretch over the entire experimental width (Fig. Nb). Each fold axis is perpendicular to the boundary displacement direction and the northern and southern limbs of the southern and northern folds, respectively, meet at the PZW (Fig. Nc). The PZW acts as a leverage point for the two fold limbs. At 2.5 cm of boundary displacement ductile roll back begins to push the PZW into the subsurface (Fig. Nc). A total of approximately 3.2 cm of surface material is pushed into the subsurface at the PZW via this process (Fig. Nf). Thickness control was poor for this experiment and the solid layer thickness grew from 1.0 cm before the onset of boundary displacement to 1.3-1.75 cm after 7 cm of boundary displacement.

1 cm solid layer at 20 cm/hr. deformation rate. In this experiment, pictures are taken every 2.5 minutes, each representing 0.83 cm of boundary displacement. Total boundary displacement is 11.6 cm of shortening. The inclined PZW in this experiment dips south.

This experiment does not result in subduction (Fig. O). Two buckle folds develop with the onset of boundary displacement north and south of the PZW that stretch over the entire experimental width (Fig. Ob). Each fold axis is perpendicular to the boundary displacement direction. The northern and southern limbs of the southern and northern

folds, respectively, meet at the PZW (Fig. Oc), which acts as a leverage point for the two fold limbs. At 3.32 cm of boundary displacement ductile roll back begins to push the PZW into the subsurface (Fig. Oc). The total surface material pushed into the subsurface via this process is 9.9 cm, 7.9 cm, and 10 cm for the western, central, and eastern sections of the PZW. The small 15 cm x 3 cm patch of wax that upwelled during creation of the PZW (Fig. Oa) is completely beneath the subsurface at the end of the experiment (Fig. Of).

1 cm solid layer at 30 cm/hr. deformation rate. In this experiment, pictures are taken every 2 minutes, each representing 1 cm of boundary displacement. Total boundary displacement in this experiment is 13 cm of shortening. The inclined PZW in this experiment dips south. Wax upwelled during extraction of the southern thickness sample as well as during the PZW cut that now covers large parts of the surface (Fig. Pa).

This experiment does not result in subduction (Fig. P). At the onset of boundary displacement a large buckle fold develops on the plate north of the PZW (Fig. Pb,c). The northern plate buckle fold has an axis that is perpendicular to the displacement direction in the center of the experiment. However, it trends towards the PWZ in both directions: approximately 18 cm east of the western edge and ~ 13 cm west of the eastern edge (Fig. Pd). The PZW acts as a pivot point for the large northern buckle fold and a smaller southern buckle fold. At 2.5 cm of boundary displacement, the northern and southern limbs of the southern and northern folds, respectively, push the PZW into the subsurface via ductile roll back at the eastern 15 cm of the experiment (Fig. Pc). Ductile roll back propagates from east to west with increasing boundary displacement but stops

approximately 15 cm east of the western edge (Fig. Pe,f). The total amount of surface material that is pushed into the subsurface increases from west to east from 1 cm, to 5.3 cm, and to 10.5 cm for the western edge, center, and eastern sections of the ductile roll back zone, respectively. On the southern plate, a buckle fold with an axis parallel to the PZW exhibits less surface relief with increasing boundary displacement compared to the northern plate buckle fold (Fig. Pf). A small 5 - 6 cm subduction zone does develop at the onset of boundary displacement at the western edge of the experiment, with the southern plate overriding the northern plate (Fig. Pb). Subduction does not occur elsewhere in the experiment, nor does the western edge subduction zone propagate with increasing deformation. Thus, this experiment does not fulfill the subduction (partial or full) criteria.

2 cm solid layer at 10 cm/hr. deformation rate. In this experiment, pictures are taken every 3 minutes, each representing 0.5 cm of boundary displacement. Total boundary displacement is 5 cm of shortening. The inclined PZW created in this experiment dips north. The inclined PZW in this experiment dips south. Wax upwelled during the process of cutting of the PZW (Fig. Qa).

This experiment results in partial subduction (Fig. Q). Subduction initiates upon the onset of boundary displacement on the western 2/3 of the experiment with the northern plate overriding the southern plate (Fig. Qb). The subduction zone ends approximately 18 cm west of the eastern edge of the experiment (Fig. Qc). Atop and south of the PZW, a thin layer of younger wax, which upwelled during creation of the PZW, appears to resist subduction (Fig. Qc-f). With increasing boundary displacement this younger wax layer develops a series of short wavelength (≤ 2 cm) buckle folds with

axes perpendicular to the boundary displacement direction (Fig. Qc-f). East of the subduction zone, at the onset of boundary displacement, the formation of a chevron buckle fold accommodates the boundary displacement. The PZW serves as its hinge axis (Fig. Qb). With increasing boundary displacement this fold turns into a 10 cm x 6.5 cm block that rotates with an increasing northward dip and is nearly overturned at 4.5 cm of boundary displacement (Fig. Qf). As this block rotates, its southern boundary – the PZW –, is pushed upward with increasing boundary displacement (Fig. Qb-f). The total surface area subsumed in this experiment is nearly identical with ~ 4.2 cm across the subduction zone by the end of the experiment (Fig. Qf).

2 cm solid layer at 20 cm/hr. deformation rate. In this experiment, pictures are taken every 2.5 minutes, each representing 0.83 cm of boundary displacement. Total boundary displacement is 11.6 cm of shortening. The inclined PZW created in this experiment dips south. Wax upwelled during the cutting of the PZW.

This experiment results in subduction (Fig. R). Subduction initiates upon the onset of boundary displacement across the entire PZW with the southern plate overriding the northern plate (Fig. Rb). The thin layer of younger wax, which upwelled onto the northern plate during creation of the PZW, appears to resist subduction (Fig. Rb-f). Instead, this younger wax develops a series of short wavelength (≤ 2.5cm) buckle folds with axes roughly perpendicular to the boundary displacement direction (Fig. Rb-f). On the northern plate, approximately 4 cm from the northern boundary and 8 cm from the eastern boundary, a ~15 cm wide buckle fold develops at 1.6 cm of boundary displacement and accommodates the boundary displacement in the east that is not

accommodated by subduction (Fig. Rb). Within 5 cm of the subduction zone, the northern plate bends dipping south towards the subduction zone. The total surface material subsumed decreases slightly from west to east with 11.6 cm, 11.3 cm, and 11 cm total subduction for the western, center, and eastern sections of the PZW, respectively (Fig. Rf).

2 cm solid layer at 30 cm/hr. deformation rate. In this experiment, pictures are taken every 2 minutes, each representing 1 cm of boundary displacement. Total boundary displacement is 13 cm of shortening. The inclined PZW created in this experiment dips south. Wax upwelled during the cutting of the PZW (Fig. Sa).

This experiment results in subduction (Fig. S). Subduction begins at 1 cm of boundary displacement at the western side of the experiment, approximately 8.5 cm east of the western edge with the southern plate overriding the northern plate (Fig. Sb). At the eastern side of the experiment subduction begins at 6 cm of boundary displacement (Fig. Sd) and in the center of the experiment subduction begins at 8 cm of boundary displacement (Fig. Sd). In addition, subsurface wax is extrudes onto the surface in the center of the experiment, which marks the onset of subduction in this area at the PZW. At 10 cm of boundary displacement this fresh wax covers the entire length of the PZW (Fig. Se). The thin layer of surface wax present on the western side of the experiment from the beginning (Fig. Sa) develops short wavelength (≤ 2 cm) buckle folds with axes that strike north-east at the onset of displacement (Fig. Sb). These short buckle folds resist subduction until they are covered by fresher upwelling wax at 10 cm of boundary displacement (Fig. Se). In the north-eastern quarter of the experimental surface, a large

buckle fold with a wavelength of 10 cm starts to develop at 2 cm of boundary displacement. It begins rolling (rotation towards the PZW) into the subsurface at 8cm of boundary displacement (Fig. Sd). By the end of the experiment, at 13 cm of boundary displacement, almost half of this fold is below the surface of the younger upwelled wax (Fig. Sf). The total surface area subsumed in the west, center, and east at the PZW are 12.7 cm, 5.2 cm, and 12.7 cm, respectively.

2.5 cm solid layer at 30 cm/hr. deformation rate. In this experiment, pictures are taken every 2 minutes, each representing 1 cm of boundary displacement. Total boundary displacement is 11 cm of shortening. The inclined PZW created in this experiment dips north (Fig. Ta).

This experiment results in subduction (Fig. T). Subduction initiates upon onset of boundary displacement in the western 2/3 of the experiment surface, with the northern plate overriding the southern plate (Fig. Tb). The subduction zone itself is obscured by a thin layer of younger wax that upwelled during the creation of the PZW, which immediately detaches from the southern plate at the onset of subduction but remained attached to the northern plate (Fig. Tb-f). On the eastern 1/3 of the model, the PZW constraints two blocks that fracture away from the northern and southern plates at 4 cm of boundary displacement (Fig. Tc). The northern block is roughly rectangular while the southern block is roughly triangular (Fig. Tc). The edge of each block that make up either side of the PZW pushes the PZW into the subsurface with increasing boundary displacement (Fig. Tb-f). At 7 cm of boundary displacement the southern triangular block is rotated completely vertical; by 8 cm of boundary displacement it has overturned (Fig.

Te). By the end of the experiment, at 11 cm of boundary displacement, the northern rectangular block is rotated vertical (Fig. Tf). This eastern deformation does not result in a noticeable increase in surface topography, and at the end of the experimental run it accommodates 10 cm of boundary displacement by pushing the two blocks into the subsurface. The total surface area subsumed in the west, center, and east (10 cm east of center) of this experiment is nearly constant with 10 cm, 10 cm, and 8.75 cm, respectively.

3 cm solid layer at 10 cm/hr. deformation rate. In this experiment, pictures are taken every 3 minutes, each representing 0.5 cm of boundary displacement. Total boundary displacement is 7.5 cm of shortening. The inclined PZW created in this experiment dips south. Wax upwelled during the cutting of the PZW (Fig. Ua).

This experiment results in subduction (Fig. U). Subduction initiates upon onset of boundary displacement across the entire PZW with the southern plate overriding the northern plate (Fig. Ub). By 6.5 cm of boundary displacement, subsurface molten wax is extruded onto the experimental surface north of the PZW. Additional molten wax is extruded to the north of the PZW at 7 cm of boundary displacement (Fig. Uf). A near uniform amount of surface material is subsumed along the PZW, with values of 6.8 cm, 7 cm, and 7 cm for the western side, center, and eastern sections respectively. The southern plate exhibits no observable surface deformation, while the northern plate slightly dips south toward the subduction zone.

3 cm solid layer at 20 cm/hr. deformation rate. In this experiment, pictures are taken every 2.5 minutes, each representing 0.83 cm of boundary displacement. Total boundary displacement is 13.3 cm of shortening. The inclined PZW created in this experiment dips south.

This experiment results in subduction (Fig. V). Subduction begins upon onset of boundary displacement across the entire PZW with the southern plate overriding the northern plate (Fig. Vb). At 10.8 cm of boundary displacement, subsurface molten wax is extruded onto the experimental surface north of the PZW, in the center, and eastern edge of the experiment (Fig. Vf). During the creation of the PZW, a small layer of molten wax upwelled and extruded onto the western half of experimental surface north of the PZW (Fig. Va). From 0.83 cm to 1.6 cm of boundary displacement this thin, young wax layer inflates from additional molten subsurface wax that upwelled into this layer (Fig. Vb,c). With increasing boundary displacement, after 1.6 cm, this zone develops three small wavelength (≤ 2 cm) buckle folds (Fig. Vd-f). Within approximately 7 cm of the advancing subduction zone, the northern plate tilts, dipping south toward the subduction zone. The total amount of surface material subsumed at the PZW is 13cm and is uniform across the length of the subduction zone (Fig. Vb-f).

3 cm solid layer at 30 cm/hr. deformation rate. In this experiment, pictures are taken every 2 minutes, each representing 1 cm of boundary displacement. Total boundary displacement is 13 cm of shortening. The inclined PZW created in this experiment dips south.

This experiment results in subduction (Fig. W). Subduction begins upon onset of boundary displacement across almost the entire PZW with the southern plate overriding the northern plate (Fig. W). The only exception is a small zone from the western edge to 5 cm east of that edge in the experiment, which never subsumes (Fig. Wb-f). During creation of the PZW, before boundary displacement, a thin layer of molten wax upwelled and spread onto the northern plate in the central area (Fig. Wa). This younger wax does not impede subduction in this area (Fig. Wb-f). At 11 cm of boundary displacement, nearly this entire younger thin layer is subsumed (Fig. We). Between 11 cm and 12 cm of boundary displacement, new subsurface molten wax is extruded onto the northern western half of the experimental surface immediately north of the subduction zone (Fig.Wf). The total amount of surface material subsumed is nearly uniform across the length of the subduction zone with 12.3 cm, 12.4 cm, and 12.5 cm for the western, central, and eastern sections at the PZW, respectively.

Special Geometry Cut Experiments

2 cm solid layer deformed at 30 cm/hr., half PZW cut. In this experiment, pictures are taken every 2 minutes, each representing 1 cm of boundary displacement. Total boundary displacement is 9 cm.

This experiment does not result in subduction (Fig. X). Instead of cutting completely through the entire solid surface layer to create the PZW, a cut of only half the solid layer thickness (1 cm) is performed. The experiment surface is dominated by a model wide east/west trending buckle fold with the PZW serving as its hinge axis (Fig. Xb-f). The fold begins forming at the onset of boundary displacement and with increasing

boundary displacement its northern limb pushes down into the subsurface, reaching a dip of almost 60° (Fig. Xf). At the eastern edge of this fold, the northern limb is completely overturned at 9 cm of boundary displacement (Fig. Xf).

1 cm solid layer deformed at 10 cm/hr. vertical PZW

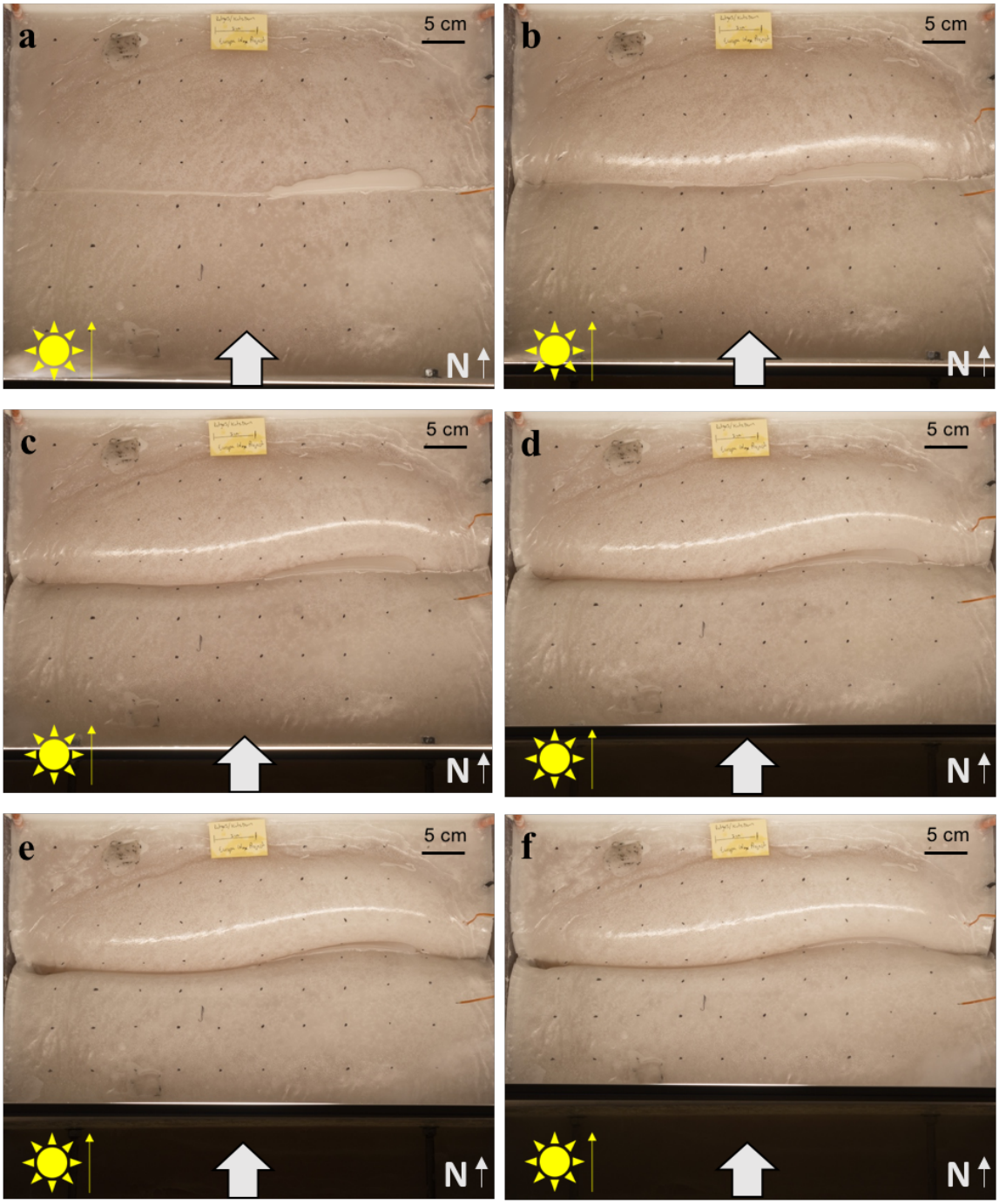

Figure A: Map view of 1 cm thick solid layer deformed at 10 cm/hr., vertical cut at a) initial conditions, b) 2 cm displacement, c) 4 cm displacement, d) 6 cm displacement, e) 8 cm displacement, and f) 9.5 cm displacement. Lighting from above in (a); sun icon indicates lighting direction in (b)-(f); thin gray arrow in conjunction the "N" indicate the northern direction of the set-up; thick, grey arrow indicates displacement direction.

1 cm solid layer deformed at 20 cm/hr. vertical PZW

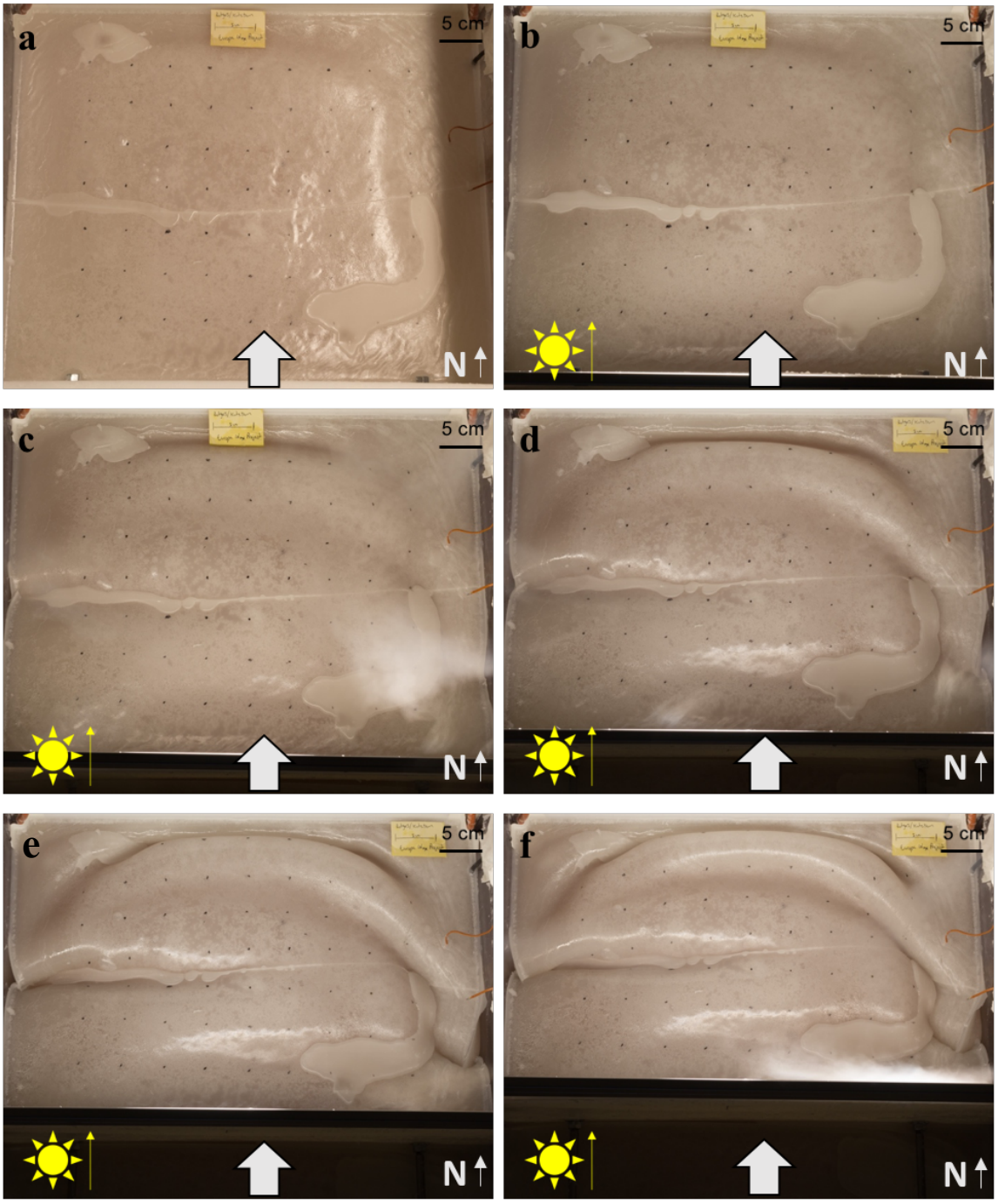

Figure B: Map view of 1 cm thick solid layer deformed at 20 cm/hr., vertical PZW at a) initial conditions, b) 0.83 cm displacement, c) 2.5 cm displacement, d) 5 cm displacement, e) 7.5 cm displacement, and f) 10 cm displacement. Lightning directions and symbols as in Fig. A.

1 cm solid layer deformed at 30 cm/hr. vertical PZW

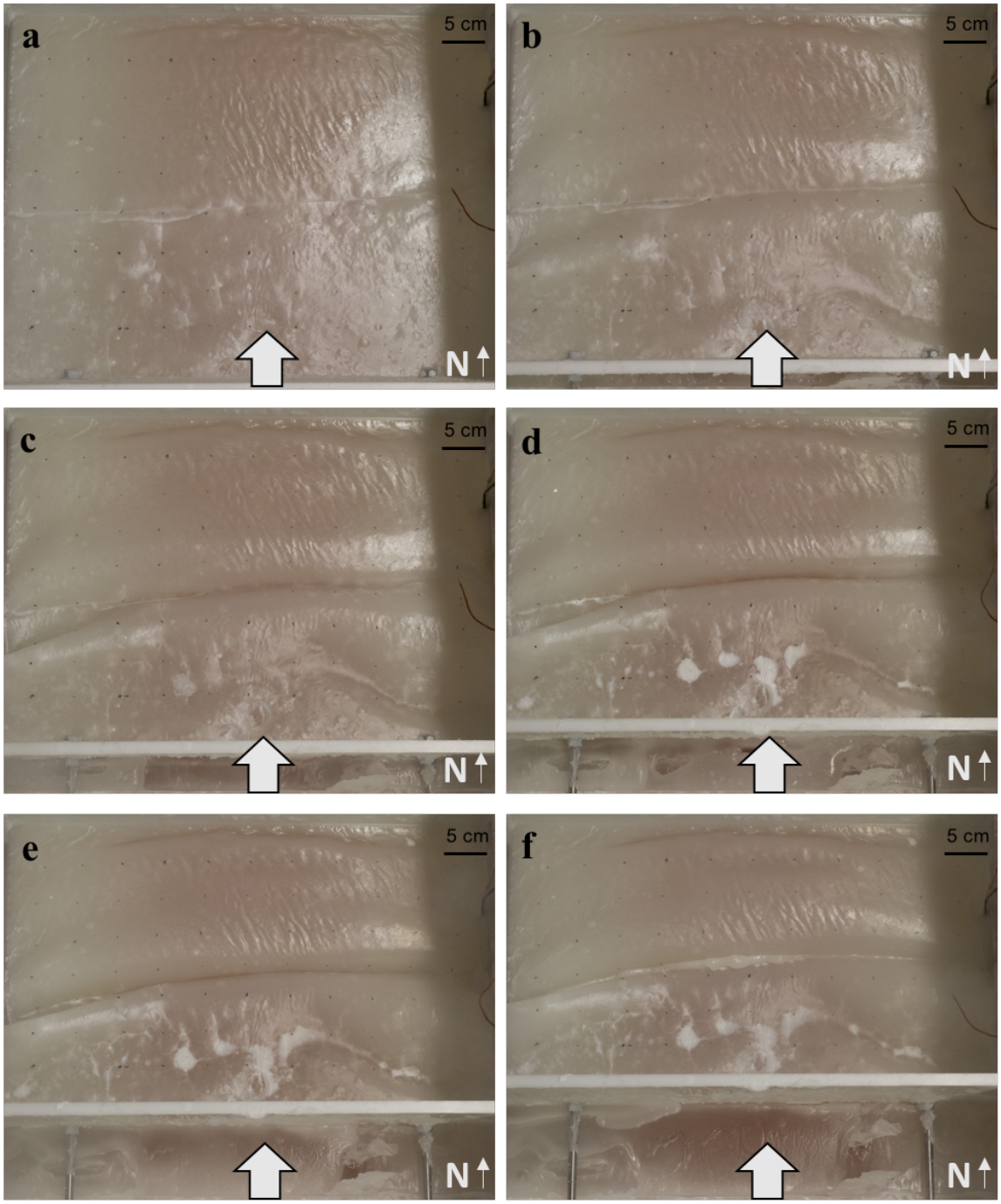

Figure C: Map view of 1 cm thick solid layer deformed at 30 cm/hr., vertical PZW at a) initial conditions, b) 2.5 cm displacement, c) 5 cm displacement, d) 7.5 cm displacement, e) 10 cm displacement, and f) 13 cm displacement. Lighting only from above and symbols as in Fig. A.

1.5 cm solid layer deformed at 30 cm/hr. vertical PZW

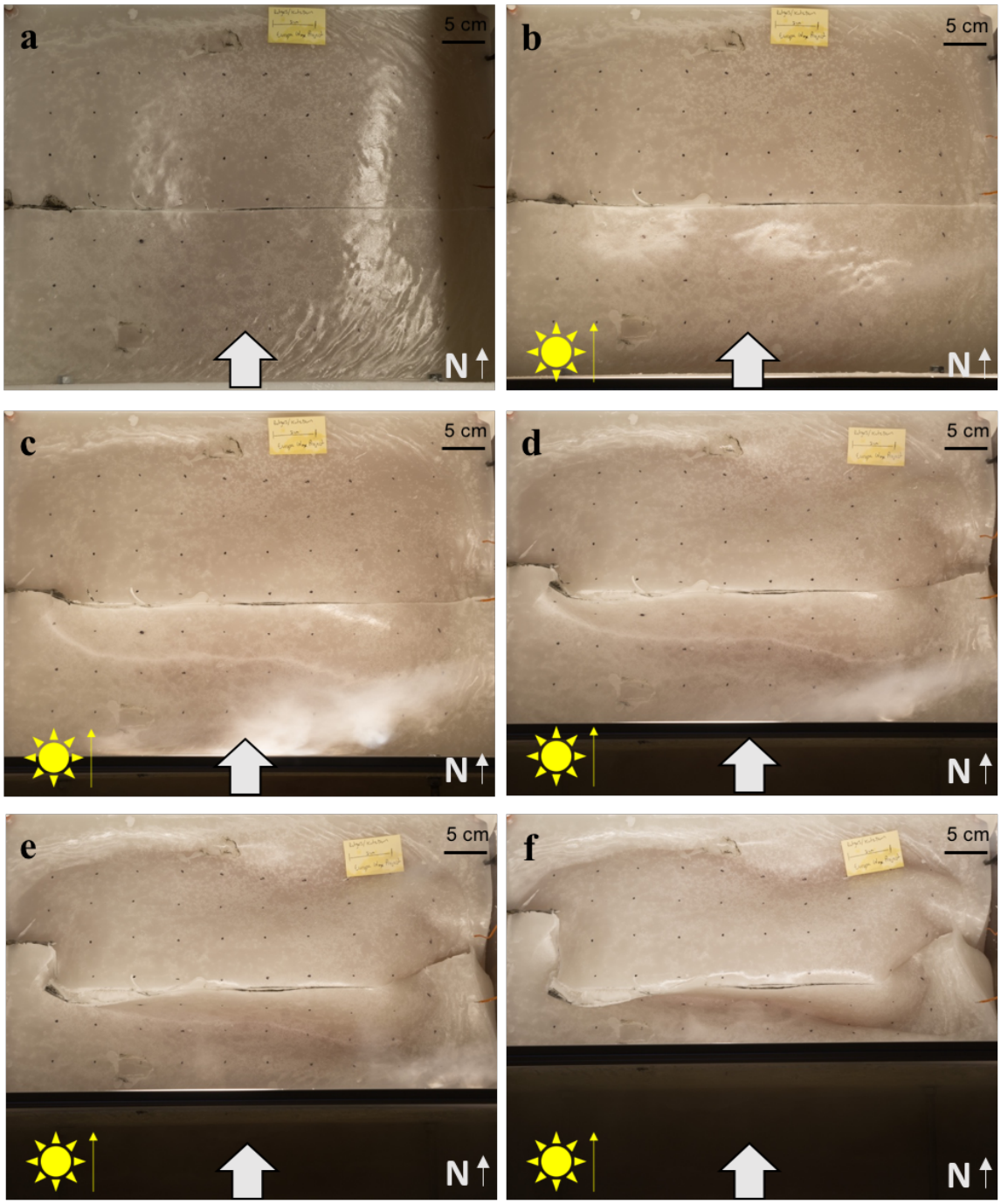

Figure D: Map view of 1.5 cm thick solid layer deformed at 30 cm/hr., vertical PZW at a) initial conditions, b) 1 cm displacement, c) 3 cm displacement, d) 6 cm displacement, e) 9 cm displacement, and f) 13 cm displacement. Lightning directions and symbols as in Fig. A.

2 cm solid layer deformed at 10 cm/hr. vertical PZW

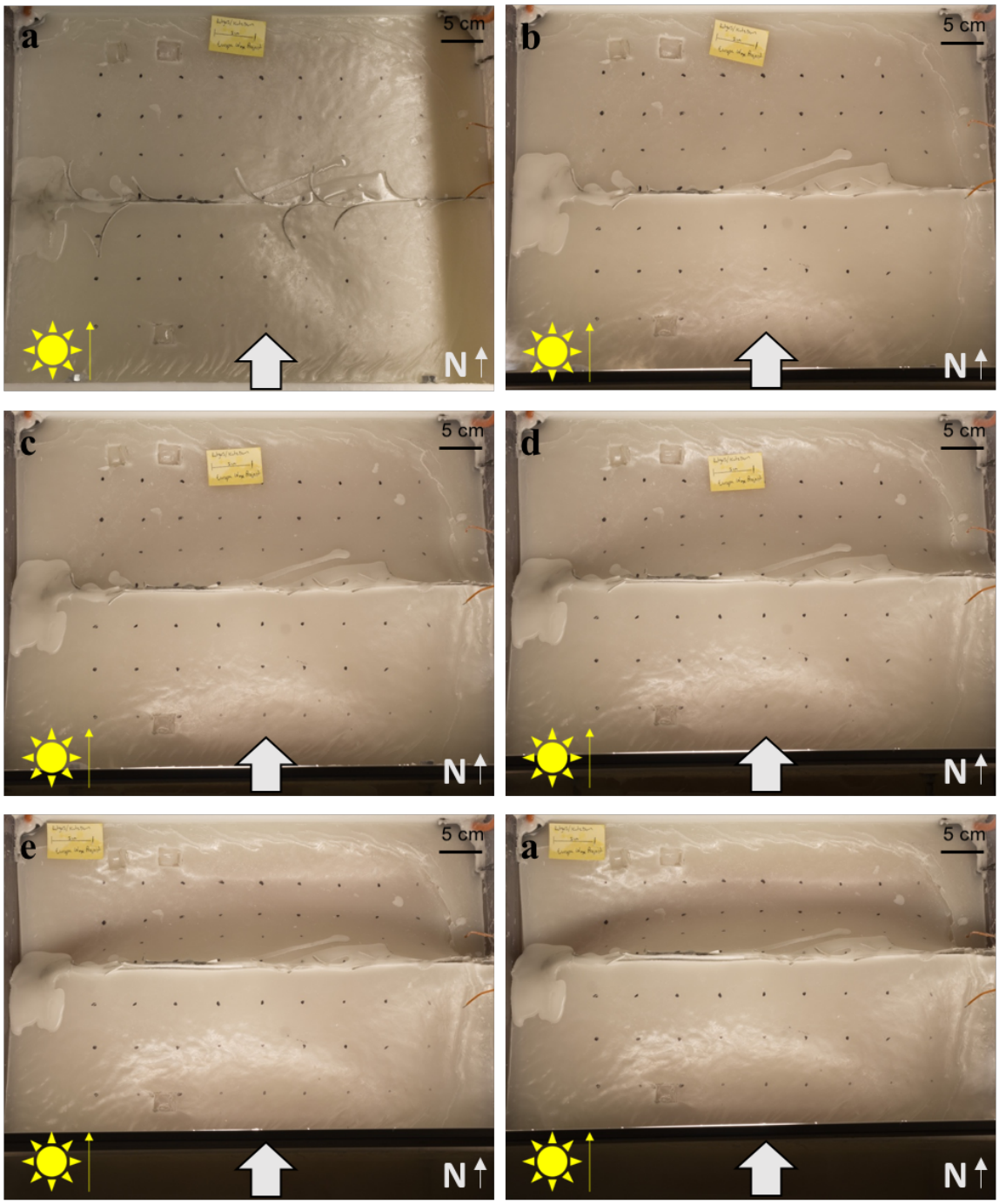

Figure E: Map view of 2 cm thick solid layer deformed at 30 cm/hr., vertical PZW at a) initial conditions, b) 1 cm displacement, c) 2 cm displacement, d) 3 cm displacement, e) 5 cm displacement, and f) 6 cm displacement. Lightning directions and symbols as in Fig. A.

2 cm solid layer deformed at 20 cm/hr. vertical PZW

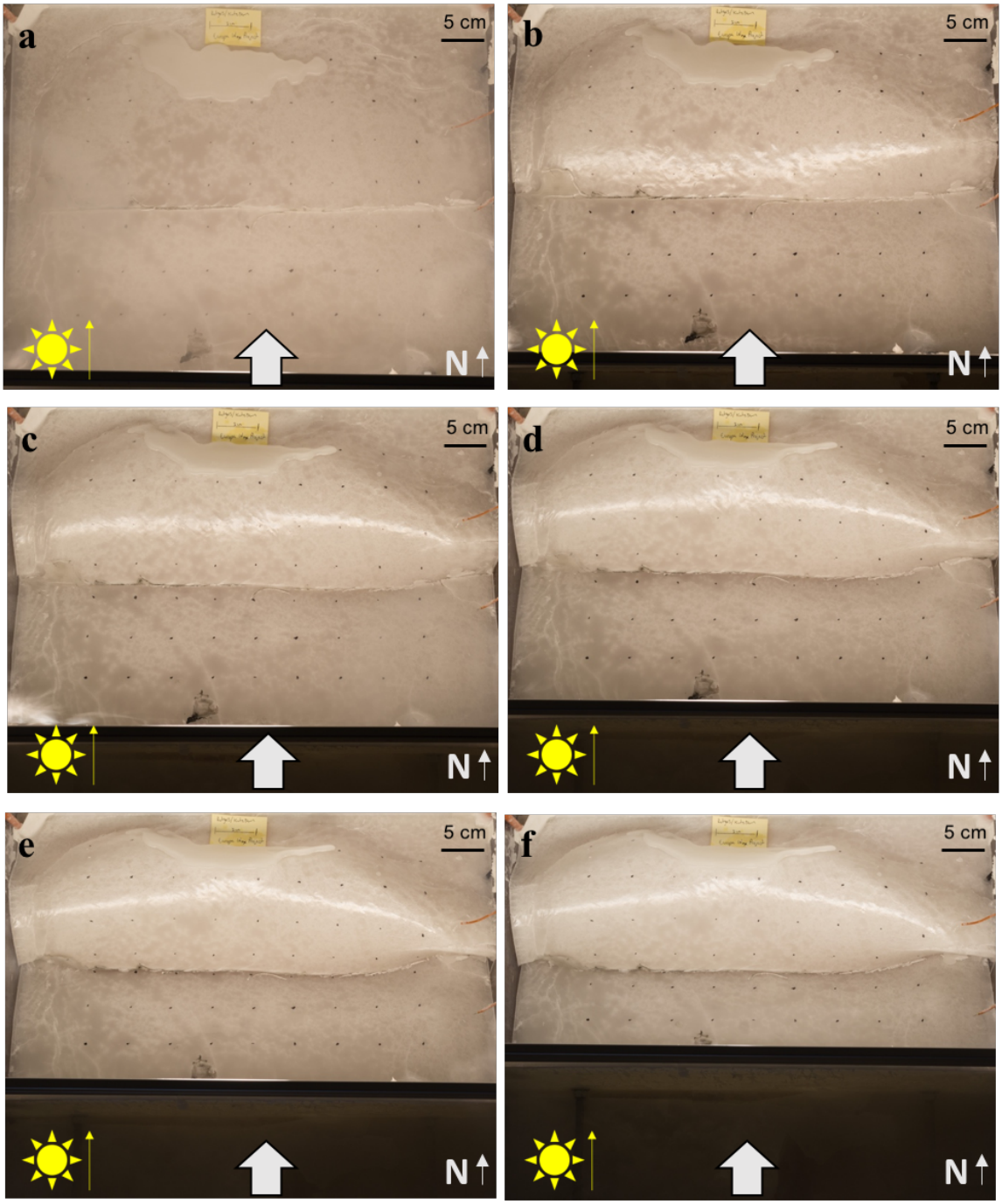

Figure F: Map view of 2 cm thick solid layer deformed at 20 cm/hr., vertical PZW at a) initial conditions, b) 2.5 cm displacement, c) 5 cm displacement, d) 7.5 cm displacement, e) 10 cm displacement, and f) 13.28 cm displacement. Symbols as in Fig. A.

2 cm solid layer deformed at 30 cm/hr. vertical PZW

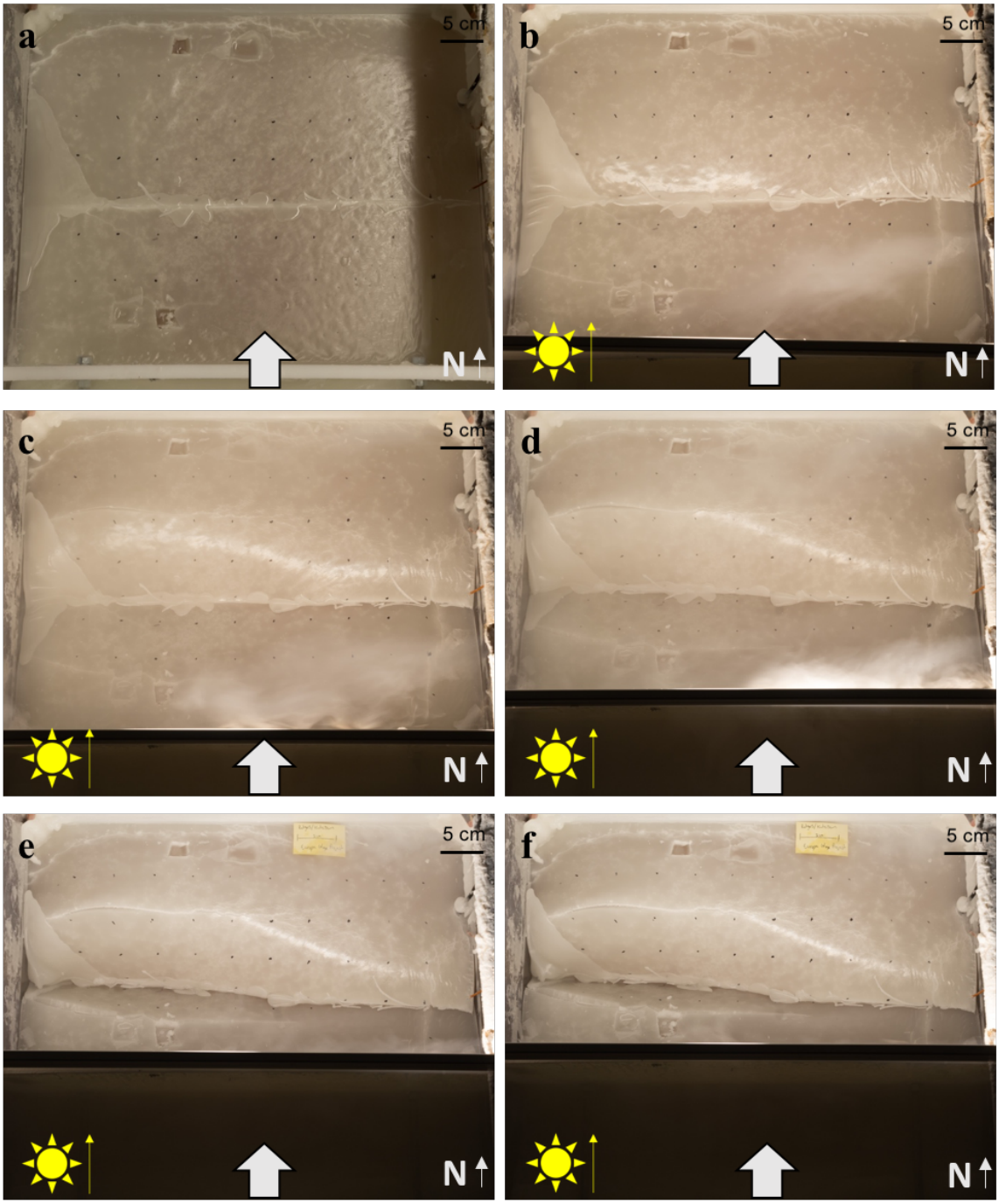

Figure G: Map view of 2 cm thick solid layer deformed at 30 cm/hr., vertical PZW at a) initial conditions, b) 2 cm displacement, c) 4 cm displacement, d) 8 cm displacement, e) 10 cm displacement, and f) 13 cm displacement. Lightning directions and symbols as in Fig. A.

2.5 cm solid layer deformed at 20 cm/hr. vertical PZW

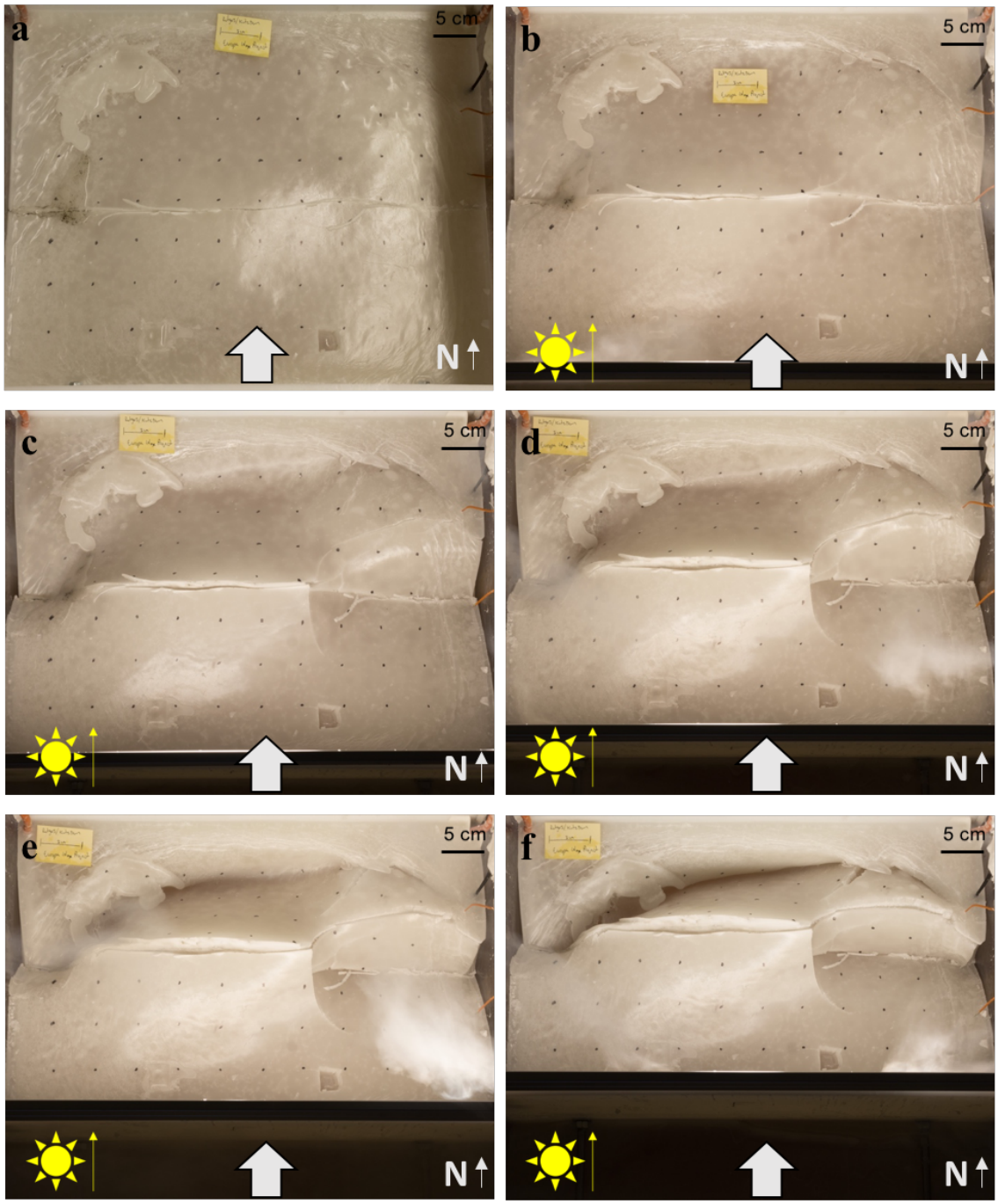

Figure H: Map view of 2.5 cm thick solid layer deformed at 20 cm/hr., vertical PZW at a) initial conditions, b) 1.7 cm displacement, c) 3.3 cm displacement, d) 5.8 cm displacement, e) 8.3 cm displacement, and f) 10.8 cm displacement. Lightning directions and symbols as in Fig. A.

2.5 cm solid layer deformed at 30 cm/hr. vertical PZW

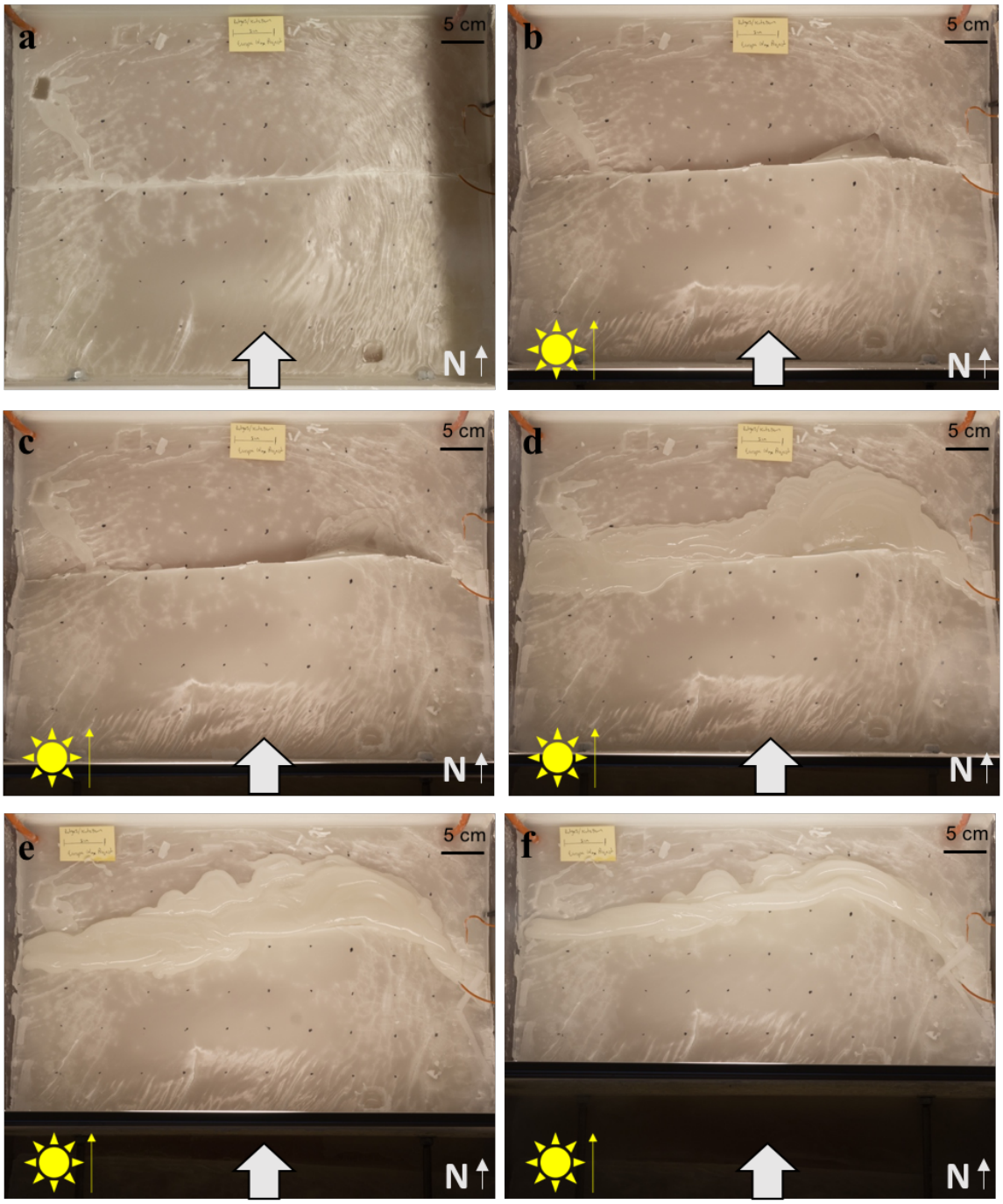

Figure I: Map view of 2.5 cm thick solid layer deformed at 30 cm/hr., vertical PZW at a) initial conditions, b) 2 cm displacement, c) 3 cm displacement, d) 4 cm displacement, e) 8 cm displacement, and f) 13 cm displacement. Lightning directions and symbols as in Fig. A.

3 cm solid layer deformed at 10 cm/hr. vertical PZW

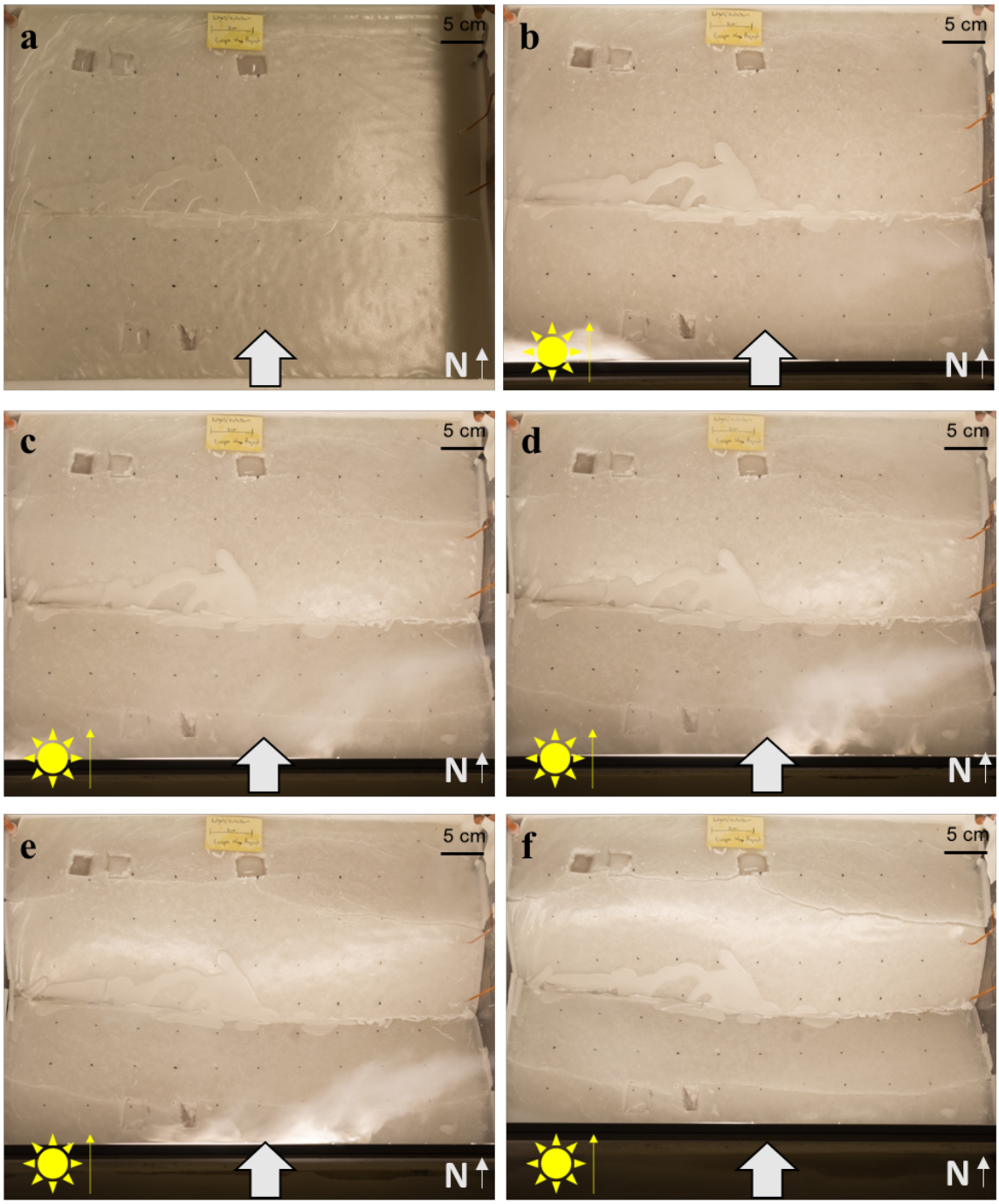

Figure J: Map view of 3 cm thick solid layer deformed at 10 cm/hr., vertical PZW at a) initial conditions, b) 1.5 cm displacement, c) 2.5 cm displacement, d) 3 cm displacement, e) 4 cm displacement, and f) 6 cm displacement. Lightning directions and symbols as in Fig. A.

3 cm solid layer deformed at 20 cm/hr. vertical PZW

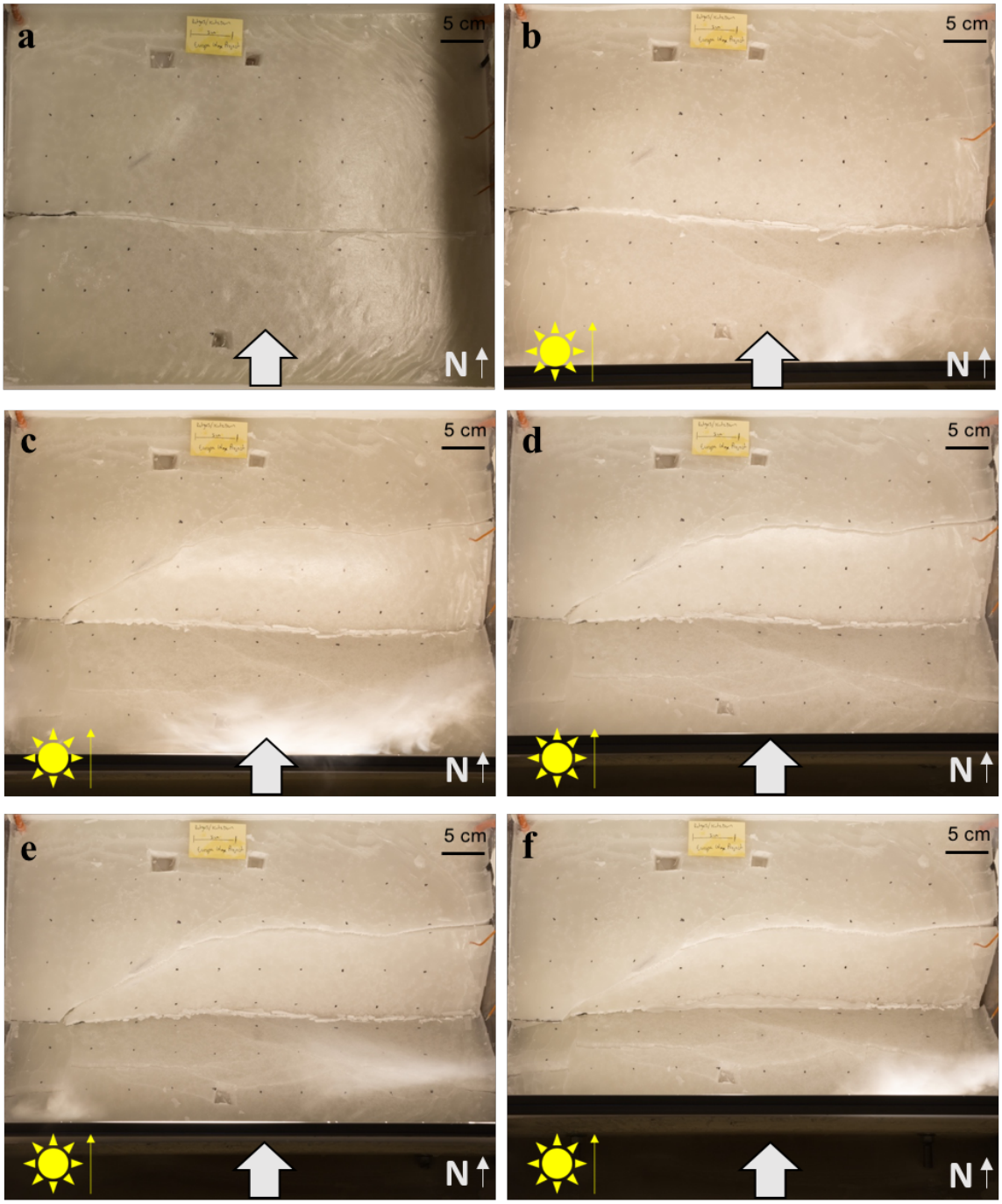

Figure K: Map view of 3 cm thick solid layer deformed at 20 cm/hr., vertical PZW at a) initial conditions, b) 2 cm displacement, c) 4 cm displacement, d) 6 cm displacement, e) 8 cm displacement, and f) 11 cm displacement. Lightning directions and symbols as in Fig. A.

3 cm solid layer deformed at 30 cm/hr. vertical PZW

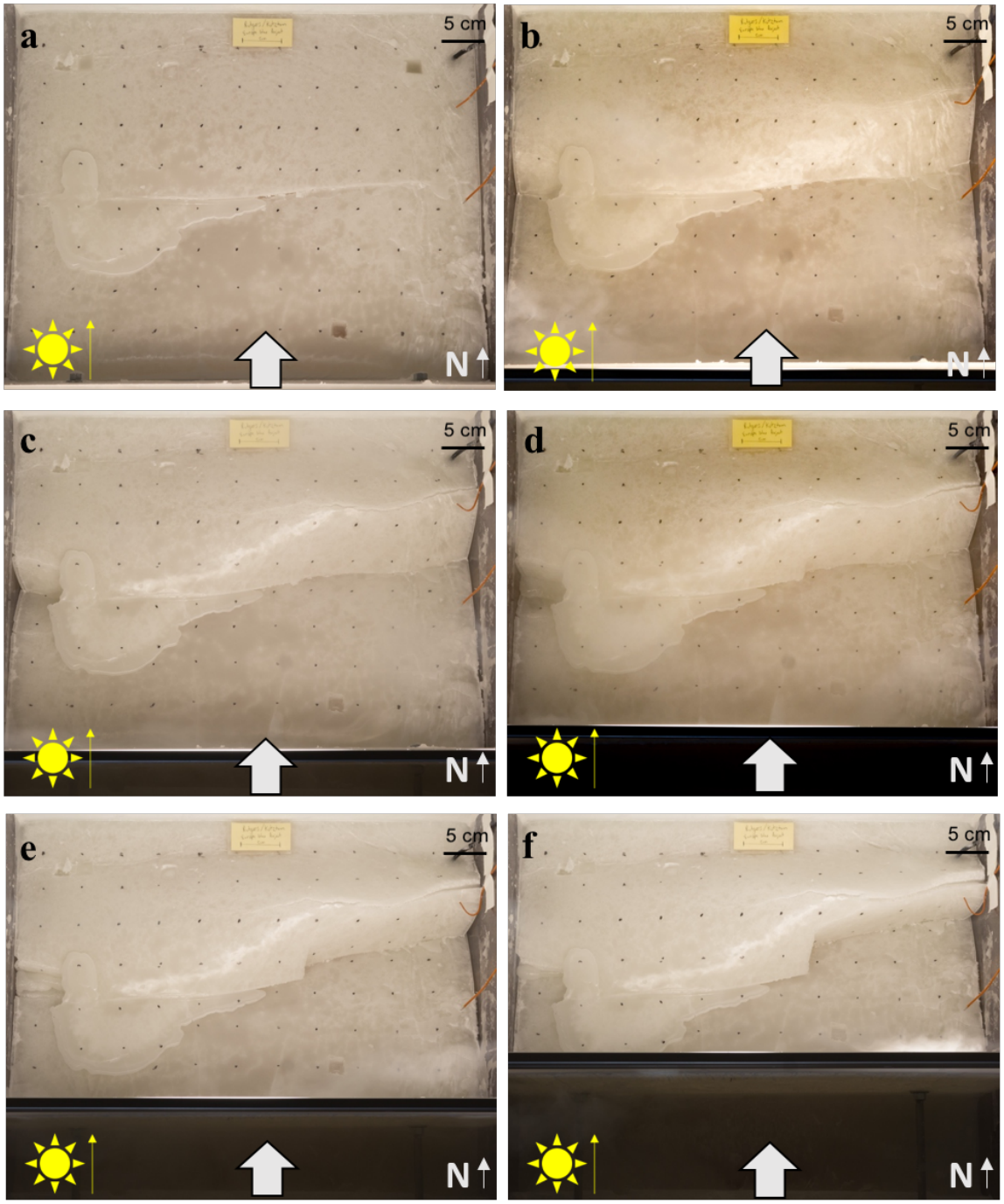

Figure L: Map view of 3 cm thick solid layer deformed at 30 cm/hr., vertical PZW at a) initial conditions, b) 2 cm displacement, c) 4 cm displacement, d) 6 cm displacement, e) 9 cm displacement, and f) 13 cm displacement. Symbols as in Fig. A.

4 cm solid layer deformed at 30 cm/hr. vertical PZW

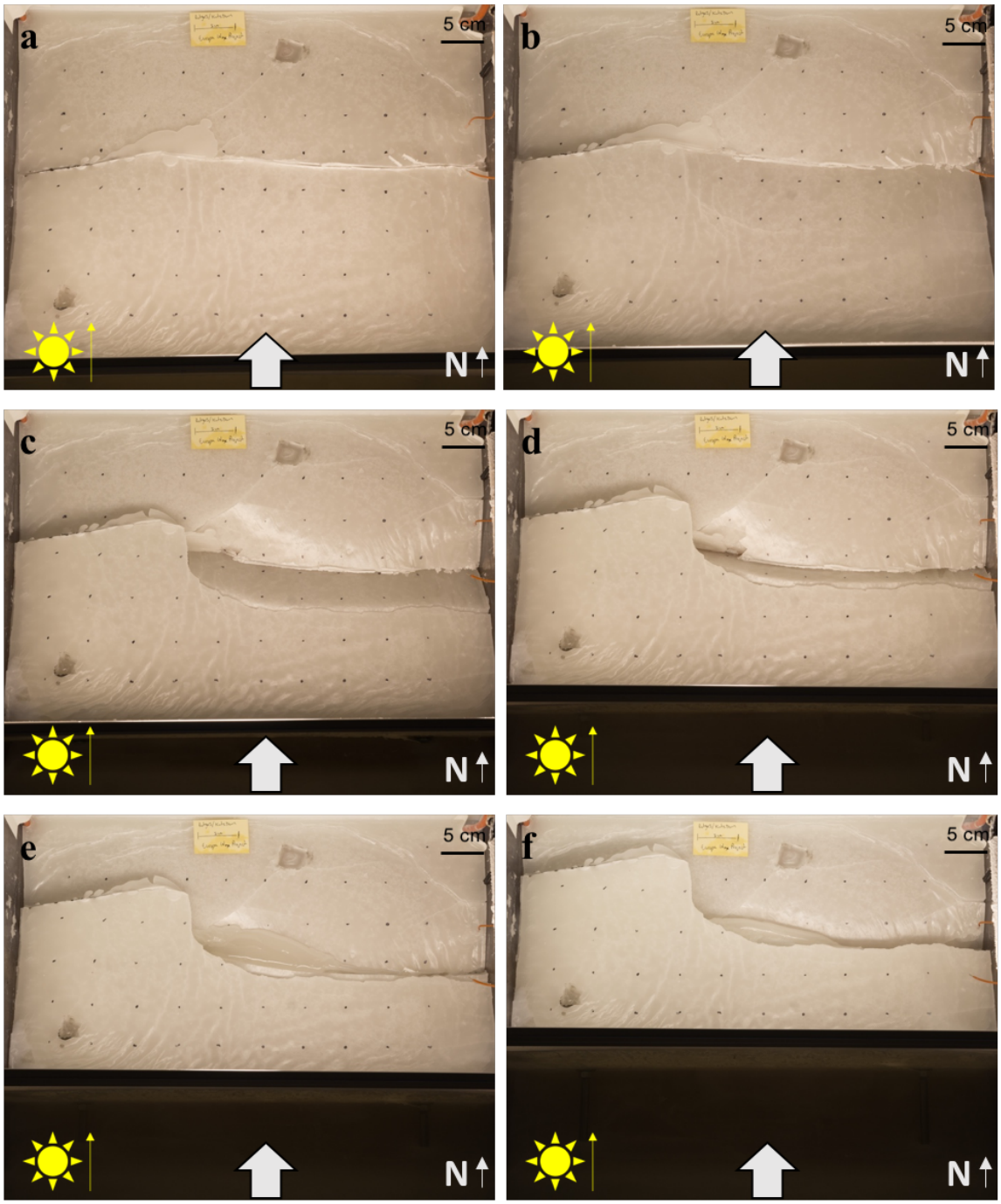

Figure M: Map view of 4 cm thick solid layer deformed at 30 cm/hr., vertical PZW at a) initial conditions, b) 2 cm displacement, c) 5 cm displacement, d) 8 cm displacement, e) 10 cm displacement, and f) 14 cm displacement. Symbols as in Fig. A.

1 cm solid layer deformed at 10 cm/hr. south dipping inclined PZW

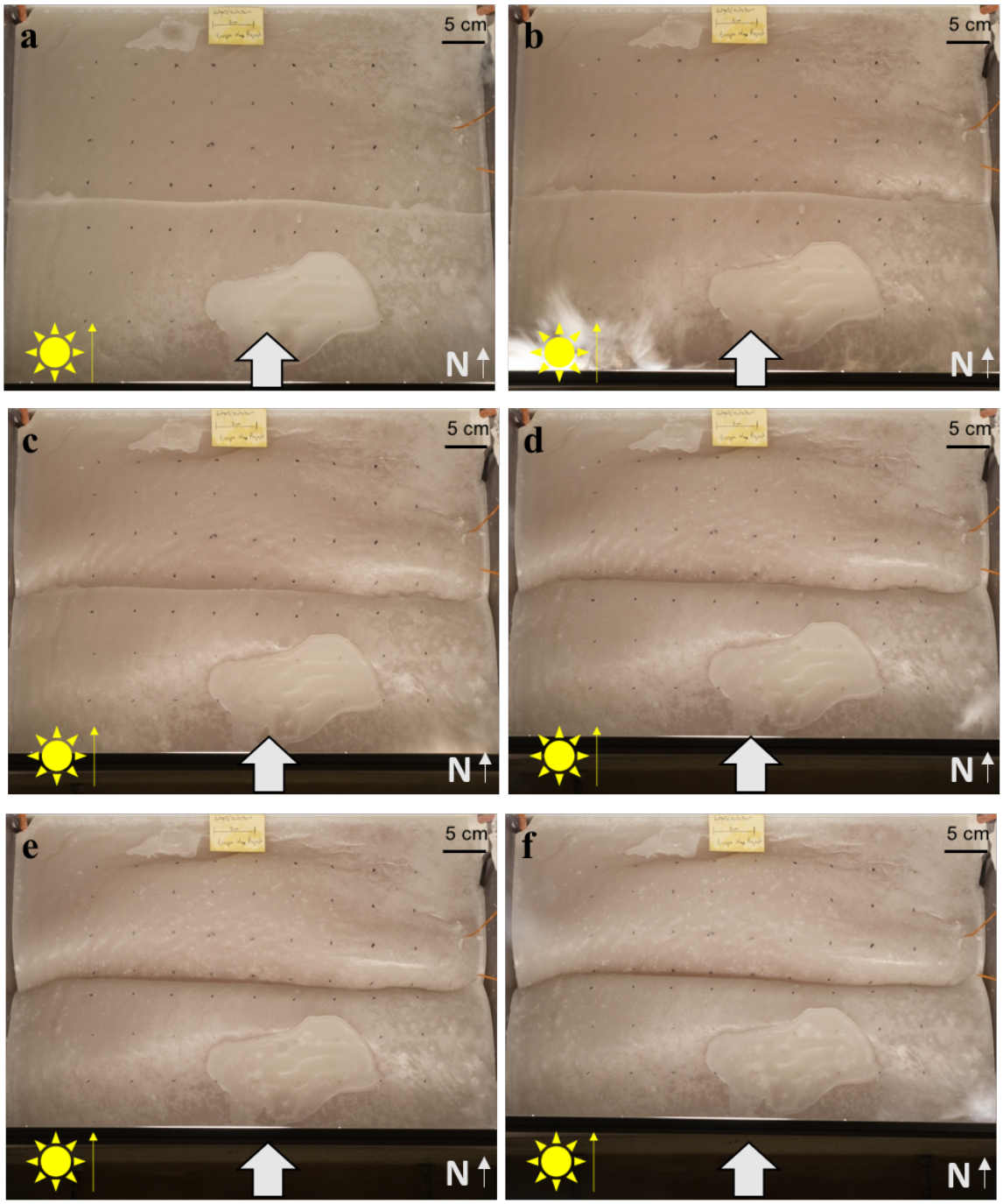

Figure N: Map view of 1 cm thick solid layer deformed at 10 cm/hr., inclined PZW at a) initial conditions, b) 1.5 cm displacement, c) 3 cm displacement, d) 4.5 cm displacement, e) 6 cm displacement, and f) 7 cm displacement. Symbols as in Fig. A.

1 cm solid layer deformed at 20 cm/hr. south dipping inclined PZW

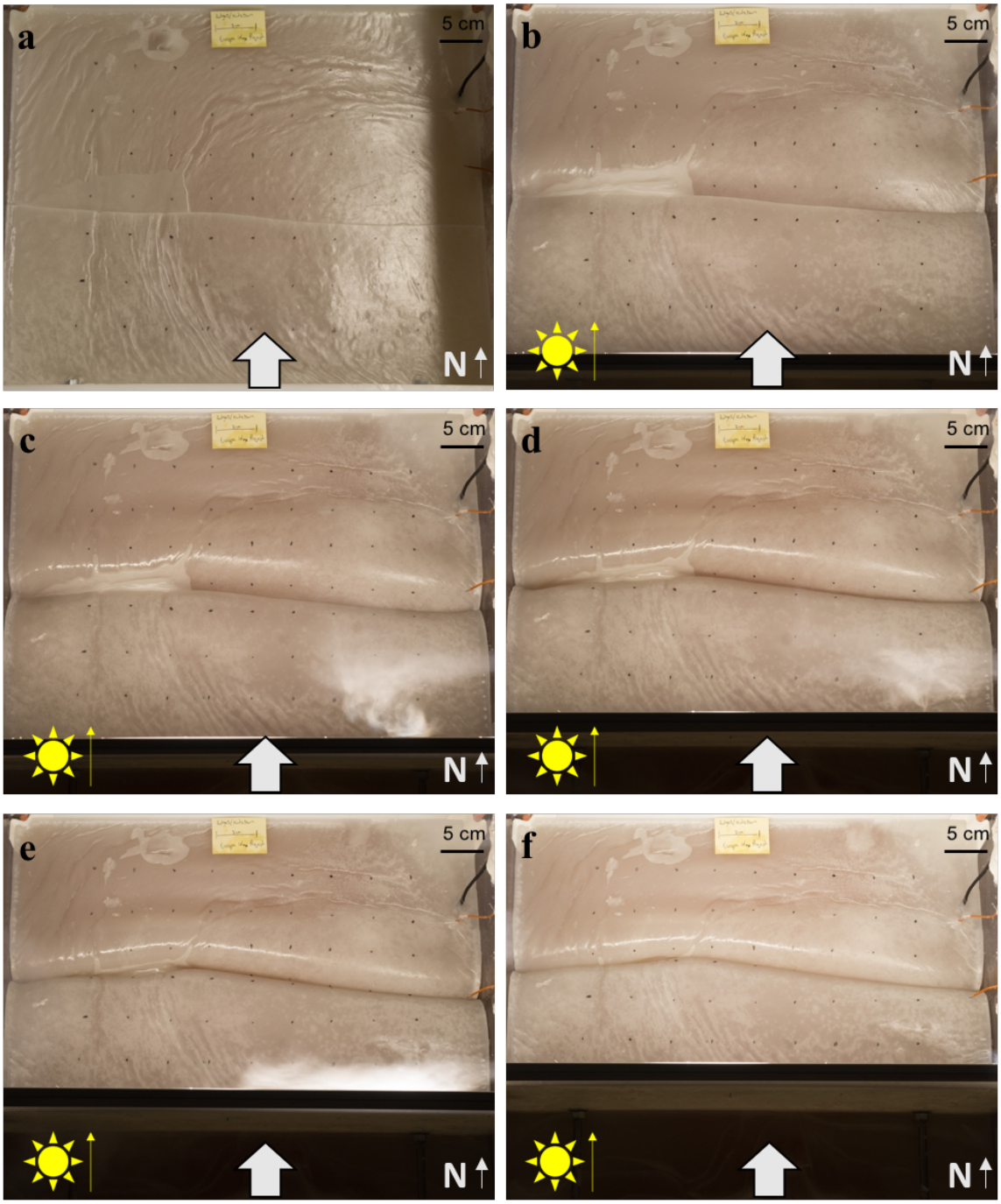

Figure O: Map view of 1 cm thick solid layer deformed at 20 cm/hr., inclined PZW at a) initial conditions, b) 2.5 cm displacement, c) 4.2 cm displacement, d) 6.6 cm displacement, e) 9.1 cm displacement, and f) 11.6 cm displacement. Lightning directions and symbols as in Fig. A.

1 cm solid layer deformed at 30 cm/hr. south dipping inclined PZW

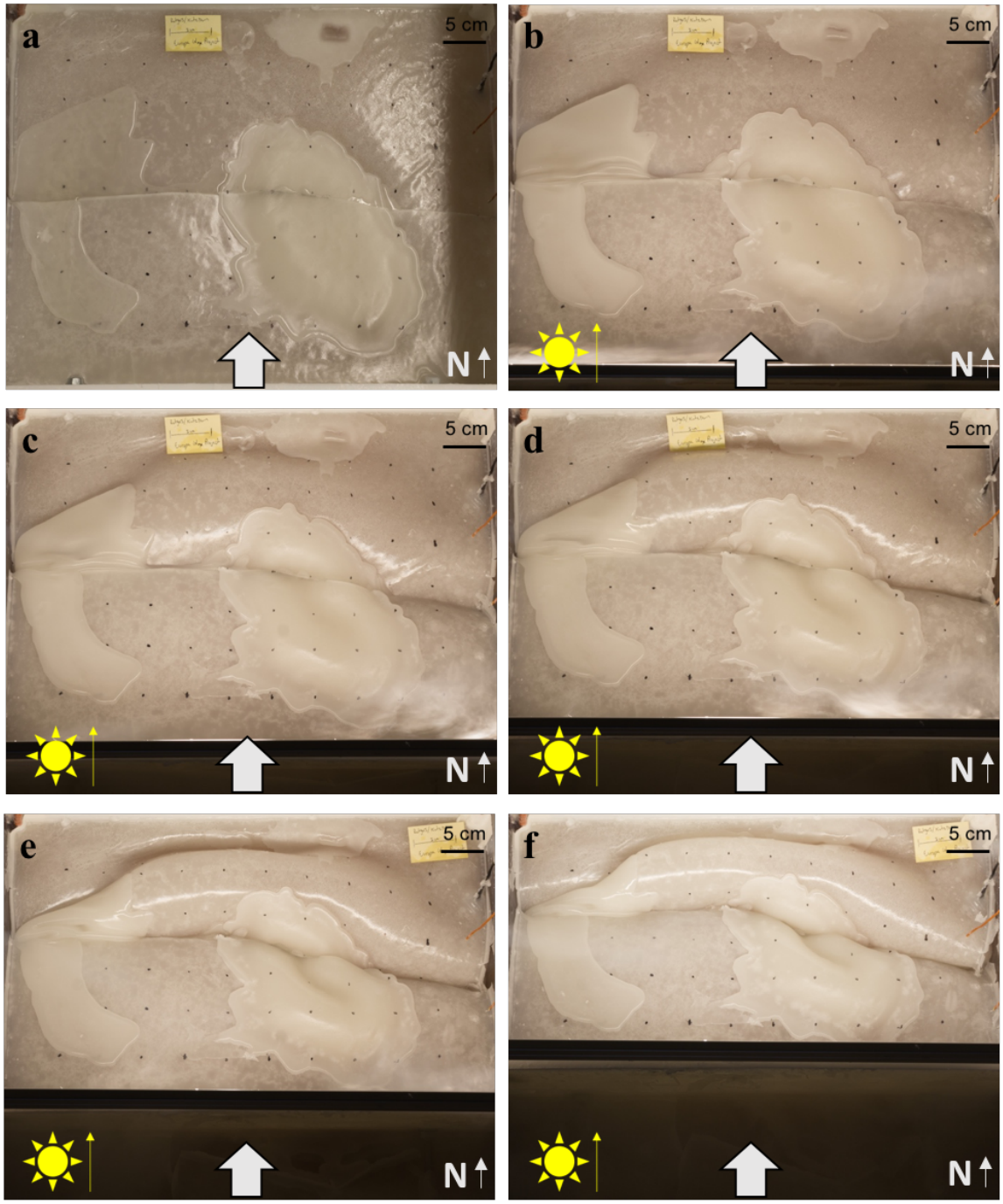

Figure P: Map view of 1 cm thick solid layer deformed at 30 cm/hr., inclined PZW at a) initial conditions, b) 2 cm displacement, c) 4 cm displacement, d) 6 cm displacement, e) 9 cm displacement, and f) 13 cm displacement. Lightning directions and symbols as in Fig. A.

2 cm solid layer deformed at 10 cm/hr. north dipping inclined PZW

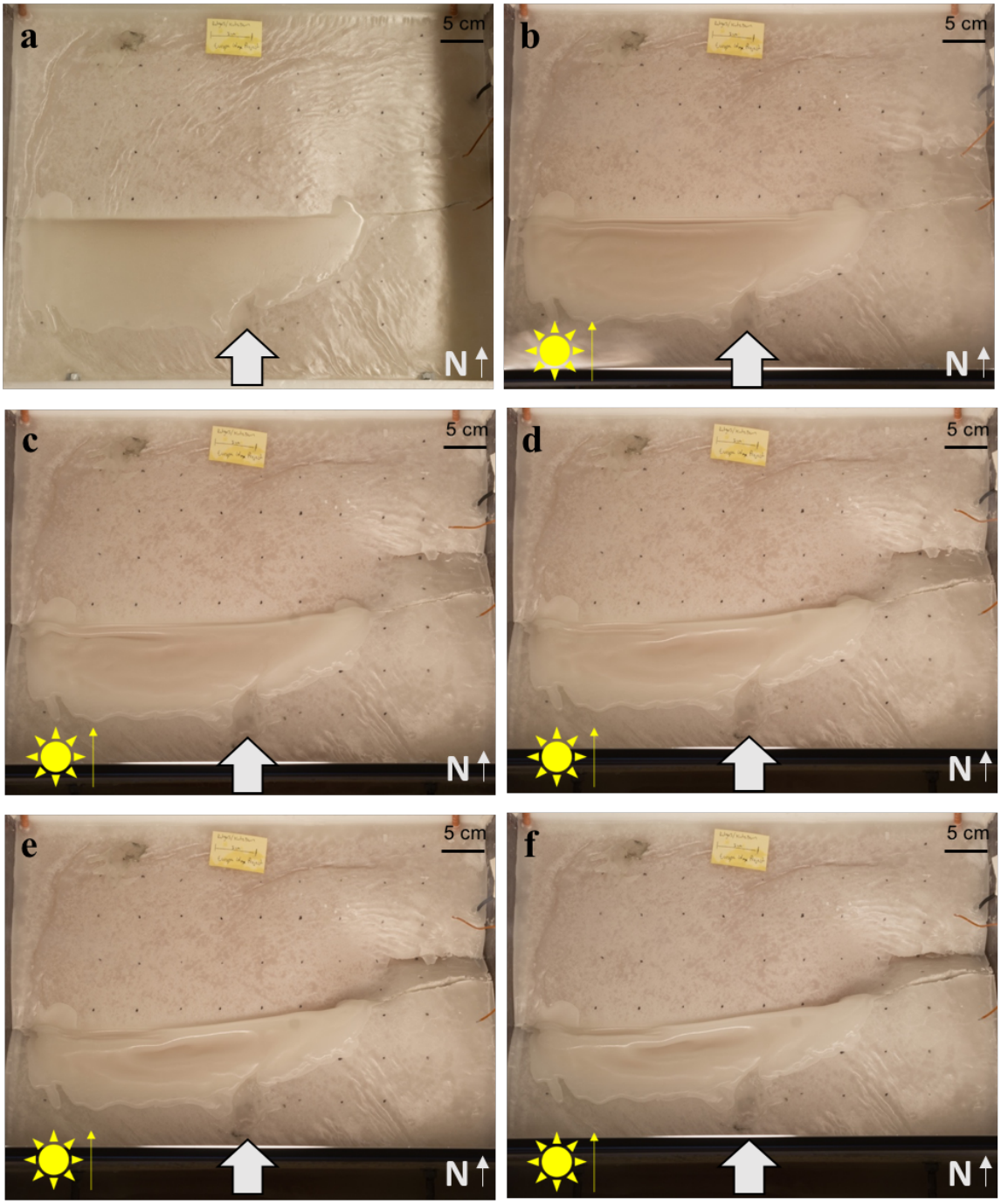

Figure Q: Map view of 2 cm thick solid layer deformed at 10 cm/hr., inclined PZW at a) initial conditions, b) 1 cm displacement, c) 2 cm displacement, d) 3 cm displacement, e) 4 cm displacement, and f) 5 cm displacement. Lightning directions and symbols as in Fig. A.

2 cm solid layer deformed at 20 cm/hr. south dipping inclined PZW

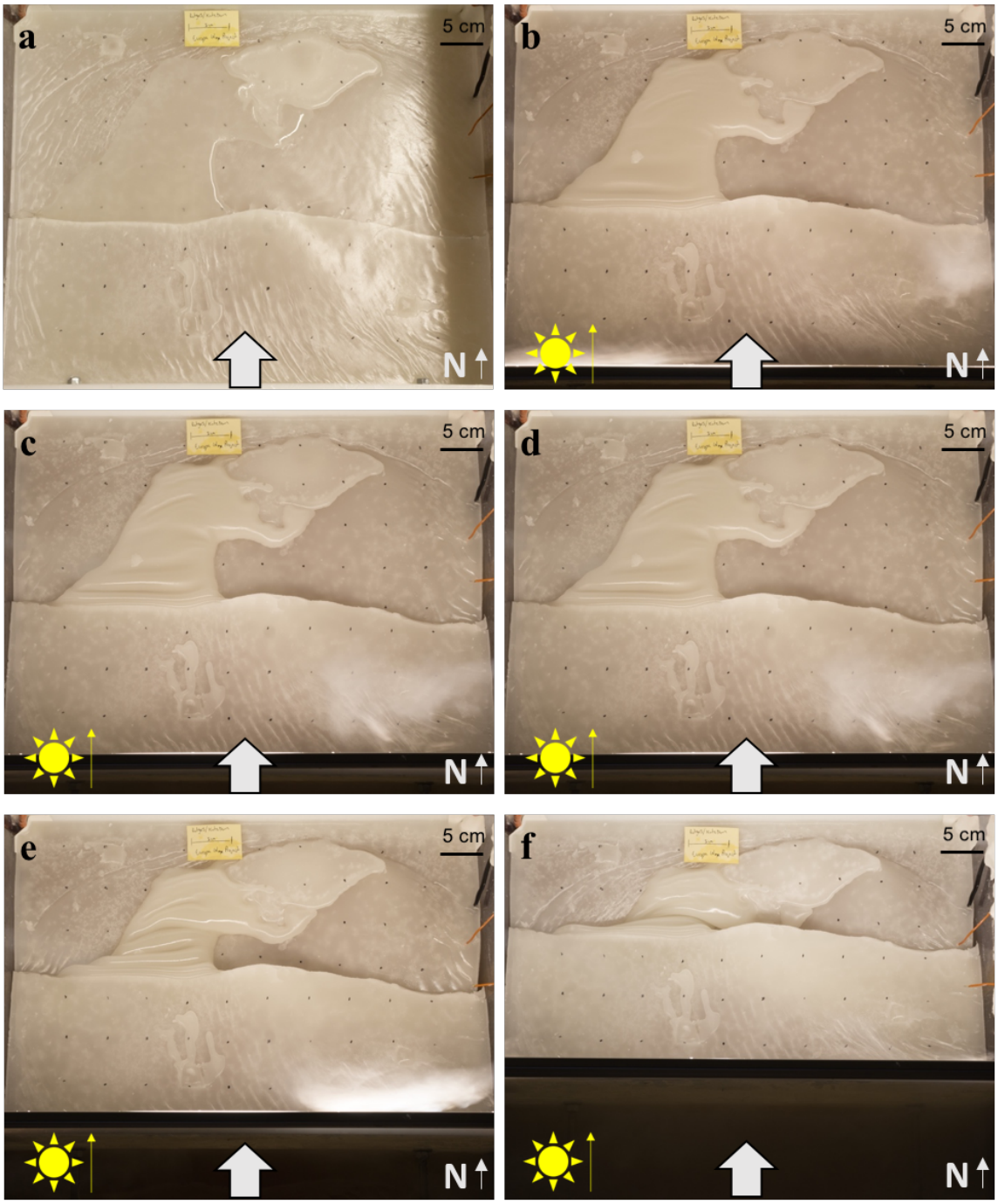

Figure R: Map view of 2 cm thick solid layer deformed at 20 cm/hr., inclined PZW at a) initial conditions, b) 1.6 cm displacement, c) 2.5 cm displacement, d) 4.2 cm displacement, e) 6.4 cm displacement, and f) 11.6 cm displacement. Lightning directions and symbols as in Fig. A.

2 cm solid layer deformed at 30 cm/hr. south dipping inclined PZW

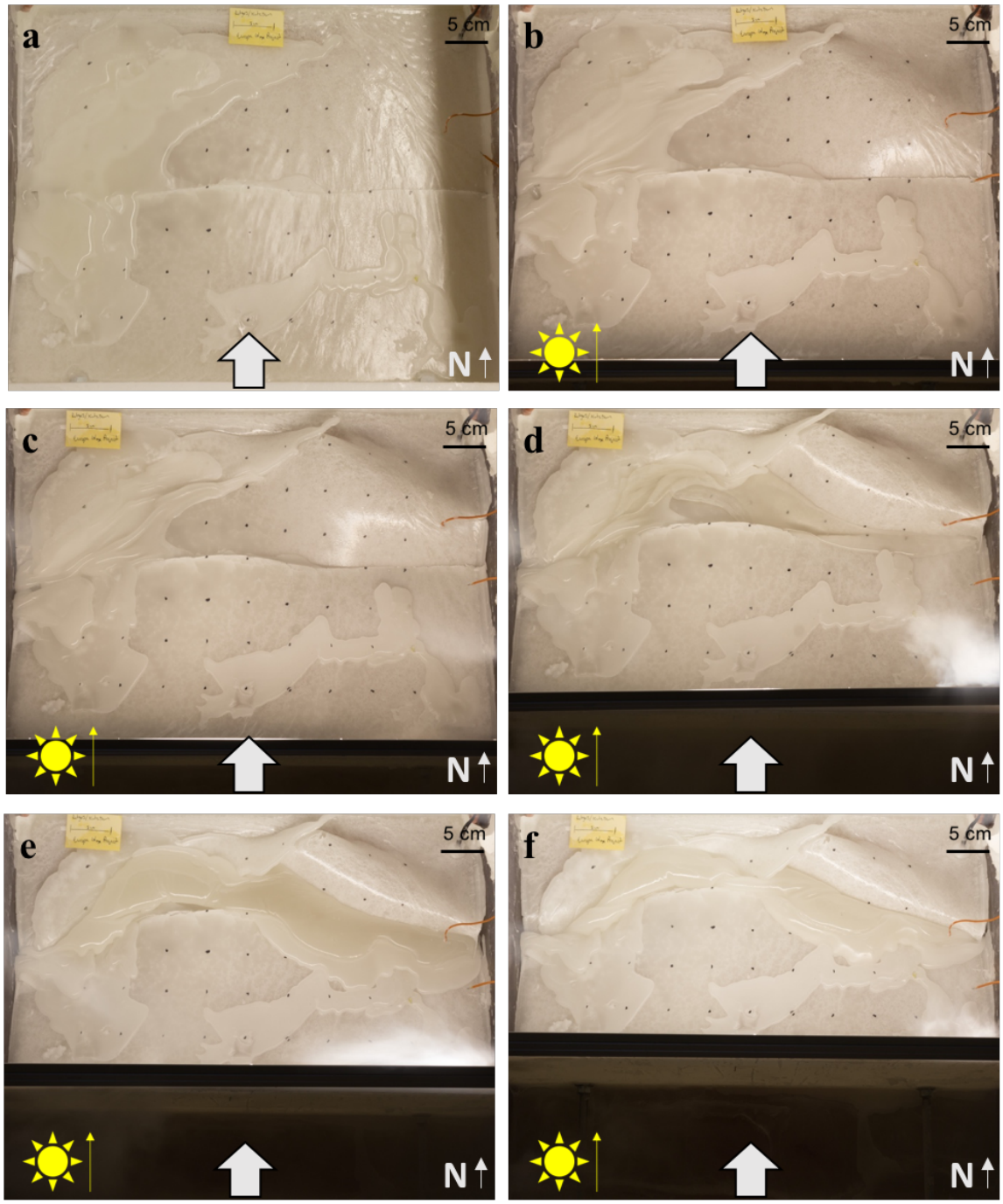

Figure S: Map view of 2 cm thick solid layer deformed at 30 cm/hr., inclined PZW at a) initial conditions, b) 2 cm displacement, c) 4 cm displacement, d) 8 cm displacement, e) 10 cm displacement, and f) 13 cm displacement. Lightning directions and symbols as in Fig. A.

2.5 cm solid layer deformed at 30 cm/hr. north dipping inclined PZW

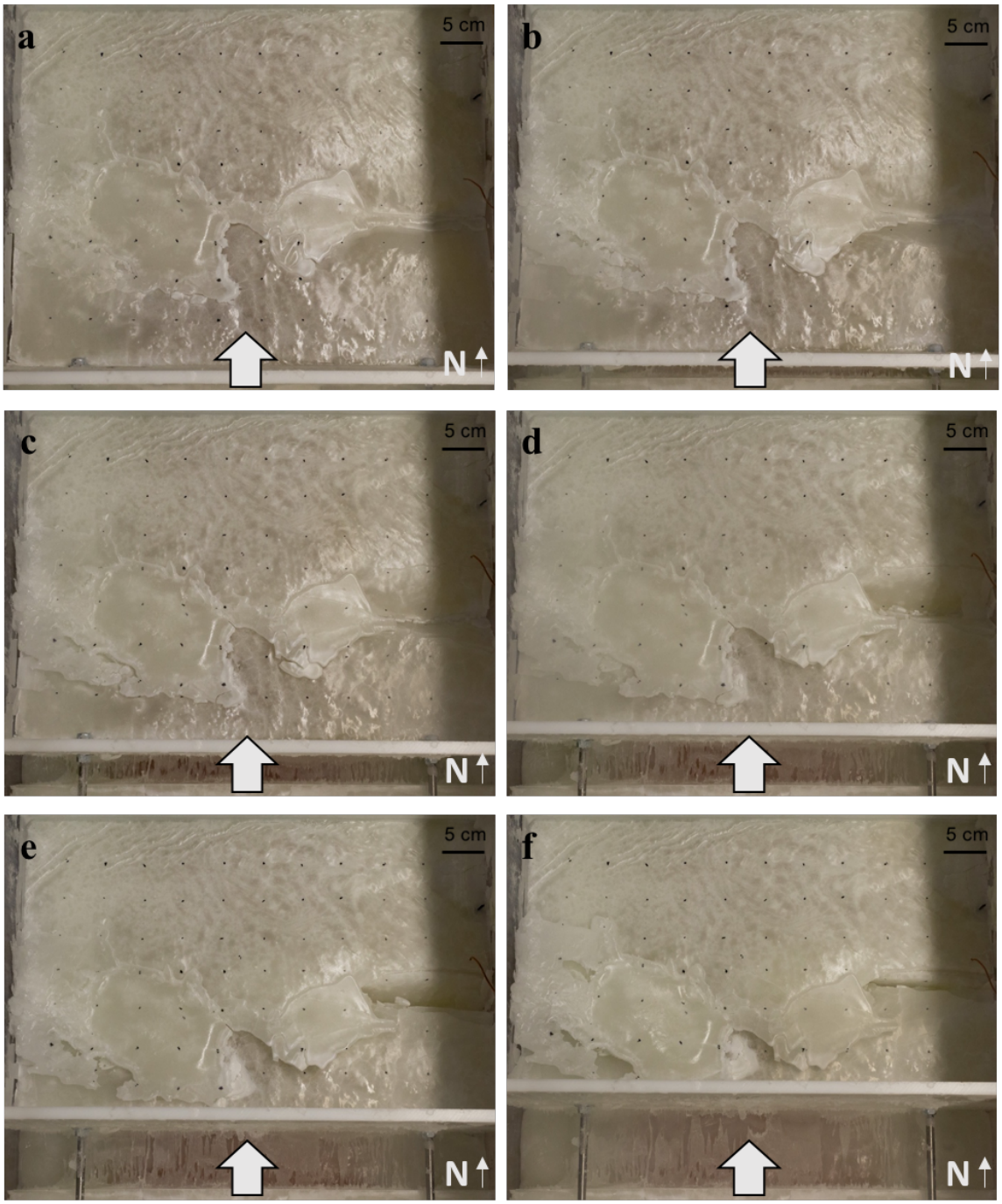

Figure T: Map view of 2.5 cm thick solid layer deformed at 30 cm/hr., inclined PZW at a) initial conditions, b) 2 cm displacement, c) 4 cm displacement, d) 6 cm displacement, e) 8 cm displacement, and f) 11 cm displacement. Lighting from above; symbols as in Fig. A.

3 cm solid layer deformed at 10 cm/hr. south dipping inclined PZW

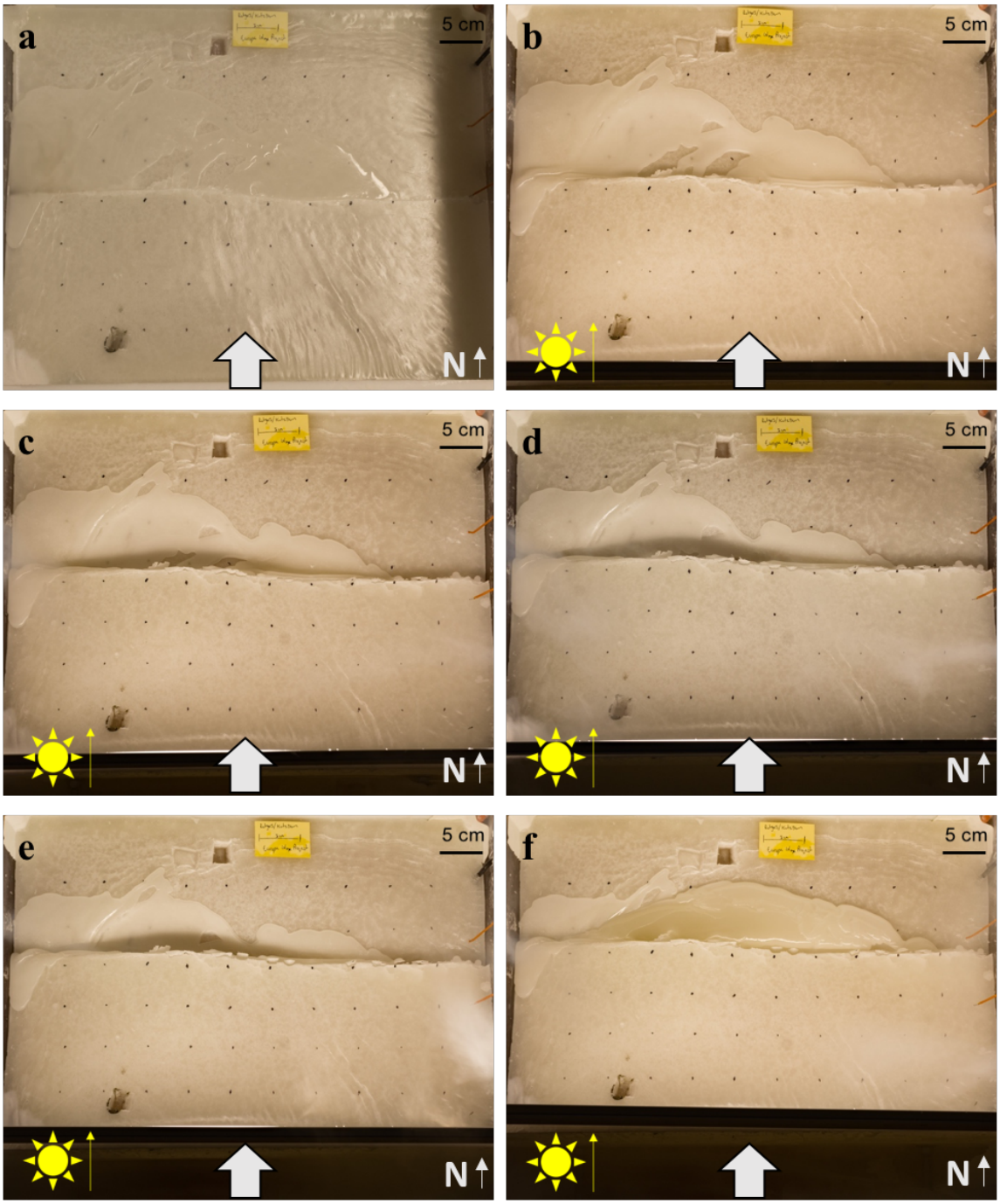

Figure U: Map view of 3 cm thick solid layer deformed at 10 cm/hr., inclined cut at a) initial conditions, b) 1.5 cm displacement, c) 3 cm displacement, d) 4.5 cm displacement, e) 6 cm displacement, and f) 7.5 cm displacement. Lightning directions and symbols as in Fig. A.

3 cm solid layer deformed at 20 cm/hr. south dipping inclined PZW

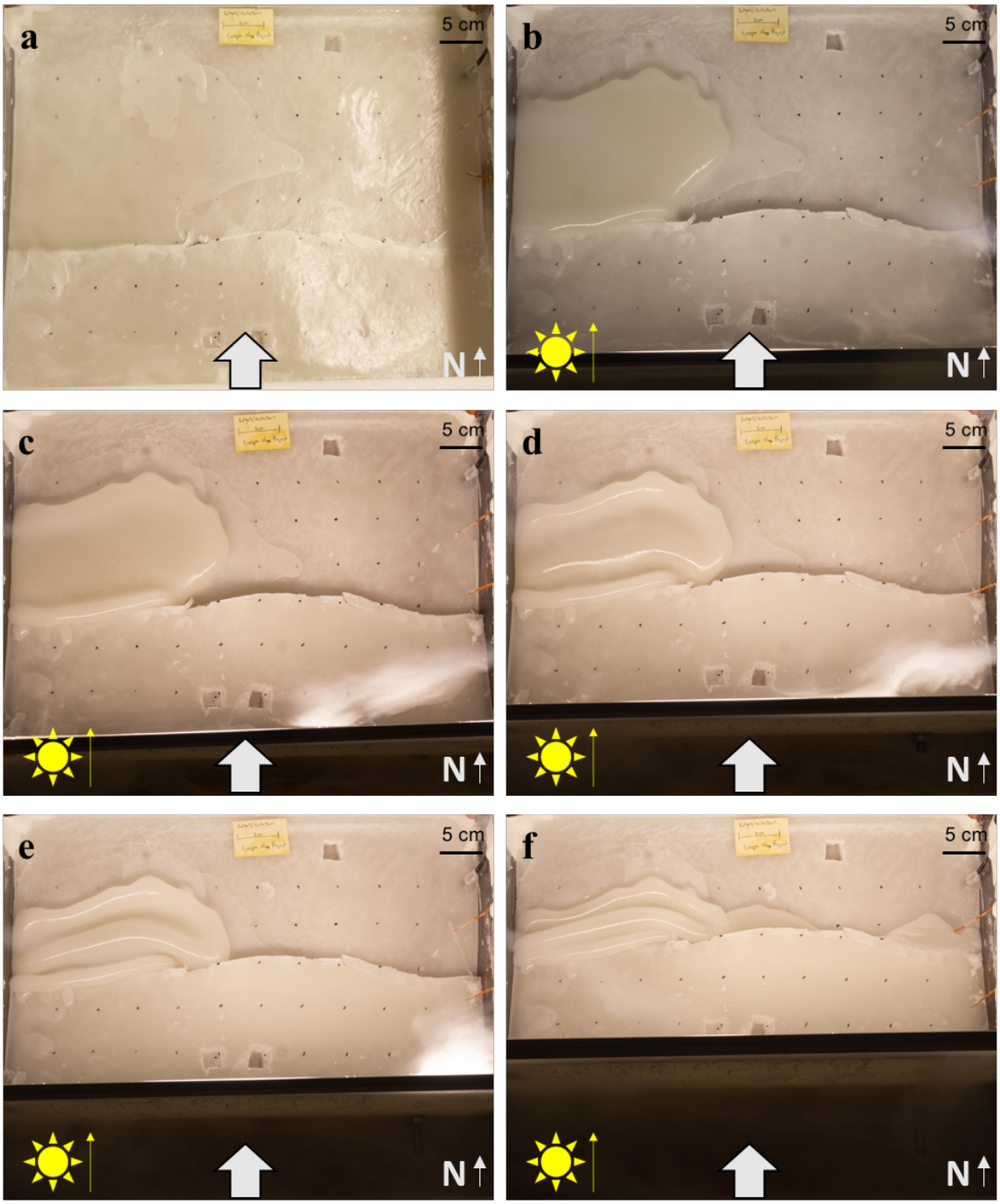

Figure V: Map view of 3 cm thick solid layer deformed at 20 cm/hr., inclined PZW at a) initial conditions, b) 2.5 cm displacement, c) 5 cm displacement, d) 7.5 cm displacement, e) 10 cm displacement, and f) 13.3 cm displacement. Lightning directions and symbols as in Fig. A.

3 cm solid layer deformed at 30 cm/hr. south dipping inclined PZW

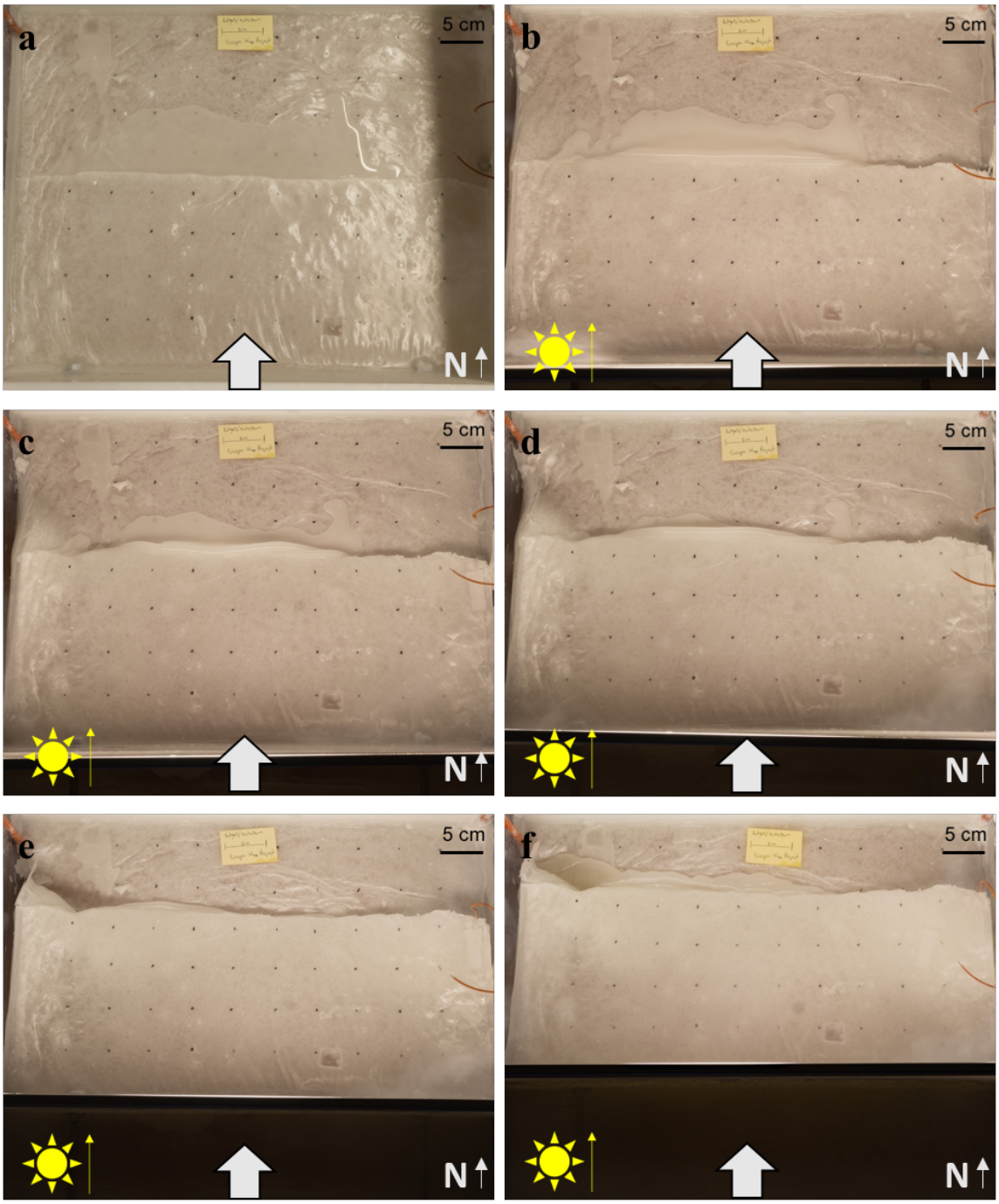

Figure W: Map view of 3 cm thick solid layer deformed at 30 cm/hr., inclined PZW at a) initial conditions, b) 2 cm displacement, c) 4 cm displacement, d) 6 cm displacement, e) 10 cm displacement, and f) 13 cm displacement. Lightning directions and symbols as in Fig. A.

2 cm solid layer deformed at 30 cm/hr. vertical half PZW

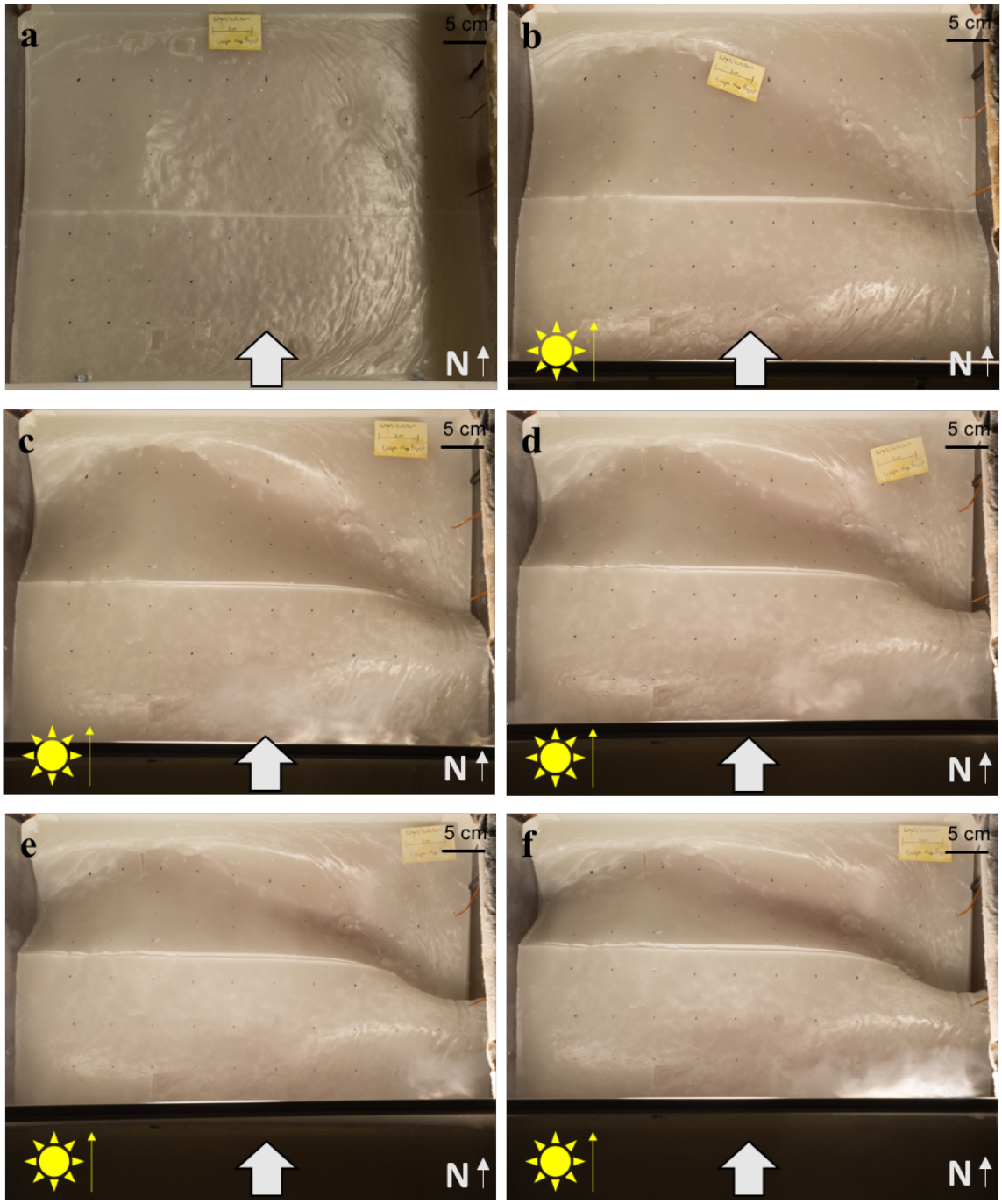

Figure X: Map view of 2 cm thick solid layer deformed at 30 cm/hr., vertical PZW at a) initial conditions, b) 2 cm displacement, c) 4 cm displacement, d) 6 cm displacement, e) 8 cm displacement, and f) 9 cm displacement. Lightning directions and symbols as in Fig. A.